Searches for New Particles in Final States with Jet(s) and Missing Transverse Momentum using first ATLAS Data

Dissertation zur Erlangung der Doktorwürde
Vorgelegt von

Florian Ahles

Fakultät für Mathematik und Physik
Albert-Ludwigs-Universität Freiburg

Dekan:	Prof. Dr. Kay Königsmann
Leiter der Arbeit:	Prof. Dr. Gregor Herten
Referent:	Prof. Dr. Gregor Herten
Koreferent:	PD. Dr. Christian Schill
Tag der Verkündigung des Prüfungsergebnisses:	01.07.2011

Contents

Chapter 1

Introduction

With the start-up of the Large Hadron Collider (LHC) a new era in Particle Physics is dawning. There is good reason to believe that new physics beyond the Standard Model will be discovered at the four experiments analyzing LHC collisions.

This thesis contributes to the search for new physics at the ATLAS experiment analyzing events with missing transverse momentum, jets and no isolated leptons. The theoretical interpretation of the results focuses on Supersymmetry (SUSY) as one possible extension of the SM. A typical SUSY signature in the detector includes several jets from the decay cascades of the produced SUSY particles and missing transverse momentum due to the escaping lightest Supersymmetric particles (c.f. Chapter 2). Nevertheless, any other new phenomenon with the same signature would be discovered by the analyses.

The layout of this work is as follows. Chapter 2 briefly introduces the theoretical aspects needed for the analysis part. After a short description of the SM, SUSY is presented as one of the possible extensions. The signatures of potential realizations are described in more detail. Besides the Minimal Supersymmetric Standard Model with a neutralino playing the role of the lightest Supersymmetric particle, the Split SUSY Model is introduced. Processes giving rise to a monojet signature in the detector are discussed.

The LHC and the ATLAS experiment are covered in Chapter 3. The chapter introduces all detector subsystems emphasizing the calorimeters, which are the most important subdetectors for analyses requiring jets and missing transverse momentum. After the description of the trigger system, the ATLAS analysis chain is briefly introduced.

Chapter 4 describes a very early Monte Carlo study, which proposes the use of a monojet analysis in order to spot detector problems. This study was done before any collision data was available.

Another possible hazard to physics analyses is studied in Chapter 5. It is crucial to control non-collision background from cosmic rays, beam-gas and beam halo events. Multivariate techniques were used to optimize cuts suppressing this kind of background. Monte Carlo as well as early single beam and cosmic data were used in the study.

After the preparational work, the following chapters describe two of the first searches for new physics with the ATLAS detector. For the search in channels with at least two or three jets, missing transverse momentum and no isolated lepton, the QCD background was determined using normalization factors from control regions. The method is described along with the analysis and the final results of the search in Chapter 6.

The ongoing joint effort between the ATLAS SUSY and EXOTICS groups concerning searches for new physics in the monojet channel is described in Chapter 7. The QCD background was determined using two different methods. The result of the search is interpreted as limit on the gluino mass in the Split SUSY model.

The thesis also reflects the transition of the ATLAS experiment from the preparation to the early running stage.

Chapter 2

Theoretical aspects

This chapter outlines the theoretical aspects, which are necessary for the analysis part of this work. The first section briefly describes the current understanding of Particle Physics - the so-called Standard Model (SM). After discussing its shortcomings, the second part describes Supersymmetry (SUSY) as a possible extension of the SM. The description of the gravitational and gauge mediated breaking scenario within the Minimal Supersymmetric Standard Model is followed by a more exotic model called Split Supersymmetry. That is interesting for this work in particular, since the monojet final state is one of its possible signatures.

The chapter is not intended as a complete thorough theoretical work, but should rather serve as a guideline for the motivation of the analysis part and the understanding of the signatures in the detector. At the end of the chapter, the Monte Carlo generators used for event simulation are briefly introduced.

2.1 The Standard Model

A very good and complete discussion of the SM can be found e.g. in [1], which also serves as the basis of this short summary. Using the principle of local gauge invariance and spontaneous symmetry breaking, the SM describes the fundamental particles and their interactions (strong and electroweak) [1] within a quantum field theory.

2.1.1 Particle content of the SM

The particle content is divided into two general groups: spin $\frac{1}{2}$ fermions, that constitute all the matter, and spin 1 gauge bosons, that mediate the forces.

Fermions are distinguished into quarks and leptons. Quarks are the fundamental building blocks of baryonic and mesonic matter and are subject to all three forces (strong, weak and electromagnetic). Leptons, in turn, only respond to the weak and electromagnetic interaction. Both categories themselves are subdivided into three, so-called, generations. Table 2.1 shows the three generations of SM leptons and quarks with their masses. The gauge bosons, which mediate the forces between the fermions, are listed in Table 2.2 with their masses and electric charges.

[1] The gravitational force is not covered by the SM.

leptons			quarks		
name	symbol	mass [MeV]	name	symbol	mass [MeV]
electron	e^-	0.511	down	d	4.1 to 5.8
electron neutrino	ν_e	$< 2 \times 10^{-6}$	up	u	1.7 to 3.3
muon	μ^-	105.7	strange	s	101^{+29}_{-21}
muon neutrino	ν_μ	< 0.19	charm	c	$1.27^{+0.07}_{-0.09} \times 10^3$
tau	τ^-	1776.82 ± 0.16	bottom/beauty	b	$4,19^{+0.18}_{-0.06} \times 10^3$
tau neutrino	ν_τ	< 18.2	top	t	$172.0 \pm 0.9 \pm 1.3 \times 10^3$

Table 2.1: The Standard Model fermions and their masses [2]. The uncertainties on the e^- and μ^- masses are negligible.

name	force	mass [MeV]	charge [e]
Photon γ	electroweak	$< 1 \times 10^{-24}$	$< 1 \times 10^{-35}$
Z Boson	electroweak	$91.188 \pm 0.002 \times 10^3$	0
W Bosons ($W^\pm$)	electroweak	$80.399 \pm 0.023 \times 10^3$	± 1
Gluon g	strong	$< \mathcal{O}(1)$	0

Table 2.2: The Standard Model bosons, the interaction they mediate, their masses and charge (in units of the elementary charge e)[2]. The gluon is regarded massless in theory; the experimental constraint on its mass is taken from [3].

The following paragraphs will briefly introduce how SM interactions are described as a quantum field theory using the principle of local gauge invariance. Also the Higgs mechanism is covered as an essential ingredient to account for the masses of the weak gauge bosons.

2.1.2 Electroweak theory

Other than the electromagnetic coupling, which is purely vectorial, the (charged) weak coupling is a mixture of vector and axial vector components. In order to overcome this problem in the unification, the combined vector and axial vector nature of the coupling is absorbed in the spinor, distinguishing so-called 'left-handed' spinor doublets and 'right-handed' spinor singlets. Details on it can be found e.g. in [1] or in the original publications [4, 5], but the baseline result is, that the weak interaction only couples to left-handed spinors.

For the unified electroweak interaction one considers the Lagrangian of two spin 1/2 Dirac fields (ψ_1, ψ_2) with equal mass m in the absence of any interaction [2]:

$$\begin{aligned} \mathscr{L} &= i\hbar c \bar{\psi}\gamma^\mu \partial_\mu \psi - mc^2 \bar{\psi}\psi \qquad (2.1) \\ \psi &\equiv \begin{pmatrix} \psi_1 \\ \psi_2 \end{pmatrix} \end{aligned}$$

[2]For the sake of clarity of the argument, there is no explicit distinction between the left- and right-handed spinors. One should just bare in mind, that the weak interaction only couples to the left-handed component, while the electromagnetic interaction couples to both.

The Lagrangian in Equation 2.1 is invariant under the global gauge transformation $\psi \to U\psi$, where U is a unitary matrix, that can be written in the form

$$U = e^{i\theta} e^{-iQ\boldsymbol{\tau}\cdot\boldsymbol{\lambda}/\hbar c} \tag{2.2}$$

This means, that the Lagrangian is invariant under global U(1) ($e^{i\theta}$) and SU(2) ($e^{-iQ\boldsymbol{\tau}\cdot\boldsymbol{\lambda}/\hbar c}$) transformations. When turning the global symmetries into local ones, the Lagrangian has to be modified in order to preserve the invariance.

Separating the two symmetries and looking first at the U(1) symmetry, one finds that the free Lagrangian of the single Dirac field (e.g. ψ_1) has to be modified into Equation 2.3 in order to admit local invariance.

$$\begin{aligned} \mathscr{L} &= [i\hbar c\bar{\psi}_1\gamma^\mu\partial_\mu\psi_1 - mc^2\bar{\psi}_1\psi_1] - [\frac{1}{16\pi}F^{\mu\nu}F_{\mu\nu}] - (q\bar{\psi}_1\gamma^\mu\psi_1)A_\mu \\ F^{\mu\nu} &\equiv (\partial^\mu A^\nu - \partial^\nu A^\mu) \end{aligned} \tag{2.3}$$

Imposing local gauge invariance leads to the interaction with the vector field A^μ, which can be identified with the electromagnetic potential, just as q can be identified with the electric charge. It is important to notice, that the field A^μ has to be massless. Otherwise the local gauge invariance would be destroyed.

For the $SU(2)$ symmetry on the two Dirac fields ψ one follows the exact same approach. When turning the global into a local transformation according to $\psi \to S\psi$, where $S \equiv e^{-iQ\boldsymbol{\tau}\cdot\boldsymbol{\lambda}(x)/\hbar c}$, with $\boldsymbol{\tau}$ being the Pauli matrices, one again has to modify the Lagrangian in order to preserve the invariance. This is accomplished by introducing three vector fields, which also have to be massless.

$$\begin{aligned} \mathscr{L} &= [i\hbar c\bar{\psi}\gamma^\mu\partial_\mu\psi - mc^2\bar{\psi}\psi] - [\frac{1}{16\pi}\mathbf{F}^{\mu\nu}\cdot\mathbf{F}_{\mu\nu}] - (Q\bar{\psi}\gamma^\mu\boldsymbol{\tau}\psi)\cdot\mathbf{A}_\mu \\ \mathbf{F}^{\mu\nu} &\equiv (\partial^\mu\mathbf{A}^\nu - \partial^\nu\mathbf{A}^\mu) - \frac{2Q}{\hbar c}(\mathbf{A}^\mu\times\mathbf{A}^\nu) \end{aligned} \tag{2.4}$$

Just by imposing local gauge invariance, one gets the electroweak interactions mediated by four gauge fields, which correspond to four gauge bosons. In the unified electroweak theory those four gauge bosons are not the mass eigenstates of the actual observed electromagnetic and weak gauge bosons. According to the theory of Glashow Salem and Weinberg [4, 5], the two charged weak gauge fields mix into the known $W^\pm$ and the neutral weak gauge field together with the electromagnetic vector field form the neutral Z^0 and γ.

There is a caveat to it. The gauge bosons of the weak interactions are known to have a mass, which is non-zero. A solution to this problem is provided by the Higgs Mechanism, which is introduced in the following.

2.1.3 The Higgs mechanism

The mechanism, which gives mass to the particles, is based on the combination of spontaneous symmetry breaking and local gauge invariance. One considers a complex scalar field $\phi = \phi_1 + i\phi_2$ and a potential with a continuous symmetry, e.g. $\mathscr{U} = -\frac{1}{2}\mu^2(\phi^*\phi) + \frac{1}{4}\lambda^2(\phi^*\phi)^2$. By reformulating the fields into $\eta \equiv \phi_1 - \mu/\lambda$ and $\xi \equiv \phi_2$, or in other words by choosing a special ground state, the rotational symmetry is spontaneously broken. This alone only leads to massless particles called 'Goldstone bosons'. But if one then imposes local gauge invariance, the gauge fields actually acquire mass.

In the SM the Higgs Mechanism is responsible for the masses of e.g. the weak gauge bosons. Since the details are still subject to speculation, the potential $\mathscr{U}$, which was introduced above, is somewhat arbitrary, but it has to be quartic in the fields for the theory to remain renormalizable [1].

2.1.4 Quantum Chromodynamics

Analogically to the electroweak theory, the strong interaction starts with the free Dirac Lagrangian for the three colours.

$$\begin{aligned} \mathscr{L} &= i\hbar c\bar{\psi}\gamma^\mu\partial_\mu\psi - mc^2\bar{\psi}\psi \qquad (2.5) \\ \psi &\equiv \begin{pmatrix} \psi_r \\ \psi_g \\ \psi_b \end{pmatrix} \end{aligned}$$

Equation 2.5 is invariant under global U(3) symmetry, which can be written as a combination of U(1) and SU(3): $\psi \to U\psi$ with $U = e^{i\theta}e^{-iq'\boldsymbol{\lambda}\cdot\boldsymbol{\phi}/\hbar c}$. With $\boldsymbol{\lambda}$ being the eight Gell-Mann matrices. The U(1) symmetry leads to the already known electromagnetic interaction. Demanding local gauge invariance for the SU(3) symmetry, the Lagrangian for the strong interaction reads:

$$\begin{aligned} \mathscr{L} &= [i\hbar c\bar{\psi}\gamma^\mu\partial_\mu\psi - mc^2\bar{\psi}\psi] - \frac{1}{16\pi}\mathbf{F}^{\mu\nu}\cdot\mathbf{F}_{\mu\nu} - (q'\bar{\psi}\gamma^\mu\boldsymbol{\lambda}\psi)\cdot\mathbf{A}_\mu \qquad (2.6) \\ \mathbf{F}^{\mu\nu} &\equiv \partial^\mu\mathbf{A}^\nu - \partial^\nu\mathbf{A}^\mu - \frac{2q'}{\hbar c}(\mathbf{A}^\mu\times\mathbf{A}^\nu) \end{aligned}$$

There are eight massless vector gauge fields in Equation 2.6 corresponding to the eight gluons, which mediate the strong interaction. The coupling constant q' is the strong analogue to the electromagnetic charge q in Equation 2.3.

2.1.5 Running couplings

When considering higher order processes, one finds that the theories have to be renormalized in order to absorb divergences. This is done by introducing a cutoff scale and defering critical terms into the coupling constants, which in turn become functions of the momentum transfer of the reaction. Other than for QED, where the coupling increases with higher momentum transfer, the QCD running coupling decreases at short distances. This phenomenon is also known as 'asymptotic freedom'.

2.2 Why go beyond the Standard Model?

Although the SM is an extremely successful and very well tested theory, it nevertheless has some shortcomings. There are a number of experimental observations, which the SM fails to describe, e.g.:

- neutrino masses and mixing [1, 6]
- matter / antimatter asymmetry [1, 7]
- cold dark matter [2, 8, 9]
- dark energy [2, 10]

In addition to this (not complete) list of experimental shortcomings, the SM also has some theoretical problems. It does not explain, why there are exactly three families of fermions, neither does it explain the fermion masses and mixing angles, nor the size of the gauge couplings. Another striking reason, why one generally believes that there must be a bigger underlying theory, is that the gravitational interaction is not included in the SM. This implies, that a new theory is needed at the latest, when quantum gravitational effects become important at the reduced Planck Scale $M_P = (8\pi G_N)^{-1/2} = 2.4 \times 10^{18}$ GeV [11]. In this respect, the SM should be seen as an effective theory for the low energy regime.

Furthermore, the running couplings of the electroweak and strong interaction point to the possibility of a unification of couplings and therefore the interactions at high energies. But this cannot be accomplished by the SM.

The hierarchy problem

Another unsolved issue in the Standard Model is the so-called "hierarchy problem". This is not a problem of the theoretical structure of the SM, but the SM fails to address it. From experimental constraints it is known, that the Higgs mass squared should be in the order of $m_H^2 \sim O(100\text{GeV})^2$ [11]. Unfortunately, this value is subject to huge quantum corrections, which arise especially, if one assumes new physics (coupling to the Higgs field) at a certain energy scale. If Λ_{UV} denotes the ultraviolet momentum cutoff, which is interpreted as at least the energy, at which new physics become relevant [11], the correction is $\Delta m_H^2 \sim \Lambda_{UV}^2$. Since Λ_{UV} is usually taken not very far below M_P, the correction is $O(10^{30})$ times larger than the value of m_H^2 itself and since all massive particles of the SM couple to the Higgs boson, the entire mass spectrum is sensitive to the correction. Even if one dismisses the use of the cutoff, the correction term will still be proportional to the squared mass of the heaviest particle the Higgs couples to (directly or indirectly) and therefore will either way be large [11].

The hierachy problem may be solved in a number of ways. One e.g. can assume that there is no new high mass particle or effect, which couples to the Higgs field. But this contradicts the argument for the existence of new physics at least at M_P, which was given before. Another possibility is far more attractive. If somehow the different contributions to Δm_H^2 could cancel each other naturally, the problem would cease to exist. This solution can be implemented in the theory of Supersymmetry, which will be discussed in the following.

Names	spin 0	spin 1/2
squarks, quarks (× 3 generations)	$(\tilde{u}_L\ \tilde{d}_L)$ $\tilde{u}_R^*$ $\tilde{d}_R^*$	$(u_L\ d_L)$ $u_R^\dagger$ $d_R^\dagger$
sleptons, leptons (× 3 generations)	$(\tilde{\nu}\ \tilde{e}_L)$ $\tilde{e}_R^*$	$(\nu\ e_L)$ $e_R^\dagger$
Higgs, higgsinos	$(H_u^+\ H_u^0)$ $(H_d^0\ H_d^-)$	$(\tilde{H}_u^+\ \tilde{H}_u^0)$ $(\tilde{H}_d^0\ \tilde{H}_d^-)$

Table 2.3: SM fermions and their superpartners in the MSSM together with the extended Higgs sector.

Names	spin 1/2	spin 1
gluino, gluon	$\tilde{g}$	g
winos, W bosons	$\tilde{W}^\pm\ \tilde{W}^0$	$W^\pm\ W^0$
bino, B boson	$\tilde{B}^0$	B^0

Table 2.4: SM gauge bosons and their superpartners in the MSSM.

2.3 Supersymmetry

The space-time symmetry, that relates fermions to bosons and therefore naturally leads to a cancelling of the corrections to m_H^2, is called Supersymmetry (SUSY) (e.g. [12, 13, 11]). This summary is largely based on the 'Supersymmetry Primer' by S. Martin [11].

The transformation operator Q turns a fermion into a bosonic superpartner and vice versa:

$$\begin{aligned} Q|\text{Boson}\rangle &= |\text{Fermion}\rangle \\ Q|\text{Fermion}\rangle &= |\text{Boson}\rangle \end{aligned} \tag{2.7}$$

Since Q commutes with the mass operator and with the gauge operators, the superpartners must have the same mass and the same charge, weak isospin and colour degrees of freedom [11]. In the Minimal Supersymmetric Standard Model (MSSM), every SM particle has a superpartner (sparticle) with a spin differing by 1/2, with which it forms a supermultiplet. The MSSM is the minimal extension of the SM, that is necessary to accommodate SUSY. The new spin 0 sparticles (sfermions) and their SM partners are listed in Table 2.3 together with the extended Higgs sector of the MSSM. This extension is necessary, since it needs two chiral supermultiplets for the Higgs sector in order to preserve the cancellation of corrections to m_H^2 [11]. There are separate partners for left- and right-handed fermions. But for the sparticles this distinction is evidently not related to their helicity. The new spin 1/2 sparticles (gauginos) are superpartners to the SM gauge bosons and are listed in Table 2.4. It should be noticed, that the gauge eigenstates in Tables 2.3 and 2.4 are not necessarily the observed mass eigenstates, because of the mixing after electroweak (EW) symmetry breaking. Via the new sparticles that enter the spectrum, the gauge couplings are far more likely to unify at some high energy near the GUT scale, than in the SM.

2.3.1 R-Parity

The MSSM would in principal allow for lepton and baryon number violation, leading e.g. to rapid proton decay, which is not observed. In order to solve this issue, a new multiplicative quantum number is introduced, which is called R-Parity: $P_R = (-1)^{3(B-L)+2s}$, with B, L and s being the baryon number, lepton number and the spin. P_R does not commute with the SUSY operators Q and $Q^\dagger$. Consequently, particles are R-Parity even, while sparticles are R-Parity odd objects. Conservation of R-Parity prevents the afore mentioned problems. It also means, that the lightest Supersymmetric Particle (LSP) must be stable. If the LSP is electrically neutral, it would be a good dark matter candidate, solving another issue, which the SM fails to answer. Other consequences of R-Parity conservation are related to the expected signatures at collider experiments. It implies, that sparticles subsequently will decay into the LSP and that the sparticles are produced in even numbers.

2.3.2 SUSY breaking

As already mentioned, the new sparticles should have the same masses as their SM partners, if SUSY is an unbroken symmetry. This implies, that there should be a 511 keV selectron, which definitely would have been discovered until now. Since that is not the case, it is clear, that SUSY must be broken. The important question is, how the breaking of SUSY is realized. In order to still provide a solution to the hierarchy problem, the relationships between the dimensionless couplings must be preserved [11]. That means, there is an extra breaking term in the SUSY Lagrangian. The mechanism is known as "soft" SUSY breaking. The symmetry is hereby spontaneously broken (c.f. the Higgs mechanism). Generally, the masses of the superpartners are expected to be not too large and the lighter ones are expected to be below ~ 1 TeV and therefore well in the range of the LHC. The breaking, which is introduced into the Lagrangian explicitly in the MSSM, introduces a great deal of arbitrariness into the SUSY model. There are 105 new parameters in the MSSM with respect to the SM, which are all due to the soft breaking term and not due to SUSY itself. Luckily, there are experimental constraints, which allow to relate some of the parameters and help to reduce the arbitrariness.

The breaking happens in a so-called "hidden sector" of particles with no direct coupling to the visible supermultiplets [11]. There are a number of models for the sort of communication between the hidden sector and the MSSM sparticles. Two of them are regarded to be the most popular concepts.

Gravitational-mediated SUSY breaking

In this model the breaking sector is connected via gravitational interactions, which is why it is also known as minimal supergravity or mSUGRA scenario. Following the renormalization group evolution down to the EW scale [11], the MSSM spectrum is described by only five new parameters: The generalized sfermion and gaugino masses $m_{1/2}$ and m_0, the ratio of the

Names	Gauge Eigenstates	Mass Eigenstates
Higgs bosons	$H_u^0\ H_d^0\ H_u^+\ H_d^-$	$h^0\ H^0\ A^0\ H^\pm$
squarks	$\tilde{u}_L\ \tilde{u}_R\ \tilde{d}_L\ \tilde{d}_R$	(same)
	$\tilde{s}_L\ \tilde{s}_R\ \tilde{c}_L\ \tilde{c}_R$	(same)
	$\tilde{t}_L\ \tilde{t}_R\ \tilde{b}_L\ \tilde{b}_R$	$\tilde{t}_1\ \tilde{t}_2\ \tilde{b}_1\ \tilde{b}_2$
sleptons	$\tilde{e}_L\ \tilde{e}_R\ \tilde{\nu}_e$	(same)
	$\tilde{\mu}_L\ \tilde{\mu}_R\ \tilde{\nu}_\mu$	(same)
	$\tilde{\tau}_L\ \tilde{\tau}_R\ \tilde{\nu}_\tau$	$\tilde{\tau}_1\ \tilde{\tau}_2\ \tilde{\nu}_\tau$
neutralinos	$\tilde{B}^0\ \tilde{W}^0\ \tilde{H}_u^0\ \tilde{H}_d^0$	$\tilde{N}_1\ \tilde{N}_2\ \tilde{N}_3\ \tilde{N}_4$
charginos	$\tilde{W}^\pm\ \tilde{H}_u^+\ \tilde{H}_d^-$	$\tilde{C}_1^\pm\ \tilde{C}_2^\pm$
gluino	$\tilde{g}$	(same)
gravitino	$\tilde{G}$	(same)

Table 2.5: Gauge and mass eigenstates of the MSSM sparticle spectrum and the extended Higgs sector [11].

Higgs vacuum expectation values tanβ, the trilinear coupling A_0 and the sign of the Higgs mass term sign(μ).

Gauge-mediated SUSY breaking

The other popular alternative assumes, that the breaking is communicated via ordinary gauge interactions. This includes also gravitational portion, but it is negligible compared to the other components. The number of free new parameters is reduced to six in this model [11].

2.3.3 Mass spectrum of the MSSM

As mentioned before, the gauge eigenstates of the MSSM mix into the observable mass eigenstates. The neutral Higgsinos $\tilde{H}_u^0$ and $\tilde{H}_d^0$ together with the neutral gauginos $\tilde{B}^0$ and $\tilde{W}^0$ form the neutralinos $\tilde{N}_1\ \tilde{N}_2\ \tilde{N}_3\ \tilde{N}_4$, while the charged Higgsinos and Winos result in the charginos $\tilde{C}_1^\pm\ \tilde{C}_2^\pm$. The gauge eigenstates of the gluinos are also their mass eigenstates and the mixing of the first two generations of squarks and sleptons are negligible. The details of the mixing and the names of the mass eigenstates are listed in Table 2.5.

Although the details of the MSSM mass spectrum depend on the SUSY breaking mechanism, there are some general expectations about the hierarchy [11]. In most models the lightest neutralino $\tilde{N}_1$ is expected to be the LSP and serves as a candidate for cold dark matter. The gluinos are generally expected to be heavier than the lighter neutralinos and charginos. While $\tilde{t}_1$ and $\tilde{t}_2$ are most probably the lightest squarks, the squarks of the first and second generations are expected to be heavier than the sleptons. Among them, the $\tilde{\tau}_1$ is probably the lightest charged one and the left handed selectrons and smuons should be heavier than their right-handed counterparts. The lightest neutral Higgs boson h_0 is expected to be not heavier than 150 GeV, while the masses of the other Higgs bosons can be much bigger.

Because of the dependency on the SUSY breaking mechanism, the measurement of SUSY masses and mixing angles will be a tool to unveil the nature of the breaking.

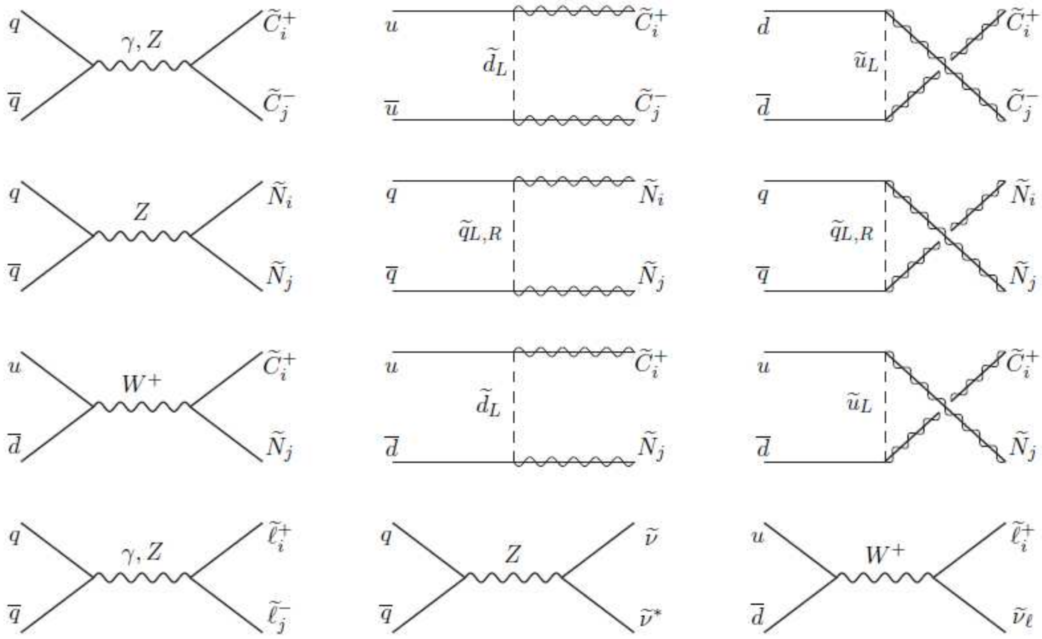

Figure 2.1: Feynman diagrams of the electroweak production channels for the MSSM sparticles. Taken from [11].

2.3.4 Expected signatures at the LHC

Although there are indirect signals of new physics, which may point to SUSY, e.g. rare forbidden processes like $\mu \to e\gamma$ or virtual sparticle effects like the anomalous magnetic moment of the muon, the direct detection of SUSY is still the key objective.

As mentioned in the previous sections, sparticles are produced in pairs at colliders (if R-Parity is conserved). Equations 2.8 summarize the possible electroweak and Equations 2.9 the QCD production mechanisms, which are both illustrated in Figures 2.1, 2.2 and 2.3 [11].

$$\begin{array}{lll} q\bar{q} \to \tilde{C}_i^+\tilde{C}_j^-,\ \tilde{N}_i\tilde{N}_j & u\bar{d} \to \tilde{C}_i^+\tilde{N}_j & d\bar{u} \to \tilde{C}_i^-\tilde{N}_j \\ q\bar{q} \to \tilde{l}_i^+\tilde{l}_j^-,\ \tilde{\nu}_l\tilde{\nu}_l^* & u\bar{d} \to \tilde{l}_L^+\tilde{\nu}_l & d\bar{u} \to \tilde{l}_L^-\tilde{\nu}_l^* \end{array} \tag{2.8}$$

$$\begin{array}{lcl} gg & \to & \tilde{g}\tilde{g},\ \tilde{q}_i\tilde{q}_j^* \\ gq & \to & \tilde{g}\tilde{q}_i \\ q\bar{q} & \to & \tilde{g}\tilde{g},\ \tilde{q}_i\tilde{q}_j^* \\ qq & \to & \tilde{q}_i\tilde{q}_j \end{array} \tag{2.9}$$

If R-Parity is conserved, the pair produced sparticles decay via cascades into two LSPs, which, if electrical neutral, will escape detection [3]. Neutralinos and charginos might decay

[3] If the LSP would be charged, it should have been detected already.

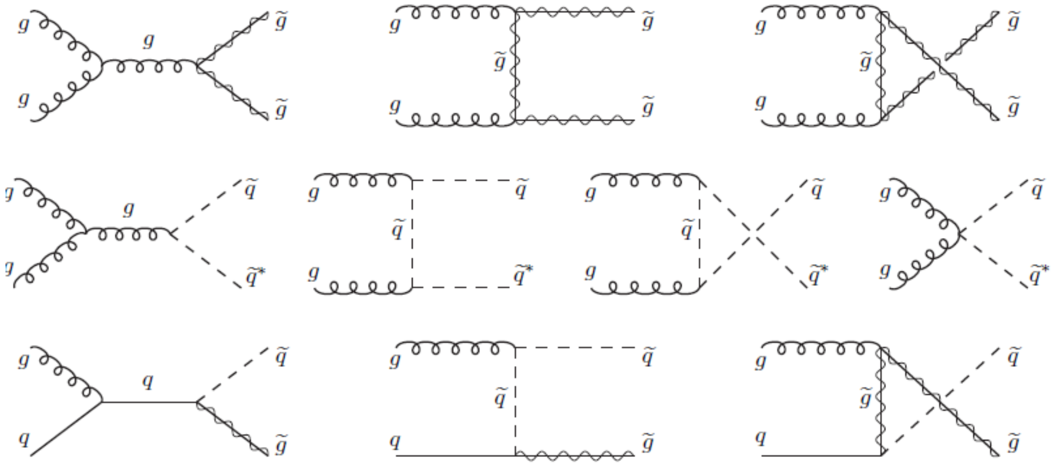

Figure 2.2: Feynman diagrams of the gluon-gluon and gluon-quark fusion production channels for the MSSM sparticles. Taken from [11].

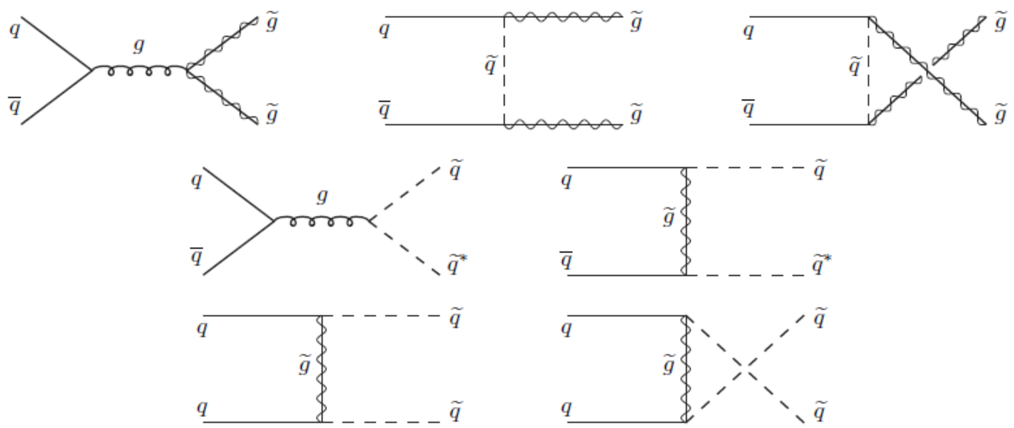

Figure 2.3: Feynman diagrams of the quark-antiquark annihilation production channels for the MSSM sparticles. Taken from [11].

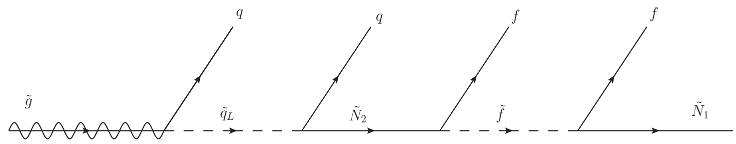

Figure 2.4: Example of a SUSY cascade decay.

into a gauge boson and a lighter neutralino or chargino, as well as into lepton+slepton or quark+squark. The sleptons decay also via two body decays into a lepton and neutralino or chargino. Squarks decay dominantly into a quark and a gluino, if this is kinematically allowed. Otherwise they decay into a quark and neutralino or chargino. Gluinos can only decay via squarks, either into quark and squark or, if that is not possible, into quark pairs and a neutralino or chargino. Figure 2.4 shows an example decay chain.

The general signature at the LHC is therefore missing transverse energy and a arbitrary number of leptons and jets. The signature with no isolated leptons, which is also covered in this work, has the advantage of a reduced W + jets SM background.

2.3.5 Standard Model background to SUSY searches

Since the general signature for SUSY is missing transverse energy accompanied by jets and maybe isolated leptons, the SM backgrounds in SUSY searches are manifold. Processes including real $E_{\mathrm{T}}^{\mathrm{miss}}$ like $Z \to \nu\nu$ + jets, $W \to l\nu$ + jets and top production contribute as well as processes, which might suffer from fake $E_{\mathrm{T}}^{\mathrm{miss}}$ like dijet QCD production, where one or more jets are badly measured, and non-collision background.

2.3.6 Experimental constraints on Supersymmetry

This paragraph summarizes the mass limits on the SUSY sparticles in the MSSM previous to the publications of the LHC results. It was assumed, that R-parity is conserved, the squarks are degenerate in mass (except $\tilde{t}$ and $\tilde{b}$), that the gaugino masses unify at the GUT scale and that the lightest neutralino is the LSP. The slepton limits correspond to the lighter $\tilde{l}_R$. The mass limits obtained with 95% confidence level are listed in Table 2.6 as of 2010.

2.4 Split Supersymmetry

The natural solution to the hierachy problem is the motivation for low energy SUSY. Now, if one accepts that there is a large amount of fine tuning realized in nature, this motivation is no longer relevant. SUSY is still needed as an extension of the SM in order to unify the gauge couplings and to provide a dark matter candidate, but it can be broken at a very high scale. This kind of model was first proposed by Wells [14], taken up by Arkani-Hamed et al. [15] and drew quite some attention since [16, 17]. As a consequence of the high breaking scale, the scalars in the Supersymmetric Standard Model become very heavy (except one Higgs) [15]. The new fermions on the other hand can stay light, since they are protected by a chiral symmetry and therefore can account for the unification of gauge couplings. The mass gap

Particle	Mass limit [GeV]	Constraints
$\tilde{N}_1^0$	46	all $tan\beta$, m_0, $m_{\tilde{N}_2^0} - m_{\tilde{N}_1^0}$
$\tilde{N}_2^0$	62.4	$1 < tan\beta < 40$, all m_0 and $m_{\tilde{N}_2^0} - m_{\tilde{N}_1^0}$
$\tilde{N}_3^0$	99.9	$1 < tan\beta < 40$, all m_0 and $m_{\tilde{N}_2^0} - m_{\tilde{N}_1^0}$
$\tilde{N}_4^0$	116	$1 < tan\beta < 40$, all m_0 and $m_{\tilde{N}_2^0} - m_{\tilde{N}_1^0}$
$\tilde{C}_1^\pm$	94	$1 < tan\beta < 40$, $m_{\tilde{C}_1^\pm} - m_{\tilde{N}_1^0} > 3$ GeV , all m_0
$\tilde{e}$	107	all $m_{\tilde{e}_R} - m_{\tilde{N}_1^0}$
$\tilde{\mu}$	94	$1 \leq tan\beta \leq 40$, $m_{\tilde{\mu}_R} - m_{\tilde{N}_1^0} > 10$ GeV
$\tilde{\tau}$	81.9	$m_{\tilde{\tau}_R} - m_{\tilde{N}_1^0} > 15$ GeV, all θ_τ
$\tilde{q}$	379	$tan\beta = 3$, $\mu > 0$, $A_0 = 0$, any $m_{\tilde{g}}$
$\tilde{b}$	89	$m_{\tilde{b}_1} - m_{\tilde{N}_1^0} > 8$ GeV, all θ_b
$\tilde{t}$	95.7	$\tilde{t} \to c\tilde{N}_1^0$, $m_{\tilde{t}} - m_{\tilde{N}_1^0} > 10$ GeV, all θ_t
$\tilde{g}$	308	any $m_{\tilde{q}}$
	392	$m_{\tilde{q}} = m_{\tilde{g}}$

Table 2.6: 95% confidence level mass limits for the MSSM sparticle content [2].

between the scalars and the fermions motivated the name "Split Supersymmetry" for this kind of model.

The concept of Split SUSY can be incorporated into the MSSM with conserved R-Parity. This time though the motivation for R-Parity is the explanation of neutrino masses and not the fixing of rapid proton decay (which is intrinsically prevented in Split SUSY) [15]. A striking feature is the long life-time of the gluino. Since it can only decay into a quark anti-quark pair via virtual squark exchange, the high squark mass results in a long lived gluino. A typical gluino, that was produced at the LHC, would then decay outside of the detector [15] and would therefore be regarded as stable in any analysis.

R-hadrons

The gluino production proceeds via the usual channels, which were already mentioned in Equation 2.9. Because of the long life-time, the gluinos hadronize. They form bound states with SM gluons and quarks, so-called R-hadrons, which can be both electrically neutral or charged. The mass prediction ranges from 100 GeV up to a few TeV [18]. When looking for R-hadron signatures in the detector, it is important to understand, how they interact with matter. The R-hadron can be interpreted as a heavy non-interacting coloured state accompanied by a hadronic coloured cloud, which is responsible for the interaction [18]. Nuclear interactions typically lead to a small energy loss of $\lesssim 2$ GeV [18], but during that, the R-hadron may change its electrical charge and or baryon number, by picking up quarks or anti-quarks.

2.4.1 Signatures

Because of the low energy loss in nuclear interactions, a R-hadron can either leave a muon like signature, provided it is electrically charged at some point (at least in the muon system), or it can lead to fake $E_{\mathrm{T}}^{\mathrm{miss}}$, if it is neutral (most of the time). If in the later case, the $E_{\mathrm{T}}^{\mathrm{miss}}$ is accompanied by an additional jet, R-hadrons would lead to the monojet signature. This was proposed in [19] for the discovery of neutral R-hadrons and is investigated in Chapter 7. The Feynman diagrams for gluon fusion processes leading to a monojet signature are shown in Figure 2.5. This is the dominant production process for gluino masses below 500 GeV. An additional hard jet is more likely to be produced via inital state than via final state radiation.

2.4.2 Experimental constraints

Prior to the results from ATLAS, the latest limit on the gluino mass in the Split SUSY model was set by the CMS collaboration [20]. Stable gluinos with mass lower than 398 GeV are excluded at 95% confidence level, if they leave a track in the inner detector and the muon system. If the track in the muon system is missing, the lower limit on the gluino mass is set at 311 GeV [20]. In both cases the R-hadron has to be charged, at least inside the inner detector in order to leave a charged track. The limits do not include the case of a completely neutral R-hadron.

2.5 Event simulation

In order to compare the data collected by the experiment to the theoretical predictions, so-called Monte Carlo generators are employed. They use the knowledge of the underlying theories to generate pseudo events. This section describes - very briefly - the mechanisms and introduces the main generators used in this thesis. A more detailed description on the principle of event generation can be found e.g. in [21].

Figure 2.6 shows the basic structure of the event simulation. The individual steps are explained in the following.

Since individual partons within the protons collide at the LHC, the momentum fraction of the partons influences the cross section of the process. This cannot be calculated perturbatively. Instead, a global fit to experimental data is used to determine the so-called parton density distribution functions (PDFs). The experimental data includes deep inelastic scattering, Drell-Yan and jet production.

The hard subprocess is modeled via the matrix element of the underlying theoretical description of the process. Depending on the capability of the generator it is computed at leading order (LO) or higher order (N^{x}LO).

In order to estimate higher-order corrections and to generate high-multiplicity final states the so-called parton shower mechanism is used. The parton showering models the radiation of gluons from accelerated coloured particles via fragmentation probability functions. Care has to be taken in order to avoid double counting of jets created in the hard subprocess and in the parton showering.

The coloured objects are then hadronized with (anti-)quarks from the vacuum into colour neutral objects. For all non stable objects the decays are simulated according to the theoretical probabilities. This way, the simulation yields to observable objects in the final state. Furthermore, the generators might simulate the underlying event, which consists of beam remnants, interactions including partons other than the ones involved in the hard subprocess and

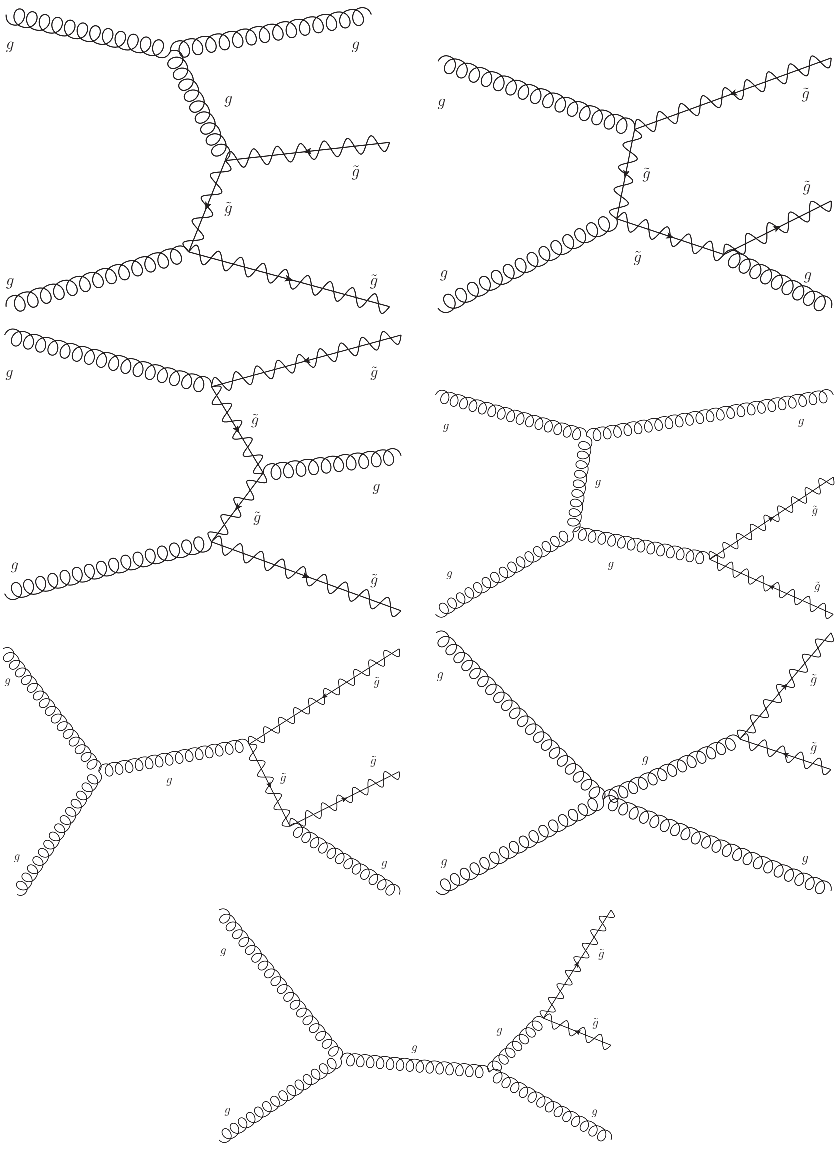

Figure 2.5: Feynman diagrams of the gluon fusion Split SUSY production with one extra jet in the final state.

parton distributions (PDFs)

$\Downarrow$

hard subprocess

$\Downarrow$

parton shower

$\Downarrow$

hadronization

$\Downarrow$

decay

Figure 2.6: Basic structure of a Monte Carlo event generator

additional collisions of other protons inside the beams (pile-up).

There are two basic kind of generators: Cross section generators, which only include the PDF and hard subprocess, and event generators, which include the full simulation chain until the observable final state.

The following generators are the main ones used in the analyses.

`Pythia`[**22**] is a general purpose event generator featuring many built in $2 \to n$ subprocesses, most of which are either $2 \to 2$, $2 \to 1$ or $2 \to 3$. Initial and final state parton showering is simulated as well as the underlying event, the hadronization and the decay of the final state particles.

`Herwig`[**23, 24**] like `Pythia` is a general purpose event generator covering many possible hard $2 \to n$ subprocesses . It includes initial and final state parton showering, hadronization and decays. It is possible to use `JIMMY` [25] for the underlying event simulation. The C^{++} version (`Herwig++`) features a new parton shower and an improved cluster hadronization model.

`ISAJET`[**26**] is also a general purpose event generator, which includes a great variety of SUSY models. It is therefore primarily used for the generation of SUSY mass spectra via its independent `ISASUSY` routine.

`Alpgen`[**27**] is designed for large jet multiplicities in the final state. Its leading order matrix element algorithm can calculate processes up to $2 \to 5$. For parton showering and hadronization it has to be interfaced with `Herwig` or `Pythia`.

`MC@NLO`[**28**] includes full NLO QCD corrections for the hard process. Therefore, only a limited number of subprocesses are available. It has to be interfaced with `Herwig` for the showering and hadronization.

`PROSPINO` [**29**] is a cross section generator, which provides NLO predictions for SUSY production processes.

`FEWZ` [**30**] is a dedicated cross section generator for the Drell-Yan process at hadron colliders, which is calculated including NNLO QCD corrections.

Chapter 3

The experiment

This chapter introduces very briefly the Large Hadron Collider and the ATLAS detector. For the detector the emphasize is on the parts which are of major importance for the analysis carried out in this work. A complete overview can be found e.g. in [31] or [32]. This chapter is largely based on the summary article in [33].

3.1 The Large Hadron Collider (LHC)

Technical aspects

The LHC succeeded the LEP accelerator at CERN and was even built in the same tunnel after LEP was dismounted. The tunnel has a circumference of 27 kilometers and is located at the outskirts of Geneva 50 to 175 meters underground the border region between France and Switzerland (c.f. Figure 3.1). In Figure 3.1 also the location of the four main LHC experiments is shown. The two multipurpose experiments ATLAS and CMS [35] are accompanied by the two smaller experiments ALICE [36] and LHC-b [37]. LHC-b is a dedicated b- and c-physics precision experiment while ALICE is an experiment specially built for heavy ion collisions. The LHC represents the latest development in collider technology and is today the collider with the highest center-of-mass energy. The development of the center-of-mass energies over time can be seen on Figure 3.2. The design energy for the LHC is 7 TeV per beam but due to an incident in 2009 the energy was reduced to 3.5 TeV per beam for the first few years of data taking.

The LHC is a proton-proton collider. Other than the Tevatron, which is a proton-antiproton collider, the LHC is not limited in luminosity due to the difficulty of producing antiprotons, but the proton-proton design requires two separate beam pipes. Also comparing to electron-positron colliders there are many advantages. Since protons loose far less energy due to synchrotron radiation, the achievable center-of-mass energies are much higher and because the partons rather than the protons themselves collide, one can study a wide energy range simultaneously without precise tuning. Colliding hadrons is also the only way to investigate parton-parton collisions including gluon-gluon reactions. Furthermore, one has the advantage of the greater variety of initial quantum numbers. Of course these aspects also come with a number of challenges. One has to deal with complicated final states because of multiple parton interactions. Furthermore, in contrast to e.g. *ee* collisions, the centre-of-mass

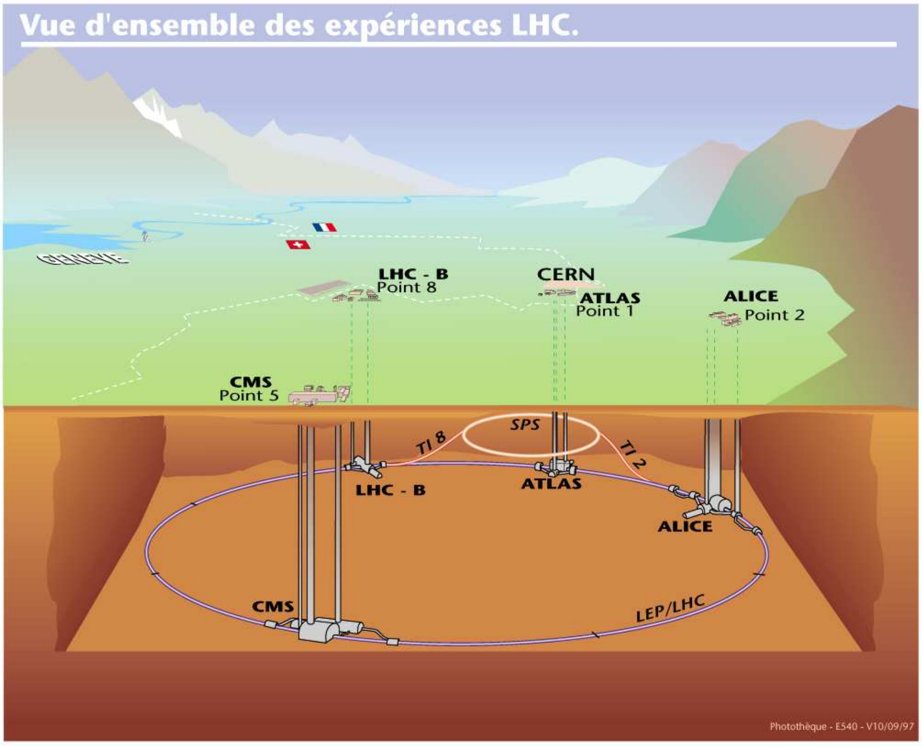

Figure 3.1: Overview map of the LHC and its experiments. Taken from [34].

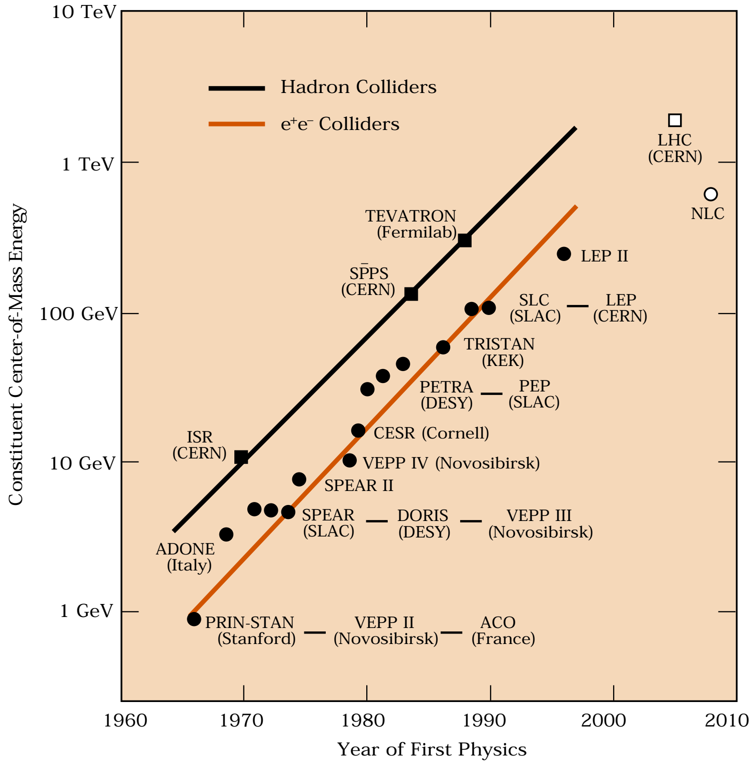

Figure 3.2: Livingston Plot: Center-of-mass energies of the experiments plotted against time. Taken from [38].

frame of the parton-parton system is not identical with the laboratory frame. In addition the cross section of soft physics events is huge and this has to be dealt with, when searching for new physics.

The unprecedented center-of-mass energy also requires unprecedented technical complexity. E.g. for bending the two proton beams around the ring 1232 superconducting dipoles are used, which require a massive amount of cooling resources and are capable of producing magnetic fields up to 8.33 Tesla. These dipole magnets and their infrastructure were also the main budget item of the LHC machine.

Furthermore, the large instantaneous LHC luminosity [1] is a big challenge. When reaching its full capabilities it will go up to $10^{34}\text{cm}^{-2}\text{s}^{-1}$. The LHC will operate with a bunch crossing rate of 40 MHz which is equivalent to a bunch spacing of 25 ns. Since this implies that the particles originating from one collision cannot travel through the whole detector until the next collision happens, the challenges to the trigger system of the detectors are huge.

Purpose and philosophy
The primary goal of the LHC is to serve as discovery machine. G. Kane even takes it a step further and calls the LHC a 'why machine' that will lead to a better understanding why things are the way they are [33]. Indisputable the LHC will enlarge our understanding of particle physics to a huge amount.

There is reasonable hope to find answers to fundamental questions, which are not addressed by the Standard Model. Among the most pressing ones is to find the origin of the particle masses or in other words the search for the Higgs boson. Until now there are only indirect hints for its existence but the LHC should enable us to really directly observe the manifestation(s) of the Higgs field. Equal in priority is the search for a dark matter candidate, especially the search for Supersymmetry, which is also the subject of this work.

Other than at LEP it will be much more difficult - as explained above - to do precision measurements. Nevertheless, it is possible and especially for heavy quark systems this is also one of the LHC goals stated in [31]. Among these objectives are the study of CP-violation in the B_d^0 system, the angles in the CKM unitarity triangle, $B\bar{B}$ mixing in the B_s^0 system, rare B decays and general spectroscopy of states with b-quarks.

3.2 The ATLAS detector

As one of the two general purpose detectors at the LHC the ATLAS detector should be able to provide access to as many physics signatures as possible. Furthermore, it should be able to handle luminosities up to $10^{34}\text{cm}^{-2}\text{s}^{-1}$ but at the same time should perform well with the much lower initial luminosity delivered by the LHC in the first few months of operation. Following these requirements the design of the detector was optimized according to a great variety of possible new physic discoveries as well as precision measurement objectives [31].

The search for the Higgs - the Standard Model Higgs Boson as well as the extended MSSM

[1] The instantaneous luminosity is defined as the ratio of the event rate dN/dt and the cross section σ: $d\mathcal{L}/dt = dN/dt \cdot 1/\sigma$. Later in this work, what is denoted with $\mathcal{L}$ is the integrated luminosity over a certain time.

Higgs Sector - was used as first benchmark for the detector optimization. Various signatures of possible Higgs decays drove the requirements to the detector. But also the searches for supersymmetric particles were a major driving force of the detector design and its optimization. The search for the lightest supersymmetric particle e.g. sets high demands on the hermeticity and $E_{\mathrm{T}}^{\mathrm{miss}}$ capability of the detector. The search for new heavy gauge bosons set the requirement for the high-resolution lepton measurement and charge identification capabilities at high transverse momentum. Searches for quark compositeness demand very high p_{T} jet measurement ability and the b-quark precision measurements obviously lead to the need for precise secondary vertex determination, full reconstruction capabilities of low p_{T} final states and low p_{T} lepton triggers.

All in all the detector should provide sensitivity to a great variety of final states, that set very different requests to its design, but the basic design can be summarized as follows. It has a very good electromagnetic calorimeter for electron and photon identification and measurement as well as a hermetic hadron calorimeter for jet and missing transverse energy measurement. The efficient tracking works also at very high luminosity, which enables precise lepton measurement, b-tagging, electron and photon identification as well as tau and heavy-flavour vertexing. The muon system, which can even be operated in a stand-alone mode, allows for precision muon momentum measurement up to very high luminosity and at the same time is capable of triggering very low p_{T} muons, which is necessary for the early time of operation with low instantaneous luminosity.

Figure 3.3 gives an overview of the detector. Naively one would assume that a sphere would be the best shape but the realization of the uniform magnetic fields leads to the cylinder geometry, so that the detector consists of a central barrel and two end-cap parts [2] . Its different components are described in more detail in the following.

3.2.1 Detector subsystems

Magnet systems

To allow transverse particle momentum measurement the inner detector is surrounded by a superconducting solenoid, which is aligned along the beam axis. It delivers an axial magnetic field of 2 Tesla and is located in front of the electromagnetic calorimeter. In order to minimize the amount of material and therefore the radiative thickness it shares a common vacuum vessel with the electromagnetic calorimeter.

For the momentum measurement in the muon system a toroidal magnet geometry is used. This is carried out as a large superconducting air core toroid outside the calorimeters. The system is divided into a barrel toroid and two end-cap toroids. It delivers a magnetic field of approximately 0.5 Tesla in the central barrel and 1 Tesla in the end cap region. The open structure allows for a huge area of the magnetic field but also requires a very detailed field mapping due to the eightfold geometry in order to accurately measure the muon momentum.

[2] ATLAS uses a right-handed coordinate system with its origin at the nominal interaction point (IP) in the centre of the detector and the z-axis coinciding with the axis of the beam pipe. The x-axis points from the IP to the centre of the LHC ring, and the y axis points upward. Cylindrical coordinates (r, ϕ) are used in the transverse plane, ϕ being the azimuthal angle around the beam pipe. The pseudorapidity is defined in terms of the polar angle θ as $\eta = -\ln\tan(\theta/2)$.

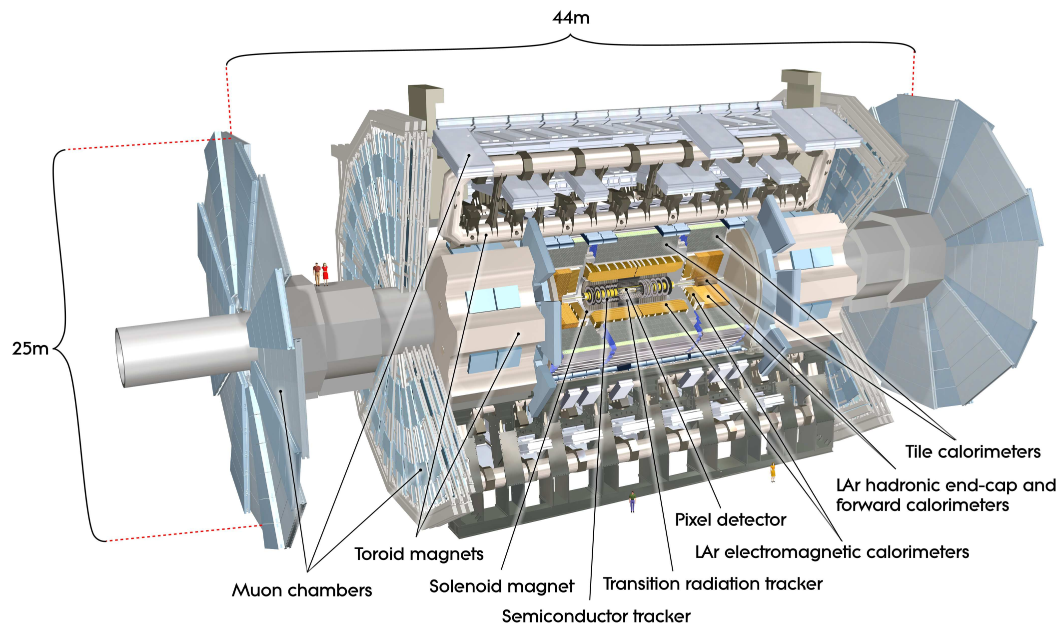

Figure 3.3: Computer generated overview of the ATLAS detector. Taken from [39].

Inner detectors

The collisions delivered by the LHC every 25 ns will result in a very high track density. The requirements on momentum and vertex resolution mentioned above demand a very fine detector granularity for the inner detector system. The main challenges for the design and construction were the high particle rates, radiation hardness of the detector components and the control of their aging effects. All that required several years of R&D iterations.

Figure 3.4 shows overviews of the inner detector components. They are contained inside the magnetic field of the solenoid and provide efficient tracking of charged particles within a range of $|\eta| < 2.5$.

Located closest to the interaction point there are layers of silicon pixel detectors with a cell size of $50 \times 400\ \mu\text{m}^2$. Their innermost layer is at around 5 cm as close to the interaction point as possible to improve the measurement of secondary vertices. It covers approximately 2 m^2 and has 80 million channels to be read out. Although being most accurate the pixel technology is also the most expensive one and has a very high power density. Because of that, the next layers of the inner detector use silicon microstrip technology. Divided into a barrel section and two end-cap discs, this system covers a range of $|\eta| < 2.5$. The strip dimension of $10-12 \times 80-120\ \mu\text{m}^2$ results in an estimated occupancy of a few percent per bunch crossing. In order to improve the resolution in z-direction, some strips are placed at a stereo angle of 40 mrad with respect to the beam axis. For the outermost layer at radii greater than 56 cm one can abandon the expensive silicon technology and relies on a tracker made of $3 \cdot 10^5$ straw tubes filled with a xenon based gas. It provides typically 36 hits per track and allows tracking with less material per point and even has electron identification capability via the detection

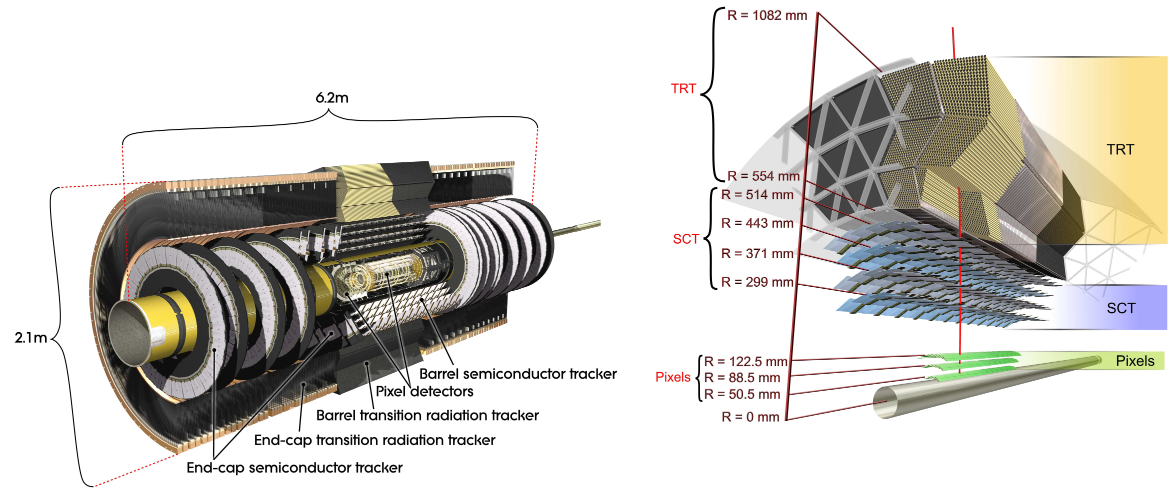

Figure 3.4: Computer generated views of the ATLAS inner detector system. Taken from [40].

of transition radiation.

Calorimetry

This paragraph contains a little bit more detailed description also in terms of numbers, because the main objects of the analysis, namely jets and missing transverse energy, are measured in the calorimeters. The calorimetry of ATLAS can be divided into two main parts: The electromagnetic and the hadronic calorimeters. This can also be seen on Figure 3.5, which shows a computer generated overview of the calorimeter systems. The separation into the two main parts is needed for the separation of electrons and gammas from jets. The first two are mostly contained in the electromagnetic calorimeter, while jets deposit part of their energy also in the hadronic calorimeter.

The electromagnetic calorimeter should provide a good energy resolution as well as position and direction measurements and a wide geometric coverage. It consists of a barrel and two end-cap parts. The barrel section shares the cryostat with the solenoid and the two end-cap parts share their cryostats with the hadronic end-cap and forward calorimeters. All three sections use sampling technology with absorbers made from lead and liquid argon at a temperature of 89 Kelvin as active detection material. It covers a geometric range of $|\eta| < 3.2$ and has an “accordion” like shape that leads to complete azimuthal symmetry without uninstrumented regions. In order to correct for energy losses a so-called presampler is installed in front of the calorimeter over $|\eta| < 1.8$. Table 3.1 shows detailed information about the coverage, granularity and readout channels.

The hadronic calorimeters emphasis is on the accurate measurement of the jet energy and full coverage in order to describe the missing transverse energy correctly. The barrel part of the hadronic calorimeter, which itself is subdivided into central barrel and two extended barrel regions, is also a sampling calorimeter but uses iron absorbers and plastic scintillator tiles.

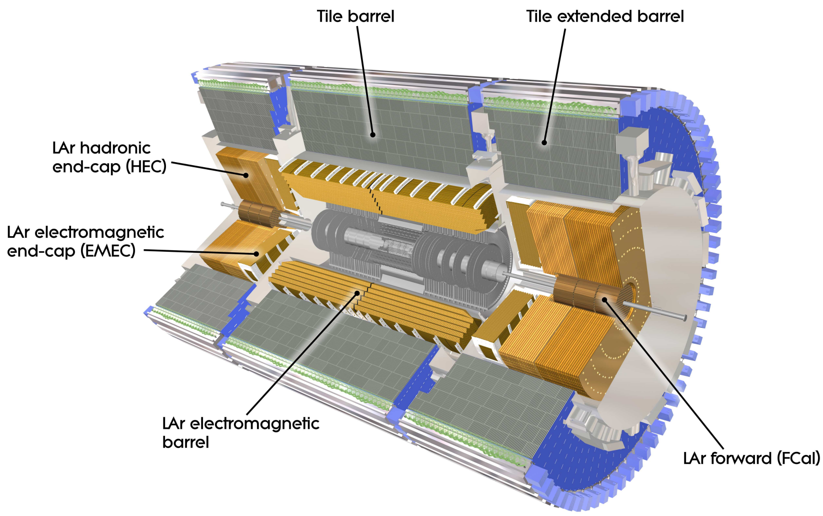

Figure 3.5: Computer generated overview of the ATLAS calorimeters. Taken from [41].

	barrel		end-cap	
	Number of layers and $\|\eta\|$ coverage			
Presampler	1	$\|\eta\| < 1.52$	1	$1.5 < \|\eta\| < 1.8$
Calorimeter	3	$\|\eta\| < 1.35$	2	$1.375 < \|\eta\| < 1.5$
	2	$1.35 < \|\eta\| < 1.475$	3	$1.5 < \|\eta\| < 2.5$
			2	$2.5 < \|\eta\| < 3.2$
	Granularity $\Delta\eta \times \Delta\phi$ versus $\|\eta\|$			
Presampler	0.025×0.1	$\|\eta\| < 1.52$	0.025×0.1	$1.5 < \|\eta\| < 1.8$
Calorimeter 1st layer	$0.025/8 \times 0.1$	$\|\eta\| < 1.40$	0.050×0.1	$1.375 < \|\eta\| < 1.425$
	0.025×0.025	$1.4 < \|\eta\| < 1.475$	0.025×0.1	$1.425 < \|\eta\| < 1.5$
			$0.025/8 \times 0.1$	$1.5 < \|\eta\| < 1.8$
			$0.025/6 \times 0.1$	$1.8 < \|\eta\| < 2.0$
			$0.025/4 \times 0.1$	$2.0 < \|\eta\| < 2.4$
			0.025×0.1	$2.4 < \|\eta\| < 2.5$
			0.1×0.1	$2.5 < \|\eta\| < 3.2$
Calorimeter 2nd layer	0.025×0.025	$\|\eta\| < 1.40$	0.050×0.025	$1.375 < \|\eta\| < 1.425$
	0.075×0.025	$1.4 < \|\eta\| < 1.475$	0.025×0.025	$1.425 < \|\eta\| < 2.5$
			0.1×0.1	$2.5 < \|\eta\| < 3.2$
Calorimeter 3rd layer	0.050×0.025	$\|\eta\| < 1.35$	0.050×0.025	$1.5 < \|\eta\| < 2.5$
	Number of readout channels			
Presampler	7808		1526 (both sides)	
Calorimeter	101760		62208 (both sides)	

Table 3.1: Details on the electromagnetic calorimeters. According to [32].

Tile	Barrel	Extended barrel
$\lvert\eta\rvert$ coverage	$\lvert\eta\rvert < 1.0$	$0.8 < \lvert\eta\rvert < 1.6$
Number of layers	3	3
Granularity $\Delta\eta \times \Delta\phi$	0.1×0.1	0.1×0.1
	0.2×0.1 (last layer)	0.2×0.1 (last layer)
Readout channels	5760	4092 (both sides)

	LAr hadronic end-cap	LAr forward
$\lvert\eta\rvert$ coverage	$1.5 < \lvert\eta\rvert < 3.2$	$3.1 < \lvert\eta\rvert < 4.9$
Number of layers	4	3
Granularity	$\Delta\eta \times \Delta\phi$	$\Delta x \times \Delta y$(cm)
	0.1×0.1 $1.5 < \lvert\eta\rvert < 2.5$	FCal1 3.0×2.6 $3.15 < \lvert\eta\rvert < 4.30$
	0.2×0.2 $2.5 < \lvert\eta\rvert < 3.2$	FCal1 ~four times finer $3.10 < \lvert\eta\rvert < 3.15$
		$4.30 < \lvert\eta\rvert < 4.83$
		FCal2 3.3×4.2 $3.24 < \lvert\eta\rvert < 4.50$
		FCal2 ~four times finer $3.20 < \lvert\eta\rvert < 3.24$
		$4.50 < \lvert\eta\rvert < 4.81$
		FCal3 5.4×4.7 $3.32 < \lvert\eta\rvert < 4.60$
		FCal3 ~four times finer $3.29 < \lvert\eta\rvert < 3.32$
		$4.60 < \lvert\eta\rvert < 4.75$
Readout channels	5632 (both sides)	3524 (both sides)

Table 3.2: Details on the hadronic tile (upper), endcap and forward (lower) calorimeters. According to [32].

The vertical geometry of these tiles make the light transfer via wavelength shifting fibres to the photomultipliers easier and they have by construction a good longitudinal segmentation. The barrel region also acts as the return flux for the inner detectors solenoid. At larger pseudorapidities and closer to the beam pipe, where there is more radiation, liquid argon technology was also chosen for the hadronic calorimeters because of its intrinsic radiation tolerance. In the endcap region copper acts as absorber in a parallel plate geometry. For the forward calorimeters tungsten alloy absorbers are used together with rod shaped electrodes in a very small liquid argon gap. Table 3.2 shows detailed information on the hadronic calorimeters in terms of coverage, granularity and readout channels.

The required energy resolutions are $\sigma/E = 10\%/\sqrt{\mathrm{E(GeV)}} \oplus 0.7\%$ for the electromagnetic, $\sigma/E = 50\%/\sqrt{\mathrm{E(GeV)}} \oplus 3\%$ for the hadronic barrel and end-cap and $\sigma/E = 100\%/\sqrt{\mathrm{E(GeV)}} \oplus 10\%$ for the forward calorimeter. Early data studies have confirmed that the requirements for jets are met [42] . The ATLAS hadronic calorimeter is a non compensating calorimeter, i.e. the energy loss caused by excitation and fission must be accounted for by calibration. This calibration ensures that the jets are at the right energy scale.

Muon system

The outermost layer of the detector is occupied by the large muon system. This large area gas based detector system consists of two types of chambers. On the one hand there are precision chambers that accurately measure the muon tracks, on the other hand there are chambers whose primary purpose is the fast triggering. The air core toroid provides strong bending power within a light and open structure which minimizes multi-scattering effects and therefore an excellent muon momentum resolution can be achieved [33]. The beam pipe and the shielding are optimized such that neutron-induced background in the muon system is reduced to a minimum.

For most of the area monitored drift tubes are used as precision chambers. Their sense wires being mechanically isolated from each other makes them very robust and reliable. The aluminium made drift tubes are filled with a mixture of Argon and CO_2 and are staged into multilayers which themselves establish a chamber together with sensors monitoring the temperature, magnetic field strength, position and deformation of the chamber. Close to the interaction point cathode strip chambers with a high granularity strip readout are used as precision chambers because of the increased radiation.

In the barrel region resistive plate chambers act as trigger while in the end-cap regions thin gap chambers are used for that purpose. They not only act as a very fast muon trigger but also deliver a second independent measurement of the muon track.

For a combined muon momentum measurement both the track in the muon system and the matched inner detector track are combined together.

Trigger system

At the design luminosity there will be roughly one billion events per second delivered by the LHC. But storage and processing capabilities allow only up to 200-400 events per second to be permanently stored. Therefore, a sophisticated trigger systems needs to be established in order to sensibly reduce the event rate.

The ATLAS trigger system consists of three distinct levels: L1, L2 and the so-called EventFilter (EF). Each of these levels refines the selection made by the previous one and if necessary applies additional criteria. Figure 3.6 shows a diagram of the full ATLAS trigger and data acquisition chain.

The L1 trigger is based on custom-built processors and uses very limited amount of the full detector info (primitive objects in the calorimeters and/or muon system). As a consequence it is - with a decision rate of 2.5 μs per event - very fast. After the L1 trigger the event rate is reduced to $\sim$100 kHz.

The L2 and EF are both based on algorithms run offline on commercial computer farms. The L2 trigger further reduces the rate to $\sim$3.5 kHz in about 40 ms per event. The EventFilter marks the final trigger selection using more elaborate algorithms than L2 and reduces the event rate to its final value of $\sim$200 Hz. Due to the more complex decisions it takes about 4 seconds per event. The desired final rate is achieved using parallelization.

3.3 The ATLAS analysis chain

This section briefly introduces how the ATLAS data and the Monte Carlo simulations reconstructed with the `GEANT4` [43] based detector simulation are organized in the various formats. After the reconstruction algorithms were run on ATLAS raw data or the output from any MC generator, the events are stored in so-called 'Event Summary Data' (ESD) files. These contain very detailed information on the event, such as calorimeter cells and tracking system hits. Consequently, they consume a lot of resources in terms of storage. Therefore, they are

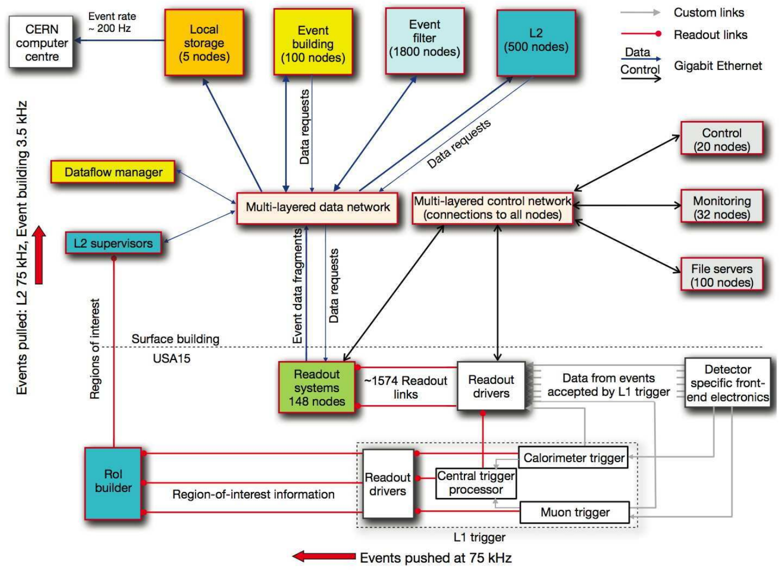

Figure 3.6: Block diagram of the ATLAS trigger and data acquisition systems. Taken from [32].

only used for dedicated detector and reconstructions and not for physics analysis [3]. In order to do that, smaller 'Analysis Object Data' (AOD) files are derived from ESDs, which lack e.g. the detailed information on calorimeter cells and tracking hits. Although it is possible to do analysis directly on AODs (and this was done in Chapter 5), it is still difficult due to the still large size per event. A solution is provided by so-called 'derived AODs' (DAODs or DPDs) and especially the so-called 'D3PDs', which are a flat ROOT [44] ntuple dump of selected AOD contents. The D3PDs contain different information for different kind of analysis and are limited in size, such that it is possible to store all Monte Carlo samples and data (as of April 2011) on a single institutes storage element.

[3] There are special 'derived ESDs' (DESDs) that reduce the size by certain filters for a specific use case.

Chapter 4

Proposal for using the monojet analysis to spot detector problems

4.1 Motivation and concept

As described earlier, in the search for new physics such as Supersymmetry many models lead to signatures with missing transverse energy and jets. Therefore, it is crucial to understand all sources of fake missing transverse energy. There are various effects that may lead to a mismeasurement of $E_{\mathrm{T}}^{\mathrm{miss}}$, such as hot or dead areas in the calorimeter or an imperfect description of the calorimeter response to jets. These problems were artificially introduced to the Monte Carlo and their impact on typical observables was investigated in events with one leading jet and missing transverse energy, because this monojet signature is very sensitive to those problems.

If one assumes no physics beyond the Standard Model and a perfect detector, events with no isolated lepton, only one hard jet and missing transverse energy are due to $Z \to \nu\nu$ + jet events only. Here the jet and $E_{\mathrm{T}}^{\mathrm{miss}}$ should be roughly back to back, balancing each other.

If the contribution of detector effects to $E_{\mathrm{T}}^{\mathrm{miss}}$ is significant, this will show up, for example, at a specific azimuthal angle Φ where QCD dijet events start to pass the event selection criteria. As the QCD cross section is several orders of magnitude larger than the ones for other contributing processes, there will be peaks in the distributions pointing to the problematic region. If there are more general problems like a wrong jet energy scale or an overall worse $E_{\mathrm{T}}^{\mathrm{miss}}$ resolution, the leading jet will be less balanced by the missing transverse energy. Therefore, the difference of the azimuthal angle $\Delta\Phi$ between the jet and $E_{\mathrm{T}}^{\mathrm{miss}}$ will reflect these kind of problems.

This chapter summarizes very early qualitative studies on the basis of a simplified 4-vector approach. The study was published as a reviewed ATLAS Internal note [45].

4.2 Monte Carlo samples and event selection

All Monte Carlo samples used in this study were simulated with Athena release 12. The old Athena release is due to the early stage during which this study was performed. It should be pointed out that no actual ATLAS data was available at that point and that the quality of the data we see today was neither known nor expected.

The events were generated using either `Pythia` or `Alpgen` and `JIMMY`. Only Monte Carlo samples from the official ATLAS production with the full detector simulation were used. The AODs [46, 47] were analyzed via EventView [48]. The same object definitions and overlap removal algorithms were used as described in detail in [49]. In the following the applied object criteria are summarized.

Jets:
A cone algorithm [49] with a cone size of 0.4 was used to reconstruct jets. The jet container which was used is the so-called "Cone4H1TowerJets" container.

Missing transverse energy:
The original missing transverse energy is calculated from calorimeter cells. Calibration weights were derived separately for cells associated to different objects. Here the used container is "MET_RefFinal", which includes corrections accounting for dead material and the recalculated muon term.

Electrons:
The "eGamma" algorithm [50] was used to identify and reconstruct electrons using "medium" purity cuts. Events with an electron inside the calorimeter crack regions ($1.37 < |\eta| < 1.52$) were rejected. The transverse energy inside a cone of $\Delta R < 0.2$ around the electron was required to be smaller than 10 GeV for the electron to be regarded as isolated. If a jet is overlapping with an electron within ΔR of 0.2 the jet was removed from the jet list while the electron was rejected if it is found in a distance $0.2 < \Delta R < 0.4$ of a jet.

Muons:
For muon reconstruction the "STACO" algorithm [51] was used, which combines Muon System and Inner Detector tracks. The total energy inside a cone of $\Delta R < 0.2$ around the muon was required to be less than 10 GeV. Muons which are close to a jet within $\Delta R < 0.4$ were removed.

In addition the following event selection criteria were applied: events with isolated leptons are vetoed and exactly one jet with a $p_{\mathrm{T}} > 150$ GeV with $|\eta| \leq 2.5$ is required. Any number of jets with a $p_{\mathrm{T}} < 50$ GeV are allowed and a missing transverse energy of $E_{\mathrm{T}}^{\mathrm{miss}} > 150$ GeV is required. The events are requested to pass the L1-1Jet Trigger (*L1_J120* [1]). Hence one does not rely on the $E_{\mathrm{T}}^{\mathrm{miss}}$ trigger only. The cuts are chosen to give a good signal ($Z \to \nu\nu$) to background ratio and high statistics in the signal sample.

Table 4.1 shows the event numbers normalized to 10 pb^{-1} for the used Monte Carlo samples. The event weight w is calculated according to $w = (\sigma\mathcal{L})/N$, where σ is the cross section of the process, N the number of generated events in the sample and $\mathcal{L}$ the integrated luminosity (10 pb^{-1} in this case). At first glance one seems to be dominated by QCD dijet events (J1). But the 34950 events for 10 pb^{-1} correspond to just one unweighted event.

[1] At that time *L1_J120* was expected to be the first unprescaled single jet trigger.

Monte Carlo	sample	$\hat{p}_T$ range [GeV]	before cuts	after cuts	weight
PYTHIA	5010 J1	17-35	1.38e+10	34950	34950
PYTHIA	5011 J2	35-70	9.28e+8	0	3447
PYTHIA	5012 J3	70-140	5.73e+7	0	246.6
PYTHIA	5013 J4	140-280	3.01e+6	0	26.8
PYTHIA	5014 J5	280-560	1.25e+5	0.88	0.44
PYTHIA	5015 J6	560-1120	3.59e+3	0.11	0.014
PYTHIA	5016 J7	1120-2240	57	0	3.8e-4
PYTHIA	5183 Znunu		7.13e+3	197	0.14
MC@NLO	5200 top lepton		4.41e+3	5.58	0.01
MC@NLO	5204 top hadron		3.80e+3	0	0.05
PYTHIA	5104 Wenu		1.05e+5	5.6	0.62
PYTHIA	5105 Wmunu		1.19e+5	31.7	0.29
PYTHIA	5106 Wtaunu		3.37e+4	15.6	0.21
PYTHIA	5107 Wtauhad		5.52e+4	30.6	6.1

Table 4.1: Number of events normalized to 10 pb^{-1} before and after all cuts (for J1 34950 normalized events correspond to one unweighted event)

Nevertheless this is disturbing since by the definition of the J1 sample it should not contain any events that pass the selection cuts (c.f. the $\hat{p}_T$ values for the QCD samples in Table 4.1). So this event was investigated in detail in Appendix B . It turned out that this event suffers from a known bug in `GEANT4` (for the Athena release 12 that was used in this study). A high p_T particle generated by `GEANT4` introduces an imbalance of the event. As a result the affected event is dominated by the high p_T `GEANT4` particle and missing transverse energy. Although this bug was known in general the occurrence in the J1 sample has not been observed until that point.

Because of the strong hints that this is really a reconstruction problem in the J1 sample it is justified to discard this special J1 event in the following. This was done by omitting the J1 sample as a whole. Then the main contribution after all cuts comes from $Z \to \nu\nu$ + jets, as expected.

The capabilities of finding detector problems with the monojet analysis are systematically investigated in the following.

4.3 Methods and control distributions

These studies represent a first look on the performance of a monojet analysis using a simplified 4-vector based inclusion of systematic effects. This simplified approach was chosen, because it is very hard if not even impossible to include all and not foreseen systematic effects into a full simulation of the events. Different methods to simulate detector problems were developed and are explained in this chapter.

For simulating dead areas in the calorimeter the jet energy was simply reduced in a certain

η-Φ region and $E_{\mathrm{T}}^{\mathrm{miss}}$ was recalculated, while for simulating hot areas the energy of a jet was increased (and the $E_{\mathrm{T}}^{\mathrm{miss}}$ was recalculated as well). For simulating more general detector problems the jet energy was changed in various manners. For one, the energy of the low p_{T} jets in the event is smeared. Furthermore the jet energy scale is changed by applying a constant shift and by introducing extra tails in the jet's energy resolution.

In order to be able to judge the influence of the simulated problems, one first has to look at the control distributions of the original detector response. These were obtained by using the events which pass the selection cuts (Figure 4.1, Figure 4.2 and Figure 4.3).

To distinguish detector problems from Monte Carlo issues, almost all control distributions can be obtained from data. Since $Z \to \nu\nu$ + jets is by far the dominant process after the selection cuts, control distributions can be obtained from $Z \to ll$ + jets events. This will allow to judge the distributions independent from any Monte Carlo expectation [49]. The azimuthal angle between the leading jet and the missing transverse energy $\Delta\Phi$ marks an exception for certain cases where one has to rely on Monte Carlo prediction. If this is the case, it will be explicitly stated in the text.

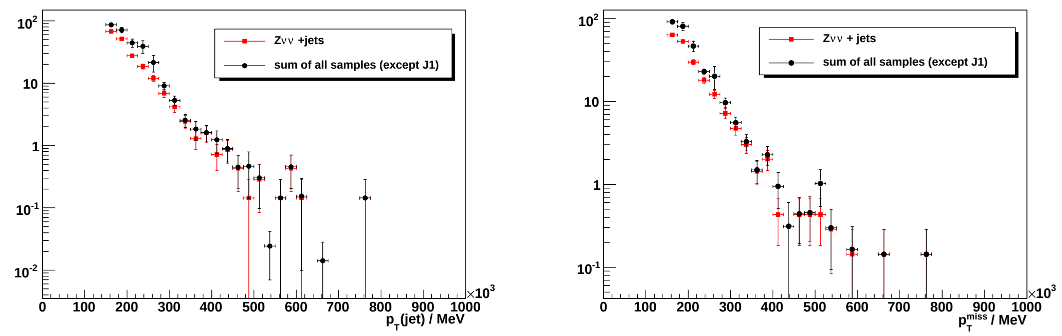

Figure 4.1: Transverse momentum of the leading jet (left) and missing transverse momentum (right)

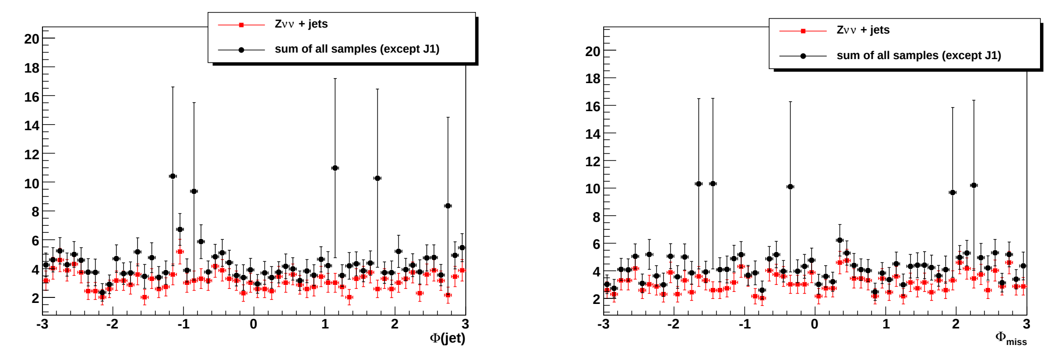

Figure 4.2: Azimuthal angle Φ of the leading jet (left) and the missing transverse momentum (right). The entries with big statistical errors are mainly due to events from the 5107 Wtauhad sample which comes with a weight of 6.1.

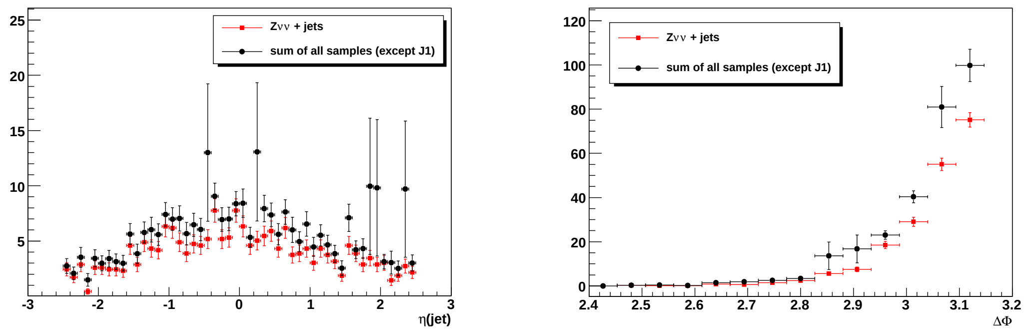

Figure 4.3: Pseudorapidity η of the leading jet (left; the entries with big statistical errors are mainly due to events from the 5107 Wtauhad sample which comes with a weight of 6.1) and azimuthal angle $\Delta\Phi$ between the jet and missing transverse momentum

4.4 Results

Dead areas

A partly dead area is introduced by reducing the energy of the leading jet, if it points to the region $\eta = [-0.1; 0.1]$, $\Phi = [0.8; 0.9]$, and E_T^{miss} has been recalculated. The jet energy was reduced to 50%, 30% and 20% of its original value. Figure 4.4 shows the azimuthal angle Φ of the leading jet and the missing transverse energy. The reduction of the jet energy leads to additional missing transverse energy in the event, which is then pointing in the same direction as the jet. With this modification QCD dijet events start to pass the selection criteria, leading to an enhanced signal in E_T^{miss} at $\Phi = [0.8; 0.9]$. The leading jet is then biased to be back to back to the missing transverse energy.

Hot areas

A partly hot area is introduced by increasing the energy of the leading jet, if it points to the region $\eta = [-0.1; 0.1]$, $\Phi = [0.8; 0.9]$, and E_T^{miss} has been recalculate. The mechanism of simulating this problem is analog to the one used for simulating Dead Areas. The missing transverse energy is now biased in the opposite direction of the leading jet (Figure 4.5 and 4.6). When increasing the jet energy in the above mentioned area, QCD dijet events start to contribute to the selected events and a peak starts to develop in the Φ distribution at $\Phi = [0.8; 0.9]$ for jets and at $\Phi = [0.8; 0.9] - \pi$ for the missing energy. Furthermore, there is also an excess in the η distribution of the leading jet (Figure 4.7) at η around zero.

Varying the jet energy scale

The overall jet energy scale was varied by a constant factor. The effect of this may be seen in the angle between the jet and the missing transverse energy (Figure 4.8). Lower energy scales result in a broad $\Delta\Phi$ distribution, that is less prominently peaked at π. Here one can also observe the influence of the jet energy scale on the number of events passing the cuts. In this case one has to rely on the Monte Carlo predictions to get a reference for the $\Delta\Phi$ distribution.

Influence of tails in the jet energy resolution

The last thing which was checked is the influence of the tails in the jet energy resolution. To accomplish this, the energy of a certain fraction A of the leading jets was changed. For one half of A the new energy $E'$was set to $E' = (1-B) \cdot E$ and for the other half to $E' = (1+B) \cdot E$, where B is the applied energy change. The result of this smearing can be seen in the ΔE(jets) (energy of the reconstructed jet - energy of the matched true jet) distribution for different values of A and B (Figure 4.9).

As a result of this modification a peak in the $\Delta\Phi$ distribution at zero started to develop with increasing tails (Figure 4.10). In contrary to the results of the changed jet energy scale, there is no broadening in the region close to $\Delta\Phi = \pi$. An effect is visible even when in only 5% of the events the jet energy is on average wrongly measured by 30%. Also here one has to rely on the Monte Carlo predictions to get a reference distribution.

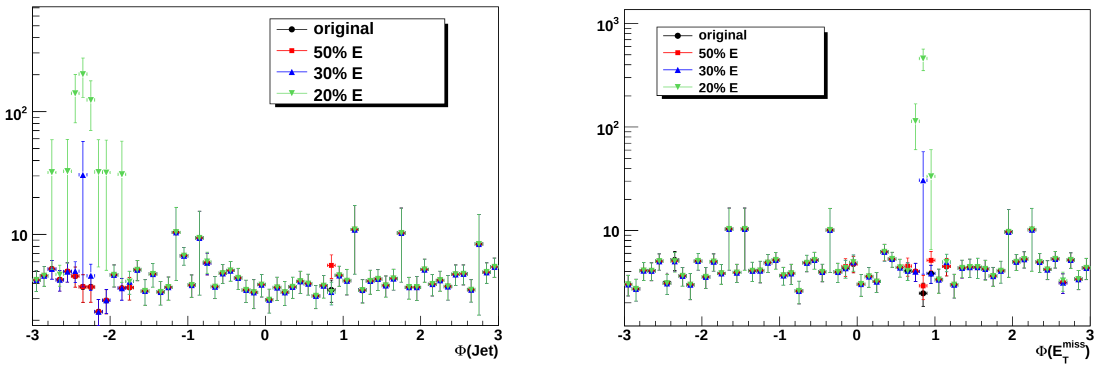

Figure 4.4: Φ of the leading jet and the missing transverse energy when reducing the jet energy in the region $\eta = [-0.1; 0.1]$, $\Phi = [0.8; 0.9]$. The jet energy was reduced to 50%, 30% and 20% of its original value.

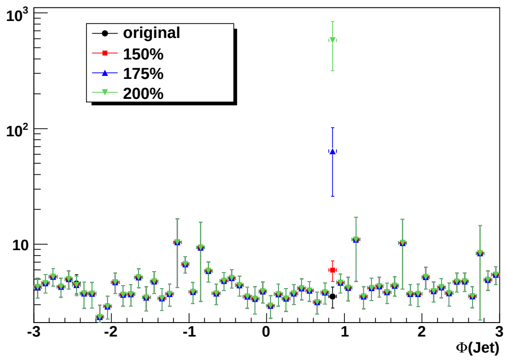

Figure 4.5: Φ of the leading jet when increasing the energy of the leading jet in the region $\eta = [-0.1; 0.1]$, $\Phi = [0.8; 0.9]$. The jet energy was increased to 150%, 175% and 200% of its original value.

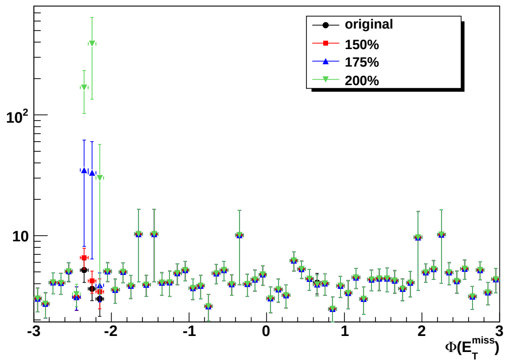

Figure 4.6: Φ of the missing transverse energy when increasing the energy of the leading jet in the region $\eta = [-0.1; 0.1]$, $\Phi = [0.8; 0.9]$. The jet energy was increased to 150%, 175% and 200% of its original value.

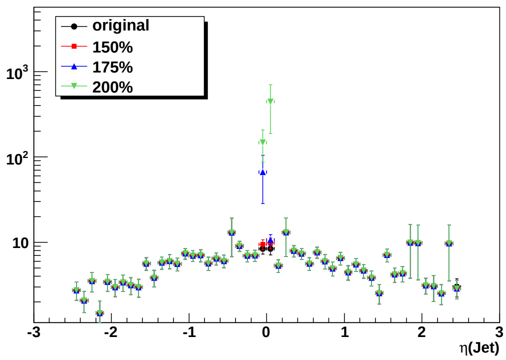

Figure 4.7: η of the leading jet when increasing the energy of the leading jet in the region $\eta = [-0.1; 0.1]$, $\Phi = [0.8; 0.9]$. The jet energy was increased to 150%, 175% and 200% of its original value.

4.5 Discussion

This study has shown that a monojet analysis is sensitive to various detector problems and might be useful to find such effects especially at very high p_{T} and $E_{\mathrm{T}}^{\mathrm{miss}}$ with early data. It also shows that it might be possible to not only localize but also to distinguish specific problems (Table 4.2). For the hot area there are additional peaks in the $\Phi(\text{jet})$ and $\eta(\text{jet})$ distributions. Whereas for a dead area the $\eta(\text{jet})$ peak is missing. If the jet energy scale is changed, this results in a broadening of $\Delta\Phi(\text{jet}, E_{\mathrm{T}}^{\mathrm{miss}})$ and if there are additional tails in the jet energy resolution, an additional peak at zero starts to form in the $\Delta\Phi(\text{jet}, E_{\mathrm{T}}^{\mathrm{miss}})$ distribution.

During the review process of the ATLAS Internal note [45] it was argued that the detector problems, which were simulated, would be spotted much earlier in the analysis chain with low

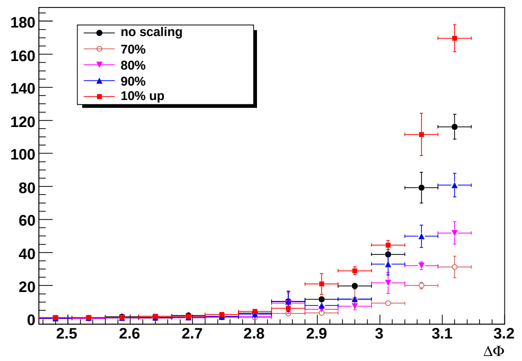

Figure 4.8: $\Delta\Phi$ between the leading jet and $E_{\mathrm{T}}^{\mathrm{miss}}$ for different jet energy scales. The plot shows the $\Delta\Phi$ for the original jet energy scale and for 70%, 80%, 90% and 110% of its original value.

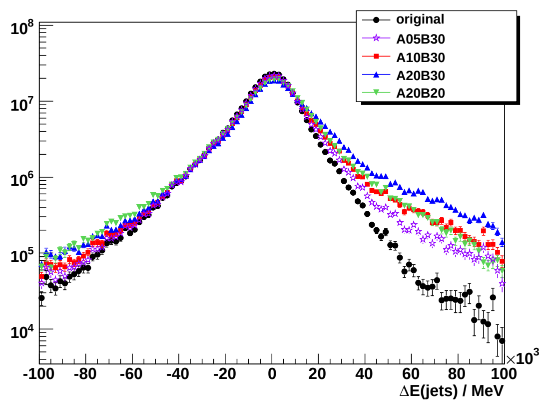

Figure 4.9: Differences in energy between the reconstructed and true jet for different values of the parameters A and B (in percent). A denotes the fraction of jets for which the energy was altered and B is the amount of energy change we apply.

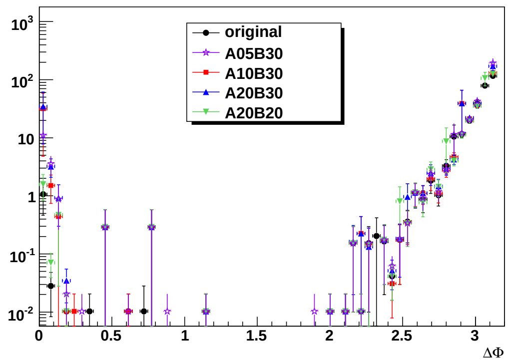

Figure 4.10: $\Delta\Phi$ between the leading jet and $E_{\mathrm{T}}^{\mathrm{miss}}$ for different values of the parameters A and B (in percent). A denotes the fraction of jets for which the energy was altered and B is the amount of energy change we apply.

detector effect	visible monojet feature
hot area	peak in $\Phi(E_{\mathrm{T}}^{\mathrm{miss}})$, $\Phi(\mathrm{jet})$ and $\eta(\mathrm{jet})$
dead area	peak in $\Phi(E_{\mathrm{T}}^{\mathrm{miss}})$, $\Phi(\mathrm{jet})$, no $\eta(\mathrm{jet})$ peak
change in jet energy scale	broadening of $\Delta\Phi(\mathrm{jet}, E_{\mathrm{T}}^{\mathrm{miss}})$
tails in jet energy	peak at zero in $\Delta\Phi(\mathrm{jet}, E_{\mathrm{T}}^{\mathrm{miss}})$

Table 4.2: Summary of simulated detector effects and their visible features

level detector studies. This statement is affirmed by the quality of the first ATLAS data (as for 2010). Nevertheless, this study has shown that, if there were still problems concerning data quality left, a monojet analysis, such as this, is a valuable tool to spot them. It also shows that one has to be aware of the fact that a monojet analysis used in searches for new physics might pick up various kinds of non-collision backgrounds. This means that all distributions presented for this study should be checked when searching for new physics with a monojet analysis. These effects might not only be caused by detector problems but also by non-collision background like beam-gas or beam halo events. These kinds of backgrounds are investigated in the following chapter.

Chapter 5

Studying suppression of beam-induced and cosmic background to physics analyses

As mentioned in the previous chapter, it is vital to suppress non-physics background. This chapter describes an early study on the suppression of fake jets arising from beam-induced background and cosmic rays by using jet quality cuts. Beam halo, beam-gas or cosmic ray jets have particular features that are distinguishable from QCD jets. Monte Carlo samples modeling QCD dijet, beam-gas, beam halo and cosmic events, as well as cosmic and single-beam data from Fall 2008, are used for this study.

Several jet variables are tested for their discriminating power. The results are compared to existing studies and the selection is further optimized using multivariate techniques. The use of event cleaning cuts is also discussed and proves very useful, especially for suppressing background from beam halo events. This study was supervised by Bernhard Meirose and was published as a reviewed ATLAS Internal Note [52].

5.1 Introduction

Cosmic rays and machine-induced backgrounds (like beam-gas or beam halo events) can, though their rates are small, be sources of fake jets for all energy regions. Since these events might overlap with events emerging from collisions, it is crucial to understand how fake and real jets can be distinguished. The QCD cross section would otherwise be incorrectly measured (especially in the case of the more probable low-energy fake jets), and physics analyses, including either jets or missing transverse energy, would be spoiled by the fake jets' contribution.

In the following it will be shown that this separation can be achieved with a set of jet cleanup cuts which were developed considering the characteristics of the jets coming from the different sources. First, a list of the different Monte Carlo and data samples used in this study is given, with detailed descriptions. Then the different jet characteristics are considered for jets coming from QCD, cosmic rays, beam-gas and beam halo events. After that the cleanup cuts are described. For cut optimization multivariate techniques are used, which are verified by comparing the results to an existing cosmic ray background study. In addition, event cleaning cuts are studied, especially for the case of beam halo background. The rates which can be expected for the different backgrounds are estimated and the impact of this study on physics analyses is discussed.

5.2 Data analysis methods

The study was performed as an AOD-based analysis [46, 47]. From the AODs, ROOT [44] ntuples and trees were derived using Athena Root Access (ARA)[53]. For the event displays, xml files were produced from the ESDs [47] using standard ATLAS jobOption files. So-called "TAG_COMM" files, derived from RDOs [54], were used to calculate event variables.

5.3 Monte Carlo and data samples

For this study, Monte Carlo samples from the official ATLAS production were used (from mc08 production with a center-of-mass energy of 14 TeV), as well as single-beam and cosmic ray data recorded in the Fall of 2008. The Monte Carlo samples were reconstructed using the full `GEANT4` [43] detector simulation. For beam-gas and beam halo, the MC samples represent the - at that time still expected - 7 TeV beam energy. The different samples are described in detail in the following section. When discussing Monte Carlo, a short description of the used event generator is included.

5.3.1 QCD dijet Monte Carlo

For QCD dijets the `Pythia` event generator [22] was used. Table 5.1 summarizes the available official samples. As already mentioned in Chapter 4, there are different samples for different

Sample Name	$\hat{p}_{\mathrm{T}}$ range [GeV]
mc08.105010.J1_pythia_jetjet	17-35
mc08.105011.J2_pythia_jetjet	35-70
mc08.105012.J3_pythia_jetjet	70-140
mc08.105013.J4_pythia_jetjet	140-280
mc08.105014.J5_pythia_jetjet	280-560
mc08.105015.J6_pythia_jetjet	560-1120
mc08.105016.J7_pythia_jetjet	1120-2240
mc08.105017.J8_pythia_jetjet	> 2240

Table 5.1: Summary of `Pythia` QCD dijet samples

values of $\hat{p}_{\mathrm{T}}$ of the partons from the hard process. These dijet samples are regarded as signal in this study. The goal is to achieve the highest efficiency for these samples, while suppressing most of the non-collision background. In the following sections the various background sources are described.

5.3.2 Beam-gas Monte Carlo

Beam-gas events are best modeled by a generator designed for nuclear physics, since the basic interaction is the impact of a relativistic proton on a quasi-stationary atomic nucleus. For this reason, the `HIJING` generator (Heavy Ion Jet INteraction Generator) [55, 56] was used, which is integrated into the ATLAS software framework Athena. Interactions with common vacuum impurities like H, C or O were generated, as well as interactions with other possible trace contaminants like Be, Cu, Cr, Fe, N, Ti, V, W and Zr. These contaminants are very unlikely, but are nevertheless present inside the vacuum system. The number of events generated corresponds roughly to the estimated rate of vacuum contamination, as estimated by A. Rossi [57], for the three principal gases. Other possible contaminants are not considered likely, and are not added in proportion. The simulation distributes the beam-gas interaction points evenly throughout the ATLAS beam pipe. For this study, the *mc08.108863.Hijing_beamgas.recon.AOD.e4_s470_r635_t53* sample was used.

Figure 5.1 shows the transverse energy spectrum (calculated from all the clusters in the event) for the beam-gas Monte Carlo sample, as well as the jet transverse energy spectrum for jets with $E_{\mathrm{T}} > 5$ GeV, and the missing transverse energy spectrum. Figure 5.2 shows an example of a Monte Carlo beam-gas event containing a 100 GeV jet in the Atlantis [58] event display.

The transverse energy spectrum (Figure 5.1) corresponds to what one would expect from a fixed-target-based calculation. The cutoff in this spectrum should be approximately [59]

$$E_{\mathrm{T}}^{\mathrm{cutoff}} \approx 50\% \cdot \sqrt{2 \cdot E_{\mathrm{beam}} + m_{\mathrm{target}}} \tag{5.1}$$

The factor of 50% in equation 5.1 is a rough estimate for the ratio of E_{T}/E. If one uses the values for the beam energy of 7 TeV and the mass for nitrogen of 14 GeV, it results in a cutoff value of 200 GeV, which is close to the 150 GeV one can see in Figure 5.1.

5.3.3 Beam halo Monte Carlo

"Beam halo events" is a general term for events arising from three different sources: particle losses in the accelerator, beam-gas interactions in the accelerator, or collimator interactions with the beam. The beam halo simulation covers only the last kind of events, and was done using the `FLUKA` generator [60]. `FLUKA` can accurately simulate the interaction and propagation of various particles in matter. Each event corresponds to one proton that is lost at the tertiary collimators. The decay products of the inelastic proton collision are projected along the beam line to a scoring plane, which is 23 m away from the nominal interaction point. Only particles that reach the scoring plane are included in the event output file. A more detailed description of the simulation can be found in [56]. For this study the following dataset was used: *mc08.108852.BeamHaloInputs.recon.AOD.e4 _e348_s563_r708.*

Figure 5.3 shows the transverse energy and the missing transverse energy spectra for this beam halo Monte Carlo sample. The transverse energy spectrum tends to be much softer than the one seen in the beam-gas sample (Figure 5.1). Due to low statistics, it is not possible to show a jet transverse energy spectrum. There are only 12 jets out of the 173492 events in the sample.

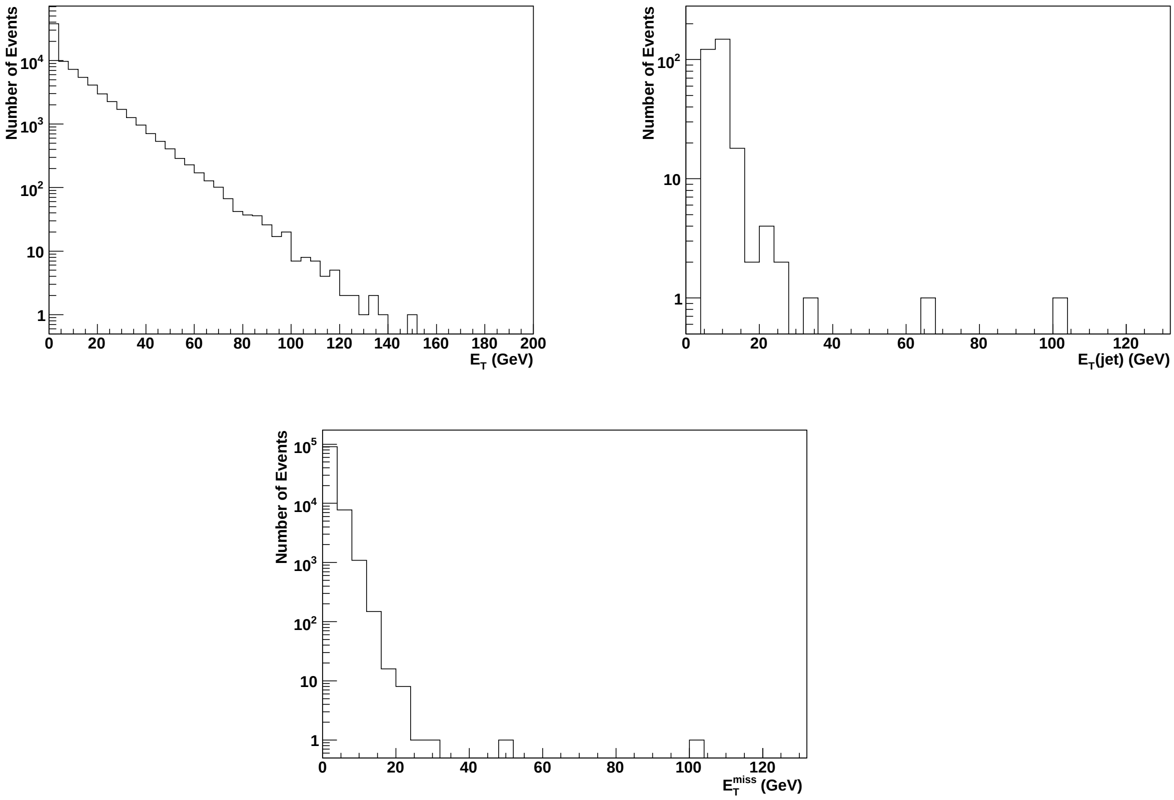

Figure 5.1: E_{T} spectrum of all objects (upper left) and of the jets with $E_{\mathrm{T}} > 5$ GeV (upper right) as well as the missing transverse energy spectrum (lower plot) for beam-gas Monte Carlo (99779 events).

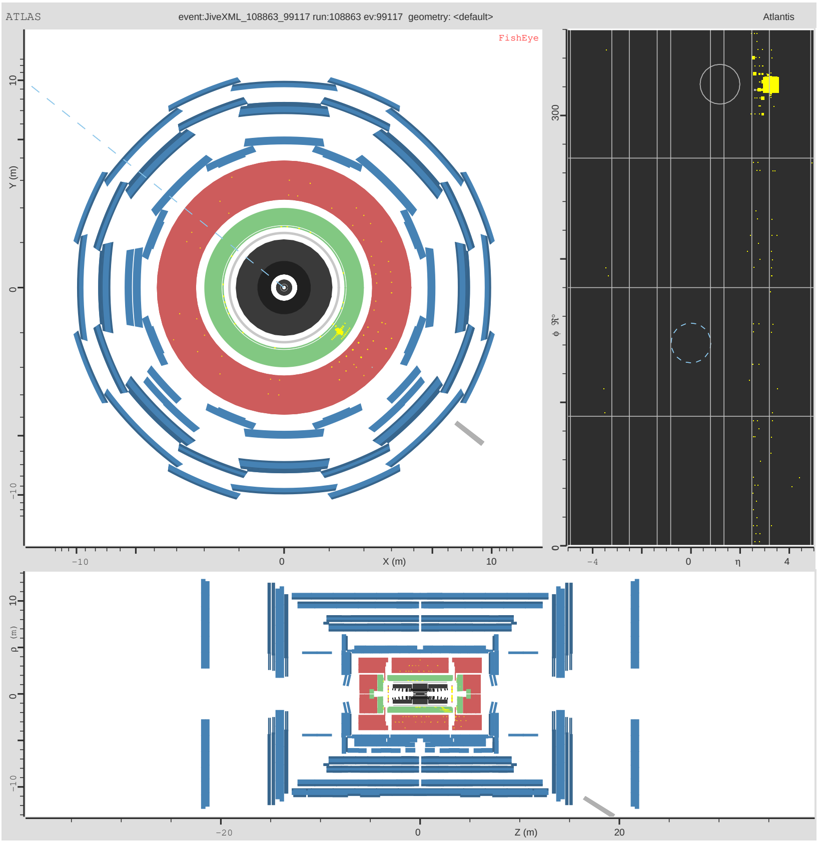

Figure 5.2: Atlantis event display for a Monte Carlo beam-gas event containing a 100 GeV jet. No tracking information was included in the event display.

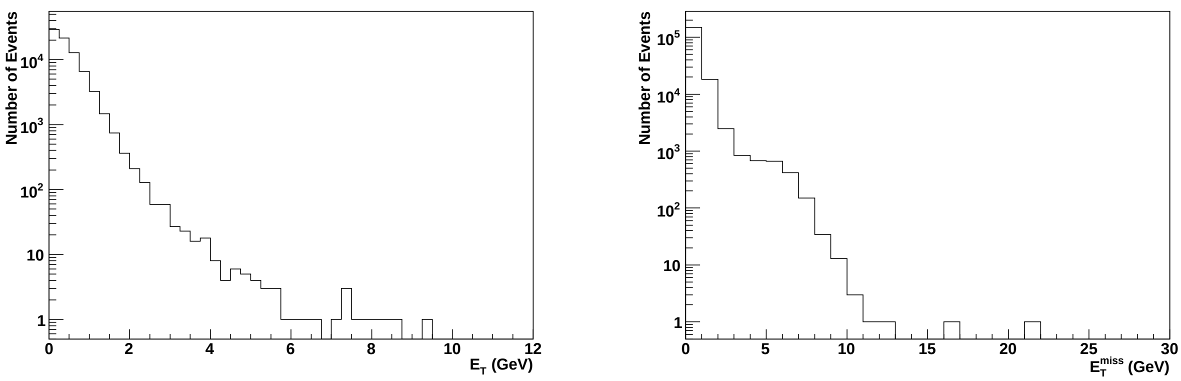

Figure 5.3: E_{T} spectrum of all objects (left) and the missing transverse energy spectrum (right) for the beam halo Monte Carlo (173492 events).

5.3.4 Single-beam data

The single-beam data collected in Fall 2008 provided, at the time this study was carried out, a good opportunity for a first look at the backgrounds that were expected during the collision data taking, although the beam energy was only 450 GeV. Several single-beam runs were recorded, but only a few proved useful for this study, as they have to be clean, (no "splash" events[1]) and (ideally) have all detector subsystems active. Even runs that seem clean at first glance may suffer from so-called "beam scraping" events. These are events for which the radio frequency capture (RF-capture) was OFF and the beam is naturally defocussed.

Figure 5.4 shows the spectra of the transverse energy and missing transverse energy for the clean run 88128, in which the collimators were open and RF-capture was ON (*data08_1beam mag.00088128.physics_BPTX.merge.AOD.o4_r653_p26*). Therefore, almost all events must arise from real non-collision background with some noise contamination. There is also the possibility of cosmic ray contamination, but as this run had a very good beam triggering, the rate should be very low.

The cutoff value which one would expect for beam-gas events only, computed according to Equation 5.1, for the transverse energy spectrum, is approximately 15 GeV. This fits very well with what one observes in Figure 5.4.

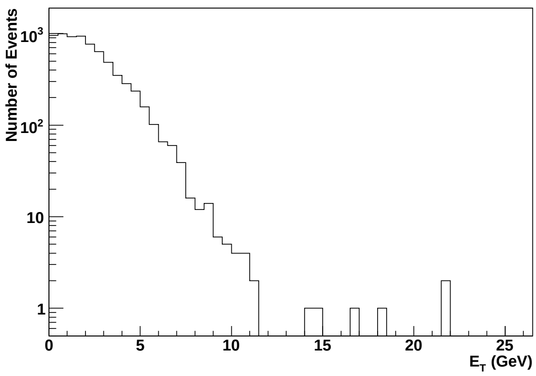

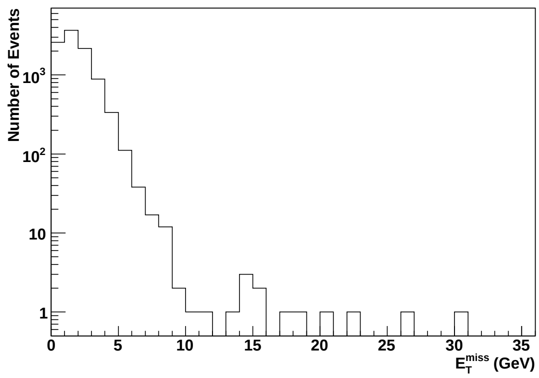

Figure 5.4: E_{T} spectrum (left) and $E_{\mathrm{T}}^{\mathrm{miss}}$ spectrum (right) for single-beam data (450 GeV single-beam, run 88128). The events originate mostly from beam halo and beam-gas interactions with some electronic noise contamination in the low E_{T} region.

Figure 5.5 shows the jet transverse energy spectrum of the single-beam run 88069. In this run, there was no LAr calorimeter information available. That is why the jets were reconstructed using only the information from the hadronic tile calorimeter. Nevertheless, this was the only opportunity to get a first estimate of the jet energy in data, since this was the only clean single-beam run with enough jet statistics. In this run, there are 31 jets out of 155104 events.

[1] As the LHC was being tuned up on 10 September 2008, the beam was initially directed at beam collimators just outside the detector, so that a splash of particles would fill much of the detector allowing ATLAS experimenters to prepare the detector for actual running.

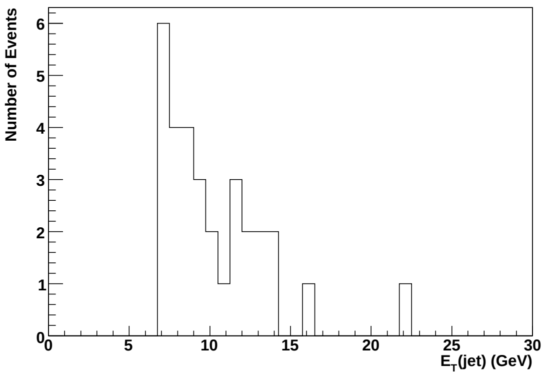

Figure 5.5: E_{T} spectrum of the jets for single-beam data (450 GeV single-beam, run 88069). There was no LAr calorimeter information available in this run.

Figure 5.6 shows a beam halo event with two jets in the Atlantis event display from the single-beam run 88069 (no LAr calorimeter information available) and Figure 5.7 shows the same event in the Calo Cosmic View tool [61]. With this tool it is possible to actually see that the energy deposition inside the calorimeter is coming from particles that fly parallel to the beam pipe, which is consistent with the beam halo interpretation for this event. To obtain the muon traces inside the calorimeters, Calo Cosmic View uses Hough Transform [62], which is a well-known technique for image processing used for detecting straight lines in noisy and lossy environments. Also, the pulse shapes shown in Figure 5.6 indicate that this is indeed a beam effect, and not due to exceptionally high noise.

5.3.5 Cosmic ray data

A very useful set of data collected with the ATLAS detector until then were the various cosmic data samples. Their statistics are much larger, and one can choose from a variety of available samples. To be able to compare the results to an existing study, the sample *data08_cosmag.0090272.physics.L1.Calo* was chosen. Figure 5.8 shows the transverse energy spectrum of the jets in that sample. The spectrum has a very large tail, reaching into the several TeV region.

5.4 Jet and event characteristics

Fake jets originating from the various sources mentioned above have certain characteristics that make them distinguishable from QCD jets. Since jets are calorimeter based objects, the ratios of the energies deposited in the different parts of the calorimeter should give some information about the quality of the jet. The number of charged tracks pointing towards the jet can also be exploited.

The following paragraphs describe the expected characteristics for QCD jets and fake jets coming from cosmic rays, beam-gas and beam halo events. Based on that expected behaviour, the cleaning cuts are developed.

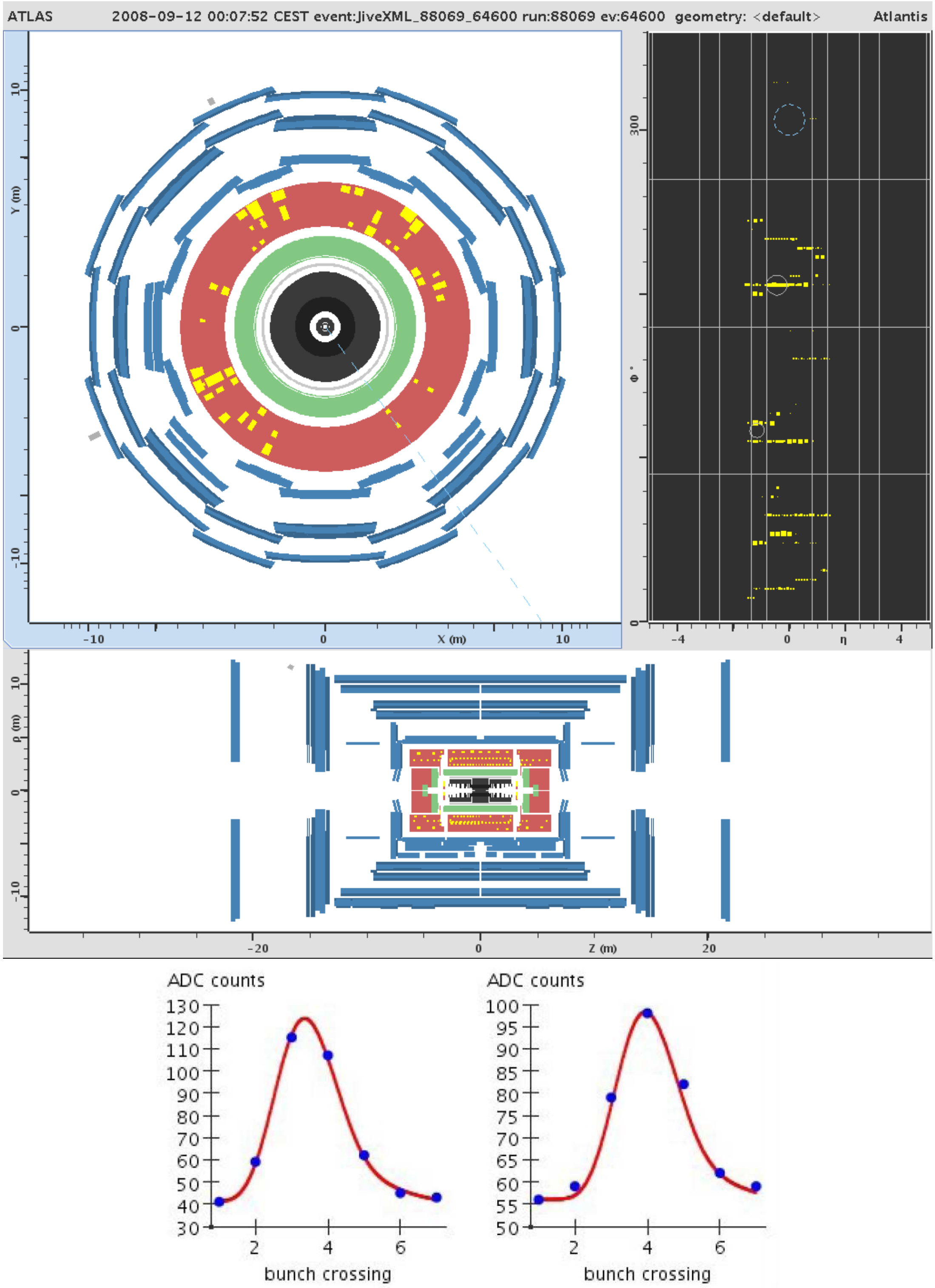

Figure 5.6: Atlantis event display for a beam halo event from the single-beam run 88069 faking two jets. No tracking information was included in the event display and no LAr calorimeter information was available in that run.

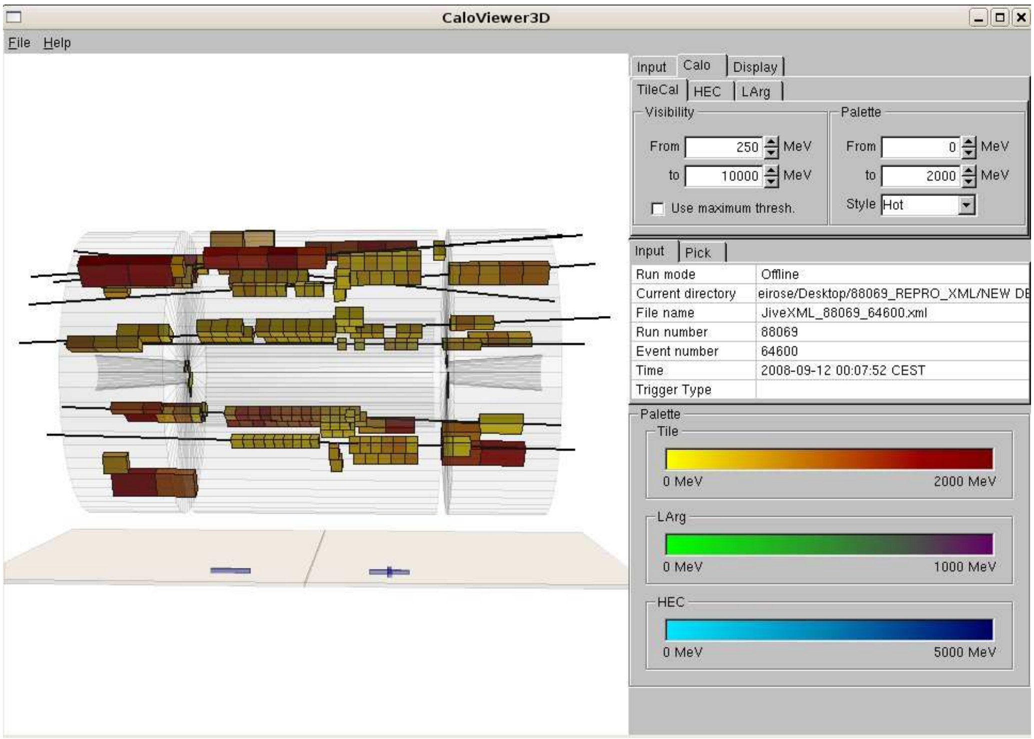

Figure 5.7: Calo Cosmic View of the same beam halo event faking two jets as in Figure 5.6. Note that the energy depositions inside the calorimeter are coming from particles that fly parallel to the beam pipe.

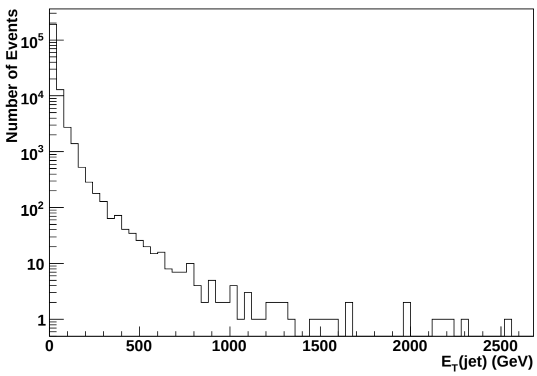

Figure 5.8: $E_{\rm T}$ spectrum of the jet fakes for cosmic ray data (run 90272). Not shown are two jet fakes with $E_{\rm T}$ around 9 TeV.

5.4.1 QCD

"Real" QCD jets will include several charged tracks pointing to the calorimeter jet object. Those tracks can also be associated to a primary vertex close to the interaction point. QCD jets will deposite a significant part of their energy already in the electromagnetic part of the calorimeter.

5.4.2 Cosmic rays

Jets faked by cosmic muons creating hard bremsstrahlung will likely deposit most of their energy either in the electromagnetic or in the hadronic part of the calorimeter. As a consequence, the ratio of the energy deposited in the electromagnetic calorimeter to the total energy will be either around zero or around one. These jets will have only one charged track, if the muon passes near the interaction point. If that is not the case and the muon is non-projective, there will be no track associated to the jet.

5.4.3 Beam-gas

For fake jets coming from beam-gas events, the situation is not as simple. In this case, there is a hard QCD process (the impact of a proton on a stationary nucleon) that leads to one or more spurious fake jets. The only observable differences between QCD and beam-gas jets in the calorimeter is the different geometric behaviour, i.e. the high boost of the fake jets along the beam axis. Furthermore, it is very unlikely that the proton collision with the gas nucleus will happen at the interaction point. The fake jets should therefore in most cases be non-projective, and have no real tracks associated to them (spurious tracks are always possible).

5.4.4 Beam halo

Jet fakes originating from beam halo events share similar geometric characteristics with beam-gas interactions. The jet fakes cannot be traced back to a primary vertex near the interaction point. As a consequence, there are also no tracks associated with the calorimeter object.

5.5 Cleaning cuts

The goal of this study was to develop a set of cuts, which suppress fake jets coming from the abovementioned sources, while keeping as many of the QCD dijets as possible.

In the following section, a set of jet variables is discussed that should have promising discriminating power regarding the jet characteristics mentioned in section 5.4. Then it is shown how the method profits from using multivariate techniques for the cut optimization. For cosmic ray backgrounds, the results are compared to an existing study [63] in order to verify the optimization procedure. Afterwards this technique is applied to all other possible backgrounds.

5.5.1 Jet variables

Based on the jet characteristics described in the previous section and on experiences from earlier publications [56, 49], the following jet variables are considered to give a good discrimination between real QCD and fake jets. [2]

- **electromagnetic fraction**
  Energy deposited in the electromagnetic calorimeter divided by the total jet energy

$$\text{electromagnetic fraction} = \frac{\text{energy deposited in EMB and EMEC}}{\text{energy deposited in all layers}} \qquad (\text{for } |\eta| < 3.2) \tag{5.2}$$

$$\text{electromagnetic fraction} = \frac{\text{energy deposited in EMB, EMEC and FCal1}}{\text{energy deposited in all layers}} \qquad (\text{else}) \tag{5.3}$$

- **fraction tile2**
  Energy in the outermost layer of the Tile Calorimeter divided by the total jet energy

$$\text{fraction tile2} = \frac{\text{energy deposited in Tile2}}{\text{energy deposited in all layers}} \tag{5.4}$$

- **fraction tile10**
  Energy in the two outermost layers of the Tile Calorimeter divided by the total jet energy

$$\text{fraction tile10} = \frac{\text{energy deposited in Tile2 and Tile1}}{\text{energy deposited in all layers}} \tag{5.5}$$

- **number of tracks**
  Number of tracks within a cone of 0.4 of the calorimeter jet

- **charge fraction**
  Sum of the p_{T} of the tracks associated to the jet divided by the jet E_{T}

$$\text{charge fraction} = \frac{\sum p_{\mathrm{T}}^{(i)}(\text{track})}{E_{\mathrm{T}}(\text{jet})} \tag{5.6}$$

5.5.2 Making use of multivariate techniques

Having a set of different variables – which are to some extent correlated – it is quite difficult to find a set of cuts that results in an optimal background rejection for a given signal efficiency. Of course, one could use a brute-force method and try all possible cut combinations. This would require a large amount of computing power and time. On the other hand, using only one or two variables would lead to suboptimal results.

It was therefore decided to use TMVA (Toolkit for Multivariate Data Analysis) [64] for this study. TMVA is a toolkit (fully implemented in ROOT [44]), which allows the user to

[2] EMB: Electromagnetic calorimeter barrel region; EMEC: Electromagnetic calorimeter endcap region; FCal1: Innermost layer of the forward calorimeter; Tile1 and Tile2: Inner layers of the tile calorimeter

Cut	cosmic data	J3
> 0.041	$(19.0 \pm 0.2)\%$	$(99.99 \pm 0.004)\%$
> 0.057	$(13.6 \pm 0.2)\%$	$(99.98 \pm 0.01)\%$
> 0.098	$(8.18 \pm 0.17)\%$	$(99.95 \pm 0.01)\%$
> 0.102	$(8.02 \pm 0.17)\%$	$(99.94 \pm 0.01)\%$
> 0.150	$(7.08 \pm 0.16)\%$	$(99.83 \pm 0.02)\%$
> 0.152	$(7.06 \pm 0.16)\%$	$(99.82 \pm 0.02)\%$
> 0.199	$(6.80 \pm 0.15)\%$	$(99.60 \pm 0.03)\%$
> 0.200	$(6.79 \pm 0.15)\%$	$(99.59 \pm 0.03)\%$
> 0.250	$(6.67 \pm 0.15)\%$	$(99.22 \pm 0.04)\%$
> 0.251	$(6.67 \pm 0.15)\%$	$(99.21 \pm 0.04)\%$
> 0.300	$(6.57 \pm 0.15)\%$	$(98.60 \pm 0.05)\%$
> 0.301	$(6.57 \pm 0.15)\%$	$(98.59 \pm 0.05)\%$

Cut	cosmic data	J6
> 0.039	$(19.8 \pm 0.2)\%$	$(99.99 \pm 0.004)\%$
> 0.056	$(13.82 \pm 0.2)\%$	$(99.98 \pm 0.005)\%$
> 0.099	$(8.22 \pm 0.17)\%$	$(99.93 \pm 0.01)\%$
> 0.103	$(8.05 \pm 0.17)\%$	$(99.92 \pm 0.02)\%$
> 0.150	$(7.17 \pm 0.16)\%$	$(99.82 \pm 0.02)\%$
> 0.155	$(7.13 \pm 0.16)\%$	$(99.81 \pm 0.02)\%$
> 0.198	$(6.91 \pm 0.16)\%$	$(99.64 \pm 0.02)\%$
> 0.201	$(6.90 \pm 0.16)\%$	$(99.63 \pm 0.02)\%$
> 0.249	$(6.80 \pm 0.15)\%$	$(99.27 \pm 0.03)\%$
> 0.250	$(6.80 \pm 0.15)\%$	$(99.26 \pm 0.03)\%$
> 0.2999	$(6.66 \pm 0.15)\%$	$(98.59 \pm 0.04)\%$
> 0.3003	$(6.66 \pm 0.15)\%$	$(98.58 \pm 0.04)\%$

Table 5.2: Breakdown of the ratio of jets remaining after different cut values on the jet electromagnetic fraction obtained with TMVA. Only statistical errors are considered.

make use of various kinds of multivariate classifiers. Given the distributions for signal and background, TMVA optimizes the cuts on the chosen variables, such that one obtains an optimized background rejection for a given signal efficiency. The user can choose between various optimization techniques – among them Fisher Discriminant, Maximum Likelihood, Neural Networks or Boosted Decision Trees. For this study, the simplest approach was used: rectangular cut optimization by a genetic algorithm. By so doing, the results can easily be compared to existing studies and verified by simply applying the obtained cuts, which would be very difficult for all other techniques offered in TMVA. The genetic algorithm is said to give the best results in terms of convergence [64].

5.5.3 Comparison with existing studies and new results for cosmic ray background

In [63], several cleanup cuts for cosmic ray fake jets are discussed. In particular, the focus for Tower Jets (only this type is considered here) is on the jet electromagnetic fraction and the number of tracks inside a jet. There, the authors list different cut values on these two variables, the signal efficiency for J3 and J6, and the corresponding background rejection for the cosmic data sample *data08_cosmag.00090272. physics_L1Calo*. Trying to reproduce their results, TMVA cut optimization was applied to a single discriminating variable, both for the jet electromagnetic fraction and the number of tracks separately.

When evaluating the cut efficiencies for the jet electromagnetic fraction, so called Cone4H1 TowerJets are considered with $E_{\mathrm{T}} > 20$ GeV, following the requirements in [63]. The resulting TMVA output for the cut optimization is shown in Table 5.2. Since TMVA optimizes the cuts by iterating over the signal efficiency with a given step size, the cut values are sometimes not identical to the ones used in [63]. This is also the reason why for J3 and J6 there are slightly different cut values. Nevertheless, taking this into account the agreement with the values obtained in [63] (c.f. Table 5.3) is within 1%. In case of the number of tracks inside the jet, Cone4H1TowerJets are considered with $E_{\mathrm{T}} > 20$ GeV and the additional requirement

Cut	cosmic data	J3	J6
> 0.05	$(16.6 \pm 0.2)\%$	$(99.988 \pm 0.002)\%$	$(99.986 \pm 0.003)\%$
> 0.10	$(8.7 \pm 0.1)\%$	$(99.958 \pm 0.004)\%$	$(99.947 \pm 0.006)\%$
> 0.15	$(7.4 \pm 0.1)\%$	$(99.886 \pm 0.007)\%$	$(99.869 \pm 0.009)\%$
> 0.20	$(7.1 \pm 0.1)\%$	$(99.75 \pm 0.01)\%$	$(99.71 \pm 0.01)\%$
> 0.25	$(6.9 \pm 0.1)\%$	$(99.51 \pm 0.02)\%$	$(99.40 \pm 0.02)\%$
> 0.30	$(6.8 \pm 0.1)\%$	$(99.13 \pm 0.02)\%$	$(98.90 \pm 0.03)\%$

Table 5.3: Comparison for the breakdown of the ratio of jets remaining after different cut values on the jet electromagnetic fraction. Only statistical errors are considered. From [63]

Cut	cosmic data	J3	J6
≥ 1	$(1.02 \pm 0.06)\%$	$(99.95 \pm 0.01)\%$	$(99.93 \pm 0.01)\%$
≥ 2	$(0.08 \pm 0.02)\%$	$(99.66 \pm 0.03)\%$	$(99.79 \pm 0.02)\%$
≥ 3	$(0.015 \pm 0.008)\%$	$(98.95 \pm 0.05)\%$	$(99.43 \pm 0.03)\%$
≥ 4	$(0.008 \pm 0.005)\%$	$(97.35 \pm 0.07)\%$	$(98.67 \pm 0.04)\%$
≥ 5	-	$(94.6 \pm 0.1)\%$	$(97.30 \pm 0.06)\%$
≥ 7	-	$(85.2 \pm 0.2)\%$	$(92.8 \pm 0.1)\%$
≥ 10	-	$(63.8 \pm 0.2)\%$	$(82.7 \pm 0.1)\%$

Table 5.4: Breakdown for the ratio of jets remaining after different cut values on the number of tracks obtained with TMVA. Only statistical errors are considered.

of $|\eta| < 2.5$, again following [63]. The results obtained in this study (Table 5.4) for the cosmic data sample are in good agreement with the results from [63] (Table 5.5). While for the dijet samples the efficiencies for a cut of ≥ 1 are still in agreement, there is a tendency to have slightly higher efficiencies for higher number of tracks. In a signal efficiency range down to 94%, the results are still within 0.3% agreement, but for lower efficiencies the discrepancy reaches up to 1.5%. A reason for this could be the (presumably) slightly different definition of the track association to a jet and/or the use of reprocessed Monte Carlo samples.

After that, TMVA was used to optimize the cuts on several variables. The input variables are: electromagnetic fraction, tile2 fraction, tile10 fraction and charge fraction. Here, the charge fraction is prefered to the number of tracks because the cut optimization works better if one uses a floating point variable instead of an integer one. Moreover, number of tracks and charge fraction are highly correlated.

There is no η cut on the jets because the results for jets with $E_{\mathrm{T}} > 20$ GeV and $|\eta| < 2.5$ can hardly be improved as the background rejection is nearly 100% when requiring two or more reconstructed tracks per jet. This does not work so well for jets with $|\eta| \geq 2.5$, because here the number of tracks is also around zero for QCD jets, since those jets are outside of the tracker acceptance.

The input variable distributions for jets with $E_{\mathrm{T}} > 20$ GeV are shown in Figure 5.9. For charge fraction an artificial cutoff at 2.0 is introduced - i.e. all values bigger then 2.0 are set

Cut	cosmic data	J3	J6
≥ 1	$(1.02 \pm 0.04)\%$	$(99.938 \pm 0.006)\%$	$(99.924 \pm 0.008)\%$
≥ 2	$(0.048 \pm 0.009)\%$	$(99.65 \pm 0.01)\%$	$(99.75 \pm 0.01)\%$
≥ 3	$(0.015 \pm 0.005)\%$	$(98.84 \pm 0.03)\%$	$(99.32 \pm 0.02)\%$
≥ 4	$(0.007 \pm 0.004)\%$	$(97.07 \pm 0.04)\%$	$(98.50 \pm 0.03)\%$
≥ 5	$(0.002 \pm 0.002)\%$	$(94.10 \pm 0.06)\%$	$(97.03 \pm 0.05)\%$
≥ 7	-	$(84.06 \pm 0.09)\%$	$(92.30 \pm 0.07)\%$
≥ 10	-	$(62.4 \pm 0.1)\%$	$(82.0 \pm 0.1)\%$

Table 5.5: Comparison for the breakdown of the ratio of jets remaining after different cut values on the number of tracks. Only statistical errors are considered. From [63]

to 2.0. By so doing, TMVA has a better handle on that variable, and the physical information is not deteriorated.

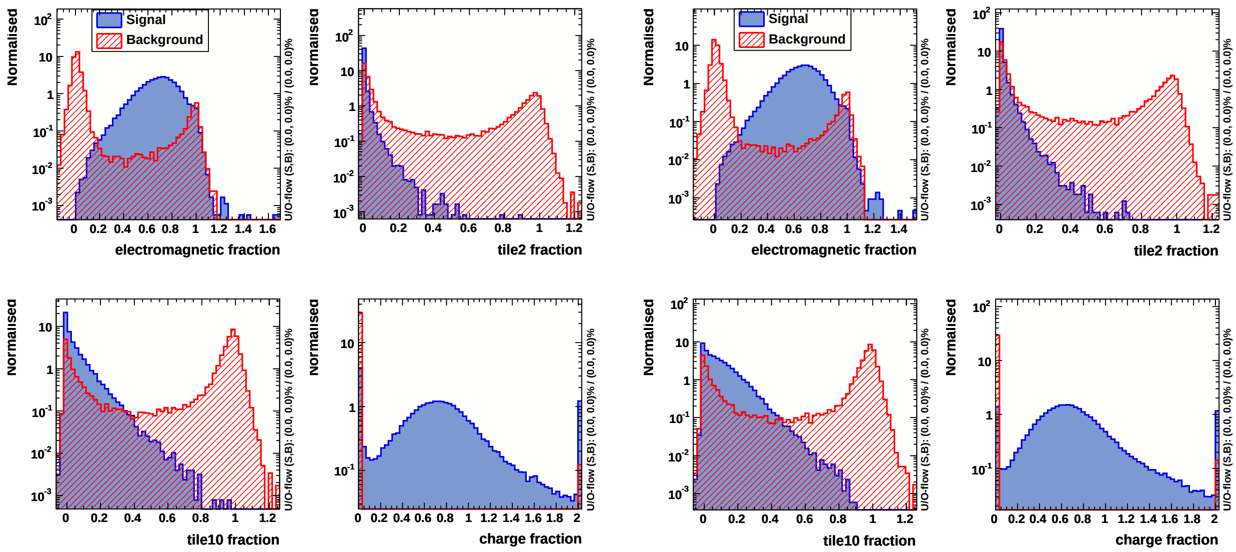

Figure 5.9: Input variables used by TMVA for signal J3 (left)/ J6 (right) and cosmic data (background) using jets with $E_{\mathrm{T}} > 20$ GeV

The result of the TMVA cut optimization is summarized in Table 5.6, Table 5.7 and Figure 5.10. The sudden jump in the ROC curve (Figure 5.10) to higher background rejection can be understood when looking at the cuts chosen by TMVA. For signal efficiencies down to 87.40% (J3) and 95.69% (J6), there is no cut on the charge fraction because any cut on that variable would lead to a lower signal efficiency. When the cut is activated at a signal efficiency of 87.39% (J3) and 95.68% (J6), the background rejection is better than 99%. The spike in the ROC curve for J3 at a signal efficiency of approx. 89% has a different source. In this case, TMVA just does not find a cut combination for this particular signal efficiency.

To avoid these problems, the samples were divided into two different regions in η – a low-η

efficiencies		cuts			
J3	cosmic data	electromagnetic fraction	fraction tile2	fraction tile10	charge fraction
99.99%	11.88%	>0.025	< 1.217	< 0.801	-
99.98%	8.62%	>0.055	< 0.576	< 0.793	-
99.96%	7.42%	>0.085	< 0.567	< 0.753	-
99.95%	7.32%	>0.093	< 0.558	< 0.753	-
99.89%	7.02%	>0.126	< 0.575	< 0.740	-
99.74%	6.83%	>0.169	< 0.559	< 0.675	-
99.51%	6.71%	>0.207	< 0.357	< 0.631	-
99.13%	6.59%	>0.200	< 0.243	< 0.405	-
87.40%	6.15%	>0.512	< 0.299	< 0.387	-
87.39%	0.58%	>0.018	< 1.145	< 1.070	> 0.0033
87.00%	0.20%	>0.196	< 0.924	<0.564	> 0.0017

Table 5.6: Breakdown extract for the ratio of jets remaining after different cuts optimized by TMVA for J3. Only statistical errors are considered. '-' means that no cut was placed on that variable.

efficiencies		cuts			
J6	cosmic data	electromagnetic fraction	fraction tile2	fraction tile10	charge fraction
99.99%	10.95%	>0.037	< 0.724	< 0.860	-
99.98%	9.81%	>0.049	< 0.724	< 0.860	-
99.96%	8.29%	>0.069	< 0.738	< 0.823	-
99.95%	7.85%	>0.084	< 0.733	< 0.823	-
99.87%	7.17%	>0.127	< 0.530	< 0.775	-
99.71%	6.90%	>0.169	< 0.567	< 0.639	-
99.40%	6.78%	>0.207	< 0.226	< 0.653	-
98.90%	6.68%	>0.264	< 0.205	< 0.824	-
95.69%	6.645%	>0.390	< 0.211	< 0.817	-
95.68%	0.948%	-	< 0.789	-	> 0.00085
95.60%	0.241%	>0.095	-	<0.789	> 0.0031

Table 5.7: Breakdown extract for the ratio of jets remaining after different cuts optimized by TMVA for J6. Only statistical errors are considered. '-' means that no cut was placed on that variable.

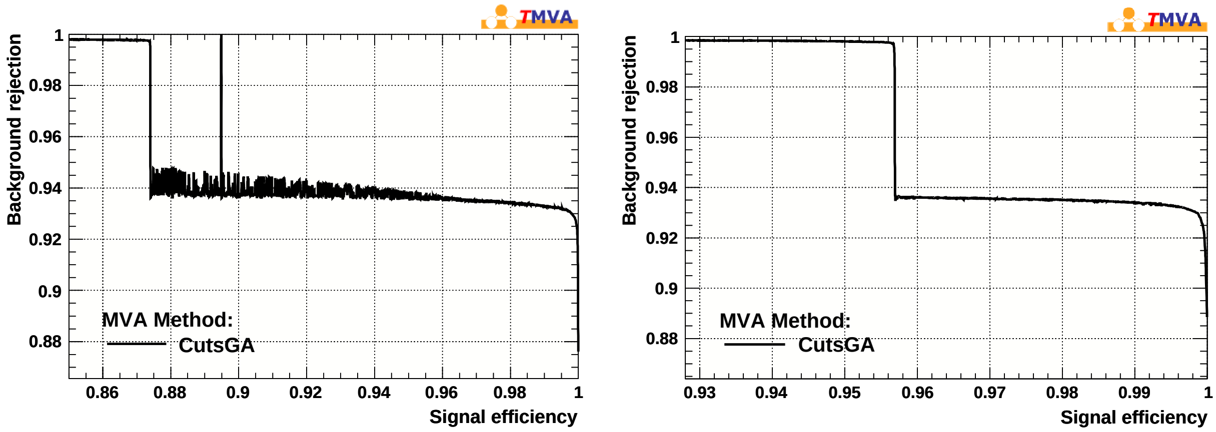

Figure 5.10: ROC curve for signal J3 (left) / J6 (right) and cosmic data (background) using jets with $E_{\mathrm{T}} > 20$ GeV.

region with $|\eta| < 2.5$ and a high-η region with $|\eta| \geq 2.5$. For the low-η region, a cut on the number of tracks was placed before the TMVA optimization takes place (number of tracks > 0). For the high-η region, no cut on this variable was placed. For both, the variable was excluded from the TMVA cut optimization procedure. Figure 5.11 shows the input variables for the low-η region after applying the precut on the number of tracks for J3 and the cosmic data background. The variable tile2 fraction loses most of its separation power. It was nevertheless included in the cut optimization procedure, because it does no harm. The statistics also get significantly lower, especially for the cosmic data sample. TMVA manages, however, to

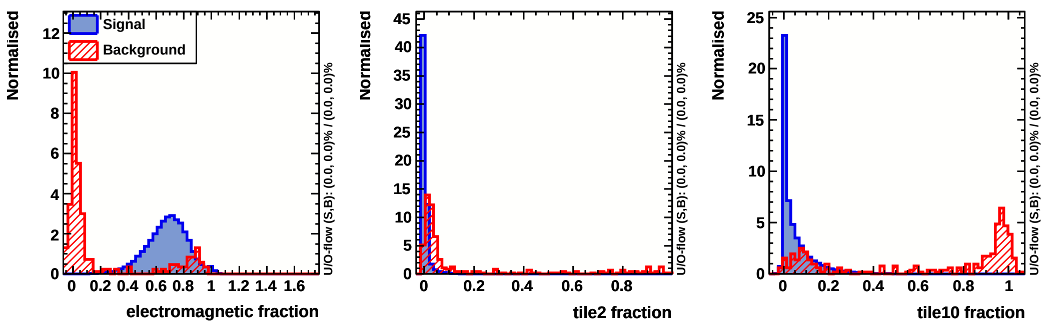

Figure 5.11: Input variables used by TMVA for signal J3 and cosmic data (background) using jets with $E_{\mathrm{T}} > 20$ GeV and a precut on the number of tracks for the low-η region.

optimize the three remaining variables (Table 5.8). In addition to the efficiencies stated in Table 5.8, one has to take the efficiency of the precut on the number of tracks into account, which is $(1.02 \pm 0.06)\%$ for cosmic data and $(99.96 \pm 0.01)\%$ for the J3 sample. The result is, that one gains a factor of 4 in background suppression for a signal efficiency of 99.9x%, compared to cutting on the number of tracks only. But one also observes that for lower signal

efficiencies		cuts		
J3	cosmic data	electromagnetic fraction	fraction tile2	fraction tile10
$(99.95 \pm 0.01)\%$	$(25.5 \pm 0.3)\%$	>0.088	< 0.583	< 0.805
$(99.00 \pm 0.05)\%$	$(21.0 \pm 0.3)\%$	>0.266	< 0.650	< 0.471
$(97.50 \pm 0.07)\%$	$(19.56 \pm 0.2)\%$	>0.275	< 0.062	< 0.531
$(95.0 \pm 0.1)\%$	$(14.39 \pm 0.2)\%$	>0.142	< 0.025	-

Table 5.8: Result of the optimization in the low-η region for J3 MC and cosmic data. Only statistical errors are considered.

efficiencies		cuts
J1	cosmics	number of tracks
$(97.83 \pm 0.07)\%$	$(1.80 \pm 0.08)\%$	>0
$(90.96 \pm 0.15)\%$	$(0.09 \pm 0.02)\%$	>1
$(78.9 \pm 0.2)\%$	$(0.01 \pm 0.02)\%$	>2
$(64.6 \pm 0.2)\%$	$(0 \pm 0.01)\%$	>3
$(49.7 \pm 0.3)\%$	$(0 \pm 0.01)\%$	>4
$(36.2 \pm 0.2)\%$	$(0 \pm 0.01)\%$	>5
$(25.2 \pm 0.2)\%$	$(0 \pm 0.01)\%$	>6
$(16.7 \pm 0.2)\%$	-	>7
$(10.56 \pm 0.16)\%$	-	>8
$(6.47 \pm 0.13)\%$	-	>9
$(3.92 \pm 0.10)\%$	-	>10

Table 5.9: Result of the optimization of the cut on the number of tracks in the low-η region for J1 MC and cosmic data. Only statistical errors are considered.

efficiencies, a harsher cut on the number of tracks leads to better results (compare Table 5.4).

The same was done for the J1 QCD dijet sample. Here, the cut on the jet transverse energy was lowered to 5 GeV. The cut efficiencies on the number of tracks are shown in Table 5.9. The input variables used by the TMVA cut optimization after applying the cut on the number of tracks (>0) are shown in Figure 5.12 for the low-η region and the result is shown in Table 5.10 (without the precut efficieny). For J1, the signal efficiency is a little bit worse than for J3 when applying similar cuts. This is expected, because of the lower energy jets in the sample. Nevertheless, a signal efficiency of more than 95% is achieved while about 99% of the cosmic ray background is rejected in the low-η region.

For the high-η region the statistics of the cosmic ray background is too low to optimize the cuts. However, Figure 5.13 shows that if the same cuts for electromagnetic fraction, tile2 fraction and tile10 fraction are applied as in the low-η region, the signal efficiency in the high-η region is preserved.

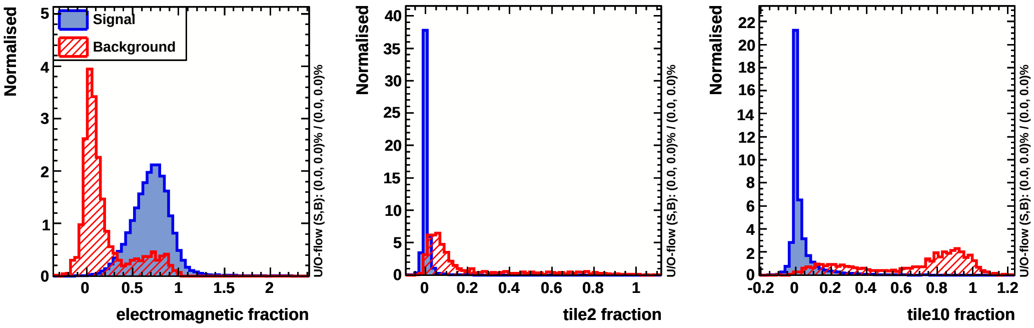

Figure 5.12: Input variables used by TMVA for signal J1 and cosmic data (background) using jets with $E_{\mathrm{T}} > 5$ GeV and a precut on the number of tracks for the low-η region.

efficiencies		cuts		
J1	cosmic data	electromagnetic fraction	fraction tile2	fraction tile10
$(99.95 \pm 0.01)\%$	$(43 \pm 1)\%$	-	< 0.584	< 0.730
$(99.00 \pm 0.05)\%$	$(20 \pm 1)\%$	>0.108	< 0.098	< 0.608
$(97.50 \pm 0.08)\%$	$(9.3 \pm 0.7)\%$	>0.111	< 0.042	< 0.637
$(95.0 \pm 0.1)\%$	$(6.1 \pm 0.6)\%$	>0.121	< 0.025	< 0.535

Table 5.10: Result of the optimization in the low-η region for J1 MC and cosmic data after the cut on the number of tracks was applied. Only statistical errors are considered.

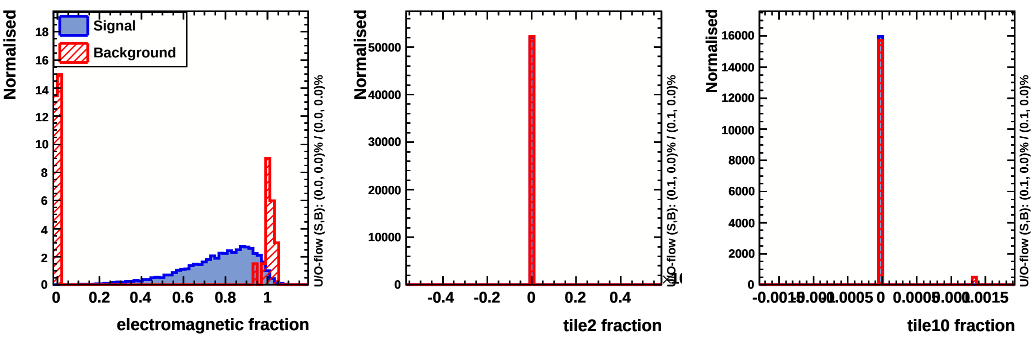

Figure 5.13: Input variables used by TMVA for signal J1 and cosmic ray data (background) using jets with $E_{\mathrm{T}} > 5$ GeV for the high-η region. Due to the geometric definition of the tile2 and tile10 fraction variables, they have no separation power in the high-η region.

5.5.4 Results for beam-gas background

The same procedure was applied to the beam-gas Monte Carlo sample (*mc08.108863.Hijing_beamgas.recon.AOD.e4_s470_r635_t53*). Also here a cut on the number of tracks was applied before the actual TMVA cut optimization took place. The cut on the transverse energy of the jets considered also had to be lowered significantly (to 5 GeV) due to the very soft jet E_{T} spectrum of the beam-gas sample (Figure 5.1). Figure 5.14 shows that practically none of the chosen calorimeter based variables has a significant separation power. But this can be understood when looking at the physical process of a beam-gas event, which is basically a fixed target collision and therefore should not look different in the calorimeter than an ordinary QCD event. Nevertheless, the optimization was attempted for the cut on the electromagnetic

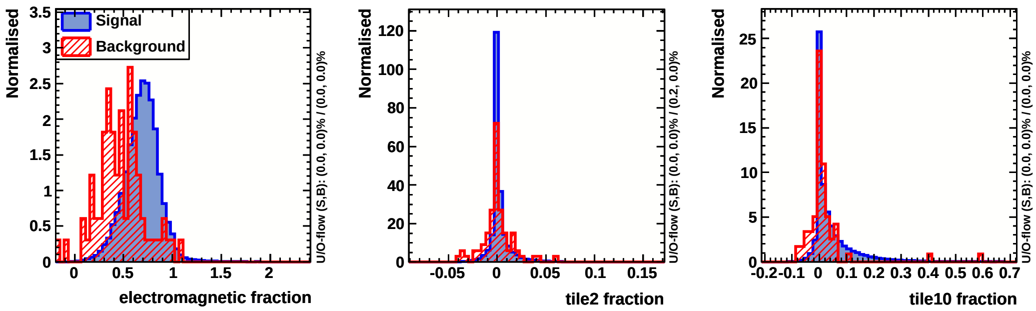

Figure 5.14: Input variables used by TMVA for signal J3 and beam-gas Monte Carlo (background) using jets with $E_{\mathrm{T}} > 5$ GeV and a precut on the number of tracks for the low-η region

fraction, since this is the variable that at least differs slightly for signal and background. Table 5.11 shows the result of the cut optimization for the electromagnetic fraction in the low-η region. In order to keep more than 99% of the J3 events, only about 10% of the beam-gas events can be suppressed using a cut in the jet electromagnetic fraction in the low-η region. Of course, one has to take the efficiency for the precut on the number of tracks into account (Table 5.12) as well.

On the other hand a track-based variable should be able to give some more discriminating power for beam-gas against QCD events. To check this hypothesis, the number of tracks variable was optimized using TMVA. The result is shown in Table 5.12. A cut on the number of tracks associated to the jet suppresses at least a good fraction (40 to 60%) of beam-gas events, while keeping over 95% of the J3 QCD events. But this, of course, only works for jets with decent tracking information. On the other hand, a cut on the transverse energy of the jet of 20 GeV would remove nearly all beam-gas events. If many of these low E_{T} jets overlapped with a QCD event, this also would lead to a significant deterioration of the missing transverse energy description.

Since the transverse energy spectrum of the beam-gas events tends to be soft (Figure 5.1), the QCD dijet J1 sample was also used to train and test the cut optimization leading to similar results [52].

In the high-η region, the statistic in the beam-gas sample is too small for a proper cut

efficiencies		cuts
J3	beam-gas MC	electromagnetic fraction
$(99.50 \pm 0.03)\%$	$(89 \pm 3)\%$	>0.179
$(99.00 \pm 0.04)\%$	$(87 \pm 3)\%$	>0.238
$(98.00 \pm 0.05)\%$	$(78 \pm 4)\%$	>0.301
$(97.00 \pm 0.06)\%$	$(74 \pm 4)\%$	>0.337
$(96.00 \pm 0.07)\%$	$(64 \pm 4)\%$	>0.367
$(95.00 \pm 0.08)\%$	$(61 \pm 5)\%$	>0.389
$(94.00 \pm 0.08)\%$	$(57 \pm 5)\%$	>0.407
$(93.00 \pm 0.09)\%$	$(54 \pm 5)\%$	>0.423
$(92.0 \pm 0.1)\%$	$(54 \pm 5)\%$	>0.439
$(91.0 \pm 0.1)\%$	$(53 \pm 5)\%$	>0.452
$(90.0 \pm 0.1)\%$	$(49 \pm 5)\%$	>0.465
$(85.0 \pm 0.1)\%$	$(42 \pm 5)\%$	>0.513

Table 5.11: Result of the optimization of cut on the electromagnetic fraction in the low-η region for J3 and beam-gas MC. Only statistical errors are considered.

efficiencies		cuts
J3	beam-gas MC	number of tracks
$(98.88 \pm 0.04)\%$	$(66 \pm 4)\%$	>0
$(95.44 \pm 0.07)\%$	$(39 \pm 4)\%$	>1
$(89.6 \pm 0.1)\%$	$(27 \pm 4)\%$	>2
$(82.4 \pm 0.1)\%$	$(19 \pm 3)\%$	>3
$(74.7 \pm 0.1)\%$	$(11 \pm 3)\%$	>4
$(67.4 \pm 0.2)\%$	$(11 \pm 3)\%$	>5
$(60.1 \pm 0.2)\%$	$(6 \pm 3)\%$	>6
$(53.4 \pm 0.2)\%$	$(3 \pm 2)\%$	>7
$(47.1 \pm 0.2)\%$	$(1.7 \pm 1.2)\%$	>8
$(41.2 \pm 0.2)\%$	$(0.85 \pm 0.85)\%$	>9
$(35.8 \pm 0.2)\%$	-	>10

Table 5.12: Result of the optimization of cut on the number of tracks in the low-η region for J3 and beam-gas MC. Only statistical errors are considered.

optimization. Therefore, no jet cleanup procedure for beam-gas events can be suggested in this region. The low statistics show, however, that the influence of the background in the high-η region is sub-dominant.

5.5.5 Results for beam halo background

Since there are almost no jet fakes in the available beam halo samples, it is not possible to suggest any jet cleanup cuts in order to suppress this background. However, it might be possible to use, not jet, but event cleanup cuts.

5.6 Event cleaning cuts

The goal of event cleaning cuts is not to distinguish between good and fake jets but suppress events with a large fake jet contamination. In order to do so, the total electromagnetic fraction of the event was computed from the information available in so-called "TAG_COMM" files. "TAG_COMM" files are small ROOT n-tuples derived from RDOs [54].

$$\text{total electromagnetic fraction} = \frac{\text{energy deposited in EMB and EMEC (for the whole event)}}{\text{energy deposited in all layers (for the whole event)}} \quad (5.7)$$

Figure 5.15 shows the total electromagnetic fraction for the single-beam run 88128, the beam-gas and beam halo Monte Carlo. The slight shift in the mean of the distribution to higher values for the single-beam run compared to the Monte Carlo distributions might be due to the significantly lower beam energy. If the beam energy is lower, the produced particles are less energetic, and are therefore stopped earlier in the calorimeters (i.e. more energy is deposited in the electromagnetic calorimeter). Nevertheless, the differences in the distributions are minor. The total electromagnetic fraction can take values lower than zero and greater than one because of noise correction contributions to the energies in the different calorimeter parts.

According to [65], the electromagnetic fraction should have at least some separation power. In order to proof this hypothesis, the total electromagentic fraction for beam-gas and beam halo Monte Carlo is plotted, together with various QCD dijet `Pythia` Monte Carlo samples (Figure 5.16).

Especially a cut on the lower edge of the distribution would remove a fair fraction of beam halo- and beam-gas-related background from the event selection. As a first quantitative test, the efficiencies of the various samples were computed for a soft ($0.0 <$ total electromagnetic fraction < 0.6) and a harsh cut ($0.1 <$ total electromagnetic fraction < 0.6) scenario (Table 5.13).

The cut on the total electromagnetic fraction does remove a good part of the beam-related background, but still the performance is not satisfying. Therefore, it was investigated how a cut on the number and position of the primary vertex in the event performs, because - as explained in Section 5.4 - this should be very different for QCD dijets and beam related background.

As expected, all investigated QCD dijet events (for J1, J3, J6) do have a primary vertex near the interaction point. For beam-gas, 99770 out of 99779 $(99.999\pm0.001)\%$ events do not

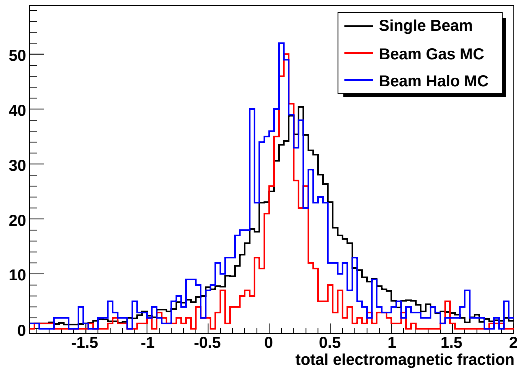

Figure 5.15: Total electromagnetic fraction for single-beam run 88128 (scaled down by factor 10), beam-gas and beam halo MC.

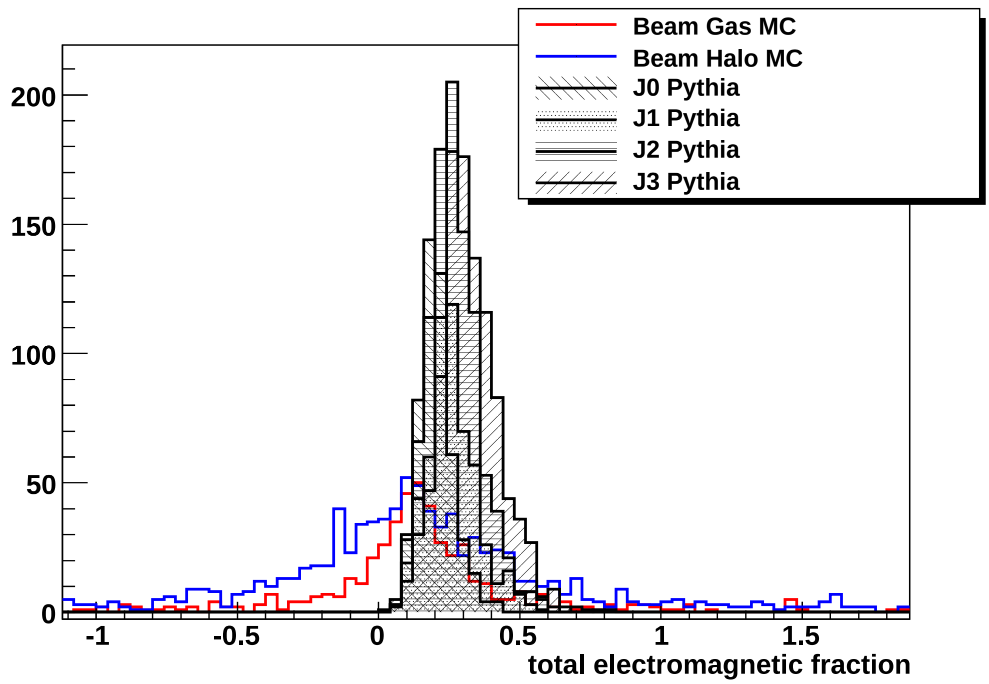

Figure 5.16: Total electromagnetic fraction for beam-gas and halo MC as well as for various `Pythia` dijet MC samples. The histograms are normalized arbitrarily.

soft cut (0.0 < emfrac < 0.6)

sample	efficiency
beam-gas	(64.8±1.7)%
beam halo	(44.2±1.0)%
single-beam	(45.7±0.3)%
J0	100%
J1	100%
J2	(99.4±0.2)%
J3	(98.8±0.2)%

harsh cut (0.1 < emfrac < 0.6)

sample	efficiency
beam-gas	(48.2±1.5)%
beam halo	(34.2±0.9)%
single-beam	(38.2±0.3)%
J0	(98.2±0.6)%
J1	(98.5±0.5)%
J2	(97.9±0.4)%
J3	(97.8±0.5)%

Table 5.13: Efficiencies for the various samples when applying a cut on the total electromagnetic fraction (emfrac). A soft (left) and a harsh cut scenario (right) is proposed.

sample	efficiency
beam-gas	(0.001±0.001)%
beam halo	0%
J1	100%
J3	100%
J6	100%

Table 5.14: Efficiencies after requiring a reconstructed primary vertex near the interaction point.

have a primary vertex reconstructed (Table 5.14). For beam halo, the mc08 sample suffered from a bug in the vertex reconstruction, but for the reprocessed mc09 sample the vertex information was available. Here one finds that none of the events have a primary vertex reconstructed. This suggests, that beam halo events can be suppressed while keeping all QCD dijet events. It was checked that this result is not due to errors in the used script or missing algorithms by running the identical script with the identical Athena version once again for the beam-gas sample. The same result as quoted above was obtained. Furthermore, there is a dummy vertex for every event in the beam halo sample, which means that the vertex algorithm was run during reconstruction.

5.7 Estimations for expected background rates

The rate for cosmic muons that will leave energy in the calorimeters is estimated in [66]. For a minimal energy deposition in the electromagnetic calorimeter of 5 GeV, the rate is estimated to be 0.6 Hz. For a minimal energy deposition in the Tile calorimeter of 20 GeV, the rate it is estimated to be 2.0 Hz. Both rates come with a systematic error of about 10-15%.

In [67], the rate for beam-gas events at nominal LHC conditions is estimated to be 400 Hz. At LHC startup, this rate would go down to 4 Hz. Also in [67], there is given an estimate for the expected beam halo rate. The overall beam halo rate can be derived from the beam loss rates, which are given in [67] for IP5. They are 2.61 MHz on TCT.B2R5[3] from collimator tails, 3.07 MHz at TCT.B2R5 from elastic beam-gas interactions, and 2.32 MHz from inelastic beam-gas interactions. All three contributions should be roughly equal. Regarding only the expected rates, the beam halo background should dominate over the background coming from beam-gas events. However, the E_{T} spectrum of beam halo events appears to be much softer than the one of beam-gas events (Figures 5.1 and 5.3).

5.8 Discussion and summary

Various Monte Carlo and data samples were investigated by looking at different spectra, such as overall transverse energy, jet transverse energy or missing transverse energy. By doing that, the Monte Carlo predictions were compared to the theoretical predictions (for beam-gas events) and to some extent to the available single-beam data observations. The Monte Carlo simulations needed further careful validation with data, but the results are consistent with the little single-beam data available at the time the study was done.

Comparing the results of the cut optimization for cosmic ray data against J3 and J6 for the single variables electromagnetic fraction and number of jets, one finds a very good agreement with existing results [63]. This verifies that the optimization procedure actually works. In order to use the tracking information in an optimal way, the samples were split into a low and high-η region. For the low-η region a cut on the number of tracks > 0 was applied. This value keeps the signal efficiency for all signal samples above 95%. After that, the variables electromagnetic fraction, tile2 and tile10 fraction were optimized by TMVA using a genetic algorithm that optimizes rectangular cuts. The simplicity of the method allows to directly obtain cuts from the multivariate technique. By using multivariate techniques, one gains a factor of four in background suppression (compared to a single cut on number of tracks), while keeping the same signal efficiency. In the low-η region, the following set of cuts are proposed, taking into account the results for cosmic ray data and beam-gas Monte Carlo:
number tracks > 0, electromagnetic fraction > 0.1, tile2 fraction < 0.1, tile10 fraction < 0.7

Of course, this depends on the specific use cases. To suppress more background, it turns out to be better to have a harsher cut on the number of tracks than trying to optimize the remaining variables any further.

For the high-η region, the variables were optimized without cutting on the number of tracks since the tracking information in that region is limited or nonexistent. Also, the statistics in that region are very low for all considered backgrounds. Nevertheless, it was verified (for cosmic data) that one can apply the same cuts as in the low-η region without spoiling the signal efficiency in the high-η region.

Background arising from cosmic rays can be suppressed by 99% using the proposed cuts, and the much more difficult beam-gas background can be reduced by at least 30 to 60%. For background coming from beam halo interactions it is not possible to suggest any jet cleanup cuts because of the low jets statistics in the Monte Carlo sample. Therefore, the use of event cleanup cuts is studied in order to suppress this background. For event cleaning, two variables were tested, the total electromagnetic fraction and the number and position of the primary

[3] tertiary collimator

vertex. For the total electromagnetic fraction, a soft and a harsh cut scenario is suggested, for which a fair background suppression was achieved, accompanied with a high signal acceptance cut (Table 5.13). If one requires a primary vertex candidate to be present in the event, close to 100% of all beam-gas and all beam halo events can be suppressed while preserving all QCD dijet events. This result emphasizes the importance of a primary vertex event cleaning cut.

Considering the cleaning cuts that are used in the data analysis in 2010 (c.f. Chapters 6 and 7), this very early study provided useful insights and contributed to the development of the final cleaning cuts proposed by the Jet$E_{\mathrm{T}}^{\mathrm{miss}}$ group.

Chapter 6

Searches in events with two or three jets

6.1 Introduction

This chapter summarizes the searches for squark and gluinos in the two and three jet channel without isolated leptons, which are described in more detail in [68] and published in [69]. The author has contributed to this publication by developing a data driven estimation of the QCD background under the supervision of Zuzana Rurikova. Hence, the main focus of this chapter is on the QCD background determination. The results of other data-driven background estimations, that were done in [68] are quoted. All the signal selection cuts were implemented and the final numbers for the signal regions were reproduced. Furthermore, the exclusion potential of the two and three jet analysis in the MSSM is quoted [68] and the possible exclusion potential for the Split SUSY model is estimated and compared to the one achieved in the monojet channel, which will be discussed in the next chapter.

Section 6.2 introduces the various data and Monte Carlo samples that were used in [68], followed by the object definitions, event selection cuts and a summary on trigger studies. After that, the QCD background determination method, which was developed for [68] is described in detail, followed by a brief description of other background estimation methods, that are used in [68]. After summarizing the signal models, the results of the first ATLAS searches for squarks and gluinos in channels with two or three jets and no isolated leptons [68] are quoted accompanied by a brief description of the limit setting procedure, that is used for the analysis and is described in detail in [70].

6.2 Datasets

The datasets used for this study are all taken from the ATLAS central production reconstructed with Athena release 15. All AODs from the central production (for data as well as for Monte Carlo) were converted into so-called SUSYD3PDs (c.f. Section 3.3) via the SUSYD3PDMaker package version 00-06–14 or 00-06–20 [1].

[1] Version 00-06–14 and 00-06–20 do not differ substantially and can be used together

6.2.1 Data

This analysis uses the data collected from March 30th to October 29th 2010, which corresponds to the data taking periods A–I. The L1Calo stream was used for periods A–D while for periods E–I the JetTauEtmiss stream was used due to the increasing collision rate. The total integrated luminosity of the mentioned datasets is $\mathcal{L} = 45 \pm 5$ pb^{-1} before any data quality requirements are applied. After applying the good run list (GRL) selection [2] , this is reduced to 35 ± 4pb^{-1}.

6.2.2 Monte Carlo simulation

The signal and background Monte Carlo samples used for the comparison with the data were generated at $\sqrt{s} = 7$ TeV. During generation a special set of parameters, which were tuned by ATLAS for its 2009 Monte Carlo generation [71], was used for the samples generated with `Pythia` [22] and `Herwig` [23, 24] (with `JIMMY` [25]). All samples were passed through the `GEANT4` [43] based full detector simulation and were reconstructed with the same algorithms as used for data. A detailed list of all the samples used in the study can be found in Appendix C.1.

Vector bosons plus jets production
The W and Z production associated with jets is considered to be one of the most important backgrounds in searches for supersymmetry. Considering that the event selection requires multiple jets, it is of great importance that multiparton final states are modeled correctly. Therefore, the `Alpgen` (v2.13) [27] Monte Carlo generator was chosen to provide the prediction for this background. Since it is possible to generate jet production using up to five-parton matrix elements, this should give a rather accurate prediction of the final states. `Herwig` [23, 24] was used for showering and fragmentation and `JIMMY` [25] for modeling the underlying event. For all the samples (listed in detail in Table C.1 and C.2) the CTEQ6L1 [72] parton density functions were used. Next-to-next-to-leading order QCD corrections from `FEWZ` [73, 30] were used to get an overall normalization for the inclusive $W \rightarrow l\nu$ and $Z \rightarrow ll$ processes.

Top production
The production of $t\bar{t}$ and also single top is a relevant background for the search channels described in this study. For the hard processes the `MC@NLO` generator [28, 74] provides full next-to-leading order QCD corrections. Again, `Herwig` [23, 24] and `JIMMY` [25] were used to model the showering and fragmentation and the underlying event, respectively. The CTEQ6.6 next-to-leading-order parton density function set was used for the matrix element, the parton shower and the underlying event. The cross sections are normalized to next-to-leading order and next-to-leading log results [75]. All samples are listed with details in Table C.3.

QCD jets production
Using the leading order $2 \rightarrow 2$ QCD matrix elements, a large inclusive jet sample was generated with `Pythia` 6.4.21 [3]. The modified leading order parton distributions of MRST 2007 LO*

[2] The GRL selection ensures, that all detector components relevant for the analysis were ON and working properly. It also ensures, that there were no problems concerning the triggers, which are used in the analysis.
[3] The top quark production is not included in this sample

[76] were used for this sample. The leading logarithm parton shower approach, which is implemented in `Pythia`, is expected to give a good description of the data for relatively low p_{T} jets. According to the recipe described later in Section 6.4.1, the Monte Carlo prediction was normalized to data in a control region.

The `Pythia` prediction has been compared to an `Alpgen` prediction after both had been normalized to data and the remaining differences were found to be smaller than the experimental uncertainties [68]. Details on the QCD samples are listed in Table C.4.

Supersymmetry signal production

For illustrative purposes, kinematic distributions are compared to the prediction from the low mass supersymmetric mSUGRA [77, 78] benchmark point called SU4, which is chosen to be close to the Tevatron limits [79, 80]: $m_0 = 200\,\mathrm{GeV}$, $m_{1/2} = 160\,\mathrm{GeV}$, $A_0 = -400\,\mathrm{GeV}$, $\tan\beta = 10$ and $\mu > 0$. `ISAJET` [26] version 7.75 was used to calculate the mass spectrum and branching ratios and a sample of 5×10^4 events was generated using `Herwig++` [81, 82] with MRST 2007 LO* parton distributions [76]. The next-to-leading order cross section computed with `Prospino` [83] was found to be 59.9 pb [68].

For the final interpretation of the search results, two signal grids [68] are used. One was created in the context of the constraint MSSM, where SUSY breaking is mediated by gravitational interaction (mSUGRA). Two of the five parameters of the model - the common boson mass m_0 and the common fermion mass $m_{1/2}$ - were varied, while the other parameters were fixed at $A_0 = 0$, $\tan\beta = 3$ and $\mu > 0$.

The other model is more phenomenologically motivated. Since one is essentially interested in the production of squark and gluinos, their production is constraint isolated from other sparticles in the theory. This is ensured by setting the masses of other sparticles to 5 TeV. This way they don't play an important role for the dynamics. The three free parameters, that are left, are the mass of the gluino, the lightest neutralino and the common squark mass for the first two generations. The mass of the lightest neutralino was fixed to zero and the sampling was done over the mass of the gluino and the common squark mass.

Next-to-leading order `Prospino` cross sections were computed for both grids and the following systematic uncertainties were taken into account for the signal: The theoretical uncertainties (from PDF and renormalization scale variations), the jet energy scale and the jet energy resolution uncertainty, which are all added in quadrature for each subprocess. Details on the signal generation and the uncertainties can be found in the corresponding chapters of [68].

Both grids do not include the specific SU4 point, thus for the final distributions a signal point very similar to SU4 was chosen: $m_0 = 200\,\mathrm{GeV}$, $m_{1/2} = 190\,\mathrm{GeV}$, $A_0 = 0$, $\tan\beta = 3$ and $\mu > 0$. Leading to a slightly higher mass spectrum the next-to-leading order `Prospino` cross section is 19.4 pb [68]. Both signal points are listed with details in Table C.5.

6.3 Object and cut definitions

This section summarizes the definition of the objects, which are relevant for the analysis, the trigger and the event selection criteria.

6.3.1 Object definition

Since there is a veto on leptons in the analysis, electrons and muons have to be defined as well as jets and $E_{\mathrm{T}}^{\mathrm{miss}}$.

Jets are reconstructed with the anti-k_t jet algorithm [84], which uses topological clusters [85] as input. The distance parameter was chosen to be $R = 0.4$ to account for a large jet multiplicity typical for potential supersymmetry events in the multijet channels.

Since the jet momentum is measured at the electromagnetic scale, a calibration procedure known as *Jet Numerical Inversion Correction* was applied to all jets. The correct transverse momentum is computed via a correction factor, which is determined as a function of the uncorrected transverse momentum $p_T^{\mathrm{jet,em}}$ and the rapidity $|y^{\mathrm{jet}}|$: $p_T^{\mathrm{jet}} = C(p_T^{\mathrm{jet,em}}, y^{\mathrm{jet}}) \times p_T^{\mathrm{jet,em}}$. Furthermore two acceptance cuts are imposed: $p_{\mathrm{T}} > 20$ GeV and $|\eta| < 2.5$.

Electrons are defined by the robust medium-purity cuts described in [50, 86] using the *AuthorElectron* algorithm and by the following additional acceptance cuts. The transverse momentum of the electron should be bigger than 10 GeV and the pseudorapidity is required to be within $|\eta| < 2.47$.

Furthermore, electron candidates must not touch a dead OTX region in the calorimeters[4] and the event is also discarded, if an electron is found in the barrel-endcap transition region defined by $(1.37 < |\eta^{\mathrm{clust}}| < 1.52)$

Muons are reconstructed by an algorithm described in [49], which performs a combination of inner detector (ID) tracks and tracks reconstructed in the muon spectrometer (MS). One distinguishes between "combined" muons, which are made from tracks independently reconstructed both in the ID and the MS with the *STACO* algorithm [51], and "segment-tagged" muons, for which the MS is only used to tag ID tracks as muons and is not required to give a fully reconstructed track.

Muons are required to be isolated by confining the energy within a cone of $\Delta R = 0.2$ to less than 1.8 GeV. In addition the acceptance cuts $p_{\mathrm{T}} > 10$ GeV and $|\eta| < 2.4$ are applied.

Missing transverse momentum is calculated at AOD level with an object-based algorithm using topological clusters [85], since cells are not available at the AOD level. The $E_{\mathrm{T}}^{\mathrm{miss}}$ used in this analysis is given by:

$$(E_{\mathrm{T}}^{\mathrm{miss}})_{\mathrm{x(y)}}^{\mathrm{RefFinal}} = (E_{\mathrm{T}}^{\mathrm{miss}})_{\mathrm{x(y)}}^{\mathrm{RefEle}} + (E_{\mathrm{T}}^{\mathrm{miss}})_{\mathrm{x(y)}}^{\mathrm{RefJet}} + (E_{\mathrm{T}}^{\mathrm{miss}})_{\mathrm{x(y)}}^{\mathrm{RefMuo}} + (E_{\mathrm{T}}^{\mathrm{miss}})_{\mathrm{x(y)}}^{\mathrm{CellOut}} \tag{6.1}$$

The *RefEle* and *RefJet* terms in Equation 6.1 correspond to the negative sum of cluster energies inside the accordant objects. Electrons fulfilling the medium-purity criteria are included in *RefEle* and jets at the jet energy scale with $p_{\mathrm{T}} > 20$ GeV and no η constraint are included in *RefJet*. Both terms are computed before overlap removal. The *RefMuo* term corresponds to the negative transverse energy sum of muons calculated according to the above mentioned criteria except for the isolation and before overlap removal. Clusters not associated to any

[4]Problematic regions (e.g. due to failing power supplies) in the calorimeters are flagged as bad.

object are included in the *CellOut* term, in particular jets with $p_T < 20$ GeV. All but the *CellOut* term are calibrated.

6.3.2 Treatment of overlapping objects

When there is an overlap of two or more candidates passing the object selection criteria described above, one needs to decide how to remove all but one of the objects. The procedure is necessary to avoid double counting of the energies assigned to one physical object, that is reconstructed as two or more objects. Furthermore, the overlap removal ensures, that only isolated leptons are considered and not the ones created in the fragmentation of jets. The classifications are based on a simple geometrical $\Delta R = \sqrt{\Delta\phi^2 + \Delta\eta^2}$ approach, that has been studied in [49]. The following criteria are applied in this exact order [68]:

1. If an electron and a jet are found within $\Delta R < 0.2$, the object is interpreted as an electron and the overlapping 'jet' is ignored.
2. If a muon and a jet are found within $\Delta R < 0.4$, the object is treated as a jet and the 'muon' is rejected.
3. If an electron and a jet are found within $0.2 \leq \Delta R < 0.4$, the object is interpreted as a jet and the nearby 'electron' is ignored.

6.3.3 Event cleaning

As already mentioned and extensively studied in Chapter 5, non-collision background arising from various different sources has to be controlled. For this reason, the official recommendations from the ATLAS JetE_T^{miss}group [87] have been adopted, which uses several different jet and event variables to veto events containing non collision background. The following list introduces the variables used for the cleaning procedure [68]:

- f_{em}: energy fraction in the electromagnetic calorimeter
- f_{hec}: energy fraction in the hadronic end-cap calorimeter (HEC)
- n_{90}: minimum number of cells containing at least 90 % of the cluster energy
- f_Q: fraction of LAr cells with a cell quality factor greater than 4000. The cell Q-factor measures the difference between the measured pulse shape and the predicted pulse shape that is used to reconstruct the cell energy.
- t_{jet}: jet timing computed as the energy squared cells mean time
- f_{max}: maximum energy fraction in one calorimeter layer
- f_{ch}: jet charge fraction defined as sum of tracks [5] p_T associated to the jet divided by the jet p_T.

[5]Tracks associated to the jets should satisfy: $p_T > 500$ MeV, $|\eta| < 2.5$, transverse impact parameter with respect to the primary vertex $|d_0| < 1.5$ mm, longitudinal impact parameter with respect to the primary vertex $|z_0 \times \sin\theta| < 1.5$ mm, at least 6 hits in the Silicon Tracker (SCT) detector, at least 1 hit in the Pixel detector and the distance between the jet and the track $\Delta R < 0.4$. [68]

Source of fake jets	*Loose*	*Tight*=*Loose* plus
EM coherent noise	f_{em} >0.95 and f_{Q} >0.8 or	f_{em} >0.90 and f_{Q} >0.6 or
HEC spikes	f_{hec} >0.8 and n_{90} <=5 or f_{hec} >0.5 and f_{Q} >0.5 or	f_{hec} >0.3 and f_{Q} >0.3 or f_{hec} >1-f_{Q} or
Cosmics and beam-background	t_{jet} >25ns or f_{em} <0.05 or f_{max} >0.99 and $\lvert\eta\rvert < 2$	f_{em} <0.1 or f_{max} >0.95 and $\lvert\eta\rvert < 2$

Table 6.1: Loose and tight bad jet definition according to [87].

The Jet$E_{\mathrm{T}}^{\mathrm{miss}}$group provided recommendations for identifying different levels of so-called "bad" jets, which are summarized in Table 6.1 [87]. The chosen variables and recommendations were established with a fair amount of collision data and therefore differ from the ones proposed in Chapter 5, where only single beam and cosmic data were available.

For the dijet selection, events with jets flagged as bad according to the *Tight* criteria are vetoed, whereas for the three jet selection only events containing jets flagged as bad according to the *Loose* criteria are dropped. For this, jets with $p_{\mathrm{T}} > 20$ GeV and no restriction on the pseudorapidity are considered.

In addition, a cut in the charge fraction (f_{ch}) of the leading jets is applied to remove background arising from cosmic muons. The event is removed, if the leading two jets fulfills $f_{\mathrm{ch}} < 0.02$, $p_{\mathrm{T}} > 120$ GeV and $|\eta| < 2$ for the di-jet selection or the leading three jets satisfy $f_{\mathrm{ch}} < 0.02$, $f_{\mathrm{em}} > 0.98$ and $|\eta| < 2$ for the three jet channel. In order to furthermore suppress non-collision beam background, only events are accepted, which contain a primary vertex with at least 5 tracks associated to it.

6.3.4 Event selection

Trigger

For the majority of the data especially at higher instantaneous luminosity the `EF_j75_jetNoEF_EFxe25_noMu` trigger was used. For early data taking periods and the MC samples this trigger was emulated, since the original trigger was not available. A summary of the triggers in use is given in Table 6.2.

The trigger is based on a jet p_{T} selection at L1 and L2 plus an additional $E_{\mathrm{T}}^{\mathrm{miss}}$ selection at EF level. The `noMu` tag stands for the fact, that muons were not included in the $E_{\mathrm{T}}^{\mathrm{miss}}$ definition. Extensive trigger studies have been done in [68]. The turn on curve for the `EF_j75_jetNoEF_EFxe25_noMu` trigger is shown in Figure 6.1. It shows, that the trigger reaches

Period	Stream	Trigger (Data)
A-F (and MC)	JetTauEtmiss (or L1Calo)	`L1_J55` cut at trig_L2_jet_pt> 70 GeV cut at $E_{\mathrm{T}}^{\mathrm{miss}} > 25$ GeV at EF
G (runs 1658*)	JetTauEtmiss	`EF_j75_jetNoEF` cut at $E_{\mathrm{T}}^{\mathrm{miss}} > 25$ GeV (EF)
G-I (excl. 1658*)	JetTauEtmiss	`EF_j75_jetNoEF_EFxe25_noMu`

Table 6.2: Triggers used in the analysis by period. According to [68].

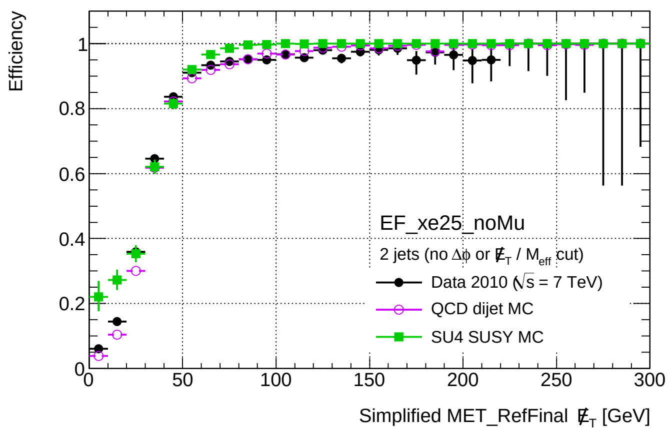

Figure 6.1: The efficiency of the `EF_j75_jetNoEF_EFxe25_noMu` trigger as a function of $E_{\mathrm{T}}^{\mathrm{miss}}$ for events passing `L2_J70`, as well as the offline selection requiring the leading two jets to have $p_{\mathrm{T}} > 120, 40$ GeV. Taken from [68].

its plateau for $E_{\mathrm{T}}^{\mathrm{miss}} > 100$ GeV. For the analysis it is essential to choose the offline cuts such, that the trigger is in the plateau region and that it is well described by the MC. This motivated the offline cuts on the $E_{\mathrm{T}}^{\mathrm{miss}}$ and the p_{T} of the leading jet, which are described in the following.

Offline selection cuts

After the events have passed the trigger selection described above and events with one or more reconstructed electrons or muons (after overlap removal and with $p_{\mathrm{T}} > 10$ GeV) have been vetoed, fiducial cuts are applied to define the signal regions. These are based on the jet p_{T}, the missing transverse energy $E_{\mathrm{T}}^{\mathrm{miss}}$, the effective mass m_{eff} and the stransverse mass m_{T2} variables, which are defined as follows:

The effective mass is defined as the scalar sum of the transverse momenta of the leading jets and the missing transverse energy according to:

$$m_{\mathrm{eff}} \equiv \sum_{i=1}^{n} |\mathbf{p}_{\mathrm{T}}^{(i)}| + E_{\mathrm{T}}^{\mathrm{miss}} \tag{6.2}$$

with n denoting the number of leading jets defining the analysis channel (two or three). This variable tends to be larger for heavier sparticles potentially produced in the event.

The stransverse mass is a generalization of the transverse mass for pair decays and defined as [68]:

$$m_{\mathrm{T2}}\left(\mathbf{p}_{\mathrm{T}}^{(1)}, \mathbf{p}_{\mathrm{T}}^{(2)}, \mathbf{E}_{\mathrm{T}}^{\mathrm{miss}}\right) \equiv \min_{\not{q}_{\mathrm{T}}^{(1)}+\not{q}_{\mathrm{T}}^{(2)}=\vec{E}_{\mathrm{T}}^{\mathrm{miss}}} \left\{\max\left(m_{\mathrm{T}}\left(\mathbf{p}_{\mathrm{T}}^{(1)}, \not{q}_{\mathrm{T}}^{(1)}\right),\ m_{\mathrm{T}}\left(\mathbf{p}_{\mathrm{T}}^{(2)}, \not{q}_{\mathrm{T}}^{(2)}\right)\right)\right\} \tag{6.3}$$

with m_{T} being the transverse mass, $\mathbf{p}_{\mathrm{T}}^{(1,2)}$ the transverse momenta of the leading jets, $\mathbf{E}_{\mathrm{T}}^{\mathrm{miss}}$ the missing transverse momentum and the minimization being done over all possible values of two undetectable particles' transverse momenta $\not{q}_{\mathrm{T}}^{(1,2)}$, which are consistent with the $E_{\mathrm{T}}^{\mathrm{miss}}$ constraint. By requiring a high value of the stransverse mass it is not only possible to suppress most of the SM background [88], but one is also extremely sensitive to any pair-produced semi-invisible decaying particles [89].

In order to cover different areas in the squark-gluino mass plane, four signal regions were defined [68] - two for each 2 jet and the 3 jet channel. A summary of the applied kinematic cuts for each region is given in Table 6.3

The cuts on the azimuthal angle between the jets and the missing transverse energy ($\Delta\phi(\mathrm{jet}, E_{\mathrm{T}}^{\mathrm{miss}})$) suppress background arising from QCD events, where a badly measured jet leads to fake missing momentum along its trajectory. Also a cut on the ratio of $E_{\mathrm{T}}^{\mathrm{miss}}/m_{\mathrm{eff}}$ helps to reduce this kind of background, especially in events with a high center-of-mass energy of the hard subprocess.

Signal region	A	B	C	D
Target	Direct $\tilde{g}\tilde{g}$	Associated $\tilde{q}\tilde{g}$	Low-mass $\tilde{q}\tilde{\bar{q}}$	High-mass $\tilde{q}\tilde{\bar{q}}$
Leading jet p_T[GeV]	> 120	> 120	> 120	> 120
Second jet p_T [GeV]	> 40	> 40	> 40	> 40
Third jet p_T [GeV]	> 40	> 40	–	–
E_T^{miss} [GeV]	> 100	> 100	> 100	> 100
$\Delta\phi(\text{jet}, E_T^{miss})$	> 0.4	> 0.4	> 0.4	> 0.4
E_T^{miss}/m_{eff}	> 0.25	> 0.25	> 0.3	–
m_{eff} [GeV]	> 500	> 1000	> 500	–
m_{T2} [GeV]	–	–	–	> 300

Table 6.3: Signal region fiducial selections. According to [68].

6.4 Background determination

The baseline background determination was done using Monte Carlo predictions (except for the QCD background). They have then been verified in various control regions and the systematic uncertainties have also been estimated in this (semi-) data-driven way. For the QCD background, the estimation method is explicitly described in the following.

6.4.1 QCD background estimation

Due to the harsh cuts that are applied for the event selection, the QCD background is expected to be only sub-dominant (< 10 % of the overall standard model background in both channels). Therefore, its precise determination is not as crucial as for the other Standard Model backgrounds and reaching an uncertainty $O(50-100\%)$ should be sufficient. Nevertheless, the prediction needs to be reliable. It is very challenging to control this background due to the still poor theoretical description, especially for multi-jet events. Despite the cuts on $(\Delta\phi(\text{jet}, E_T^{miss}))$ and E_T^{miss}/m_{eff}, QCD events with badly measured jets still enter the signal selection. There are also heavy flavour QCD events with real missing transverse energy, which contribute.

Since events that fall into the signal region typically have a large jet multiplicity, there is good reason to doubt the predictions of the `Pythia` $2 \rightarrow 2$ simulation [6]. To gain confidence in the MC description also the predictions of other generators were compared to data in the control regions in [68], especially the multi-leg generator `Alpgen`. This study has shown, that it is sufficient to compute normalization factors (k-factors) to correct for the discrepancy between the data and the MC prediction. The prediction from MC was normalized to the observed data in control regions very similar to the signal regions.

The `Pythia` QCD Monte Carlo was split into a light flavour (LF) and a heavy flavour

[6] `Pythia` QCD Monte Carlo samples were used despite this disadvantage due to the large number of events available.

(HF) component in order to investigate if different control regions prefer certain types of QCD events. A QCD event is tagged as HF, if it contains a reconstructed jet within the defined acceptance ($p_{\mathrm{T}} > 30$ GeV, $|\eta| < 2.5$), that is matched to a b-jet on generator level. The yellow error band shown in all plots correspond to a combination of the statistical uncertainty and systematic uncertainties. The systematics included in the plots are the jet energy scale (JES) uncertainty, the jet energy resolution (JRES) and a 11% uncertainty on the integretad luminosity for the non-QCD backgrounds. Details on the JES and JRES uncertainties are explained later in this section.

Control regions

The control regions were chosen such, that they are dominated by QCD background and are in a very similar region in phase space as the signal region. In order to achieve that, all selection cuts were kept the same, besides either the $\Delta\phi(\mathrm{jet}, E_{\mathrm{T}}^{\mathrm{miss}})$ or $E_{\mathrm{T}}^{\mathrm{miss}}/m_{\mathrm{eff}}$ cut, which was inverted. The k-factor and the extrapolation are computed according to:

$$k = \frac{N_{\mathrm{Data}}^{\mathrm{CR}} - N_{\mathrm{MC\ W,Z,top}}^{\mathrm{CR}}}{N_{\mathrm{MC\ QCD}}^{\mathrm{CR}}} \qquad (6.4)$$
$$N_{\mathrm{expected}}^{\mathrm{SR}} = k\, N_{\mathrm{MC\ QCD}}^{\mathrm{SR}}$$

where $N_{\mathrm{Data}}^{\mathrm{CR}}$ is the number of observed data events in the control region, $N_{\mathrm{MC\ QCD}}^{\mathrm{CR}}$ is the number of MC predicted QCD events in the control region, $N_{\mathrm{MC\ QCD}}^{\mathrm{SR}}$ is the number of MC predicted QCD events in the signal region and $N_{\mathrm{MC\ W,Z,top}}^{\mathrm{CR}}$ is the number of MC predicted W, Z and top events in the control region which is subtracted from the data in order to minimize the sensitivity of the k-factors on the small W, Z, and top contamination.

The inverted $\Delta\phi(\mathrm{jet}, E_{\mathrm{T}}^{\mathrm{miss}})$ selection serves as the baseline control region, whereas the $E_{\mathrm{T}}^{\mathrm{miss}}/m_{\mathrm{eff}}$ control region is used as a cross check. An overall k-factor was computed from the $\Delta\phi(\mathrm{jet}, E_{\mathrm{T}}^{\mathrm{miss}})$ control region for the dijet selection - previous to the final $E_{\mathrm{T}}^{\mathrm{miss}}$ or m_{T2} cut - in order to normalize the QCD background in all plots for this chapter. The resulting scaling-factor is 1.28; it was also computed for the 3 jet selection, for which it is found to be compatible. It should be noted that it is used for illustrative purpose only. The k-factors finally used to estimate the QCD background in the four signal regions are determined independently.

Figure 6.2 and 6.3 show the m_{eff}, $E_{\mathrm{T}}^{\mathrm{miss}}$, p_{T} of the leading jet and the event transverse thrust [7] for the 2 and 3 jet selection in the $\Delta\phi(\mathrm{jet}, E_{\mathrm{T}}^{\mathrm{miss}}) < 0.4$ control region. Figure 6.2 also shows the m_{T2} distribution for that region. Even by only applying the illustrative scaling-factor of 1.28, the data and the Monte Carlo prediction agree reasonable well within errors in this control region. The agreement in the transverse thrust distribution implies, that not only the leading objects are well described, but the whole event topology. Additional plots can be found in Appendix C.2.

Individual k-factors are obtained for the four different signal regions defined by additional cuts on m_{eff} or m_{T2} (without the $E_{\mathrm{T}}^{\mathrm{miss}}/m_{\mathrm{eff}}$ requirement for the $m_{\mathrm{T2}} > 300$ GeV signal region).

[7] The thrust T provides information on the event topology and is defined as $T = \max_{\vec{n}} \frac{\sum_i |\vec{n}\cdot\vec{p_i}|}{\sum_i |\vec{p_i}|}$, where the unit vector $\vec{n}$ is the orientation of the thrust axis and $\vec{p_i}$ are the momenta of the hadronic final state particles. The transverse thrust is calculated in the plane perpendicular to the beam axis.

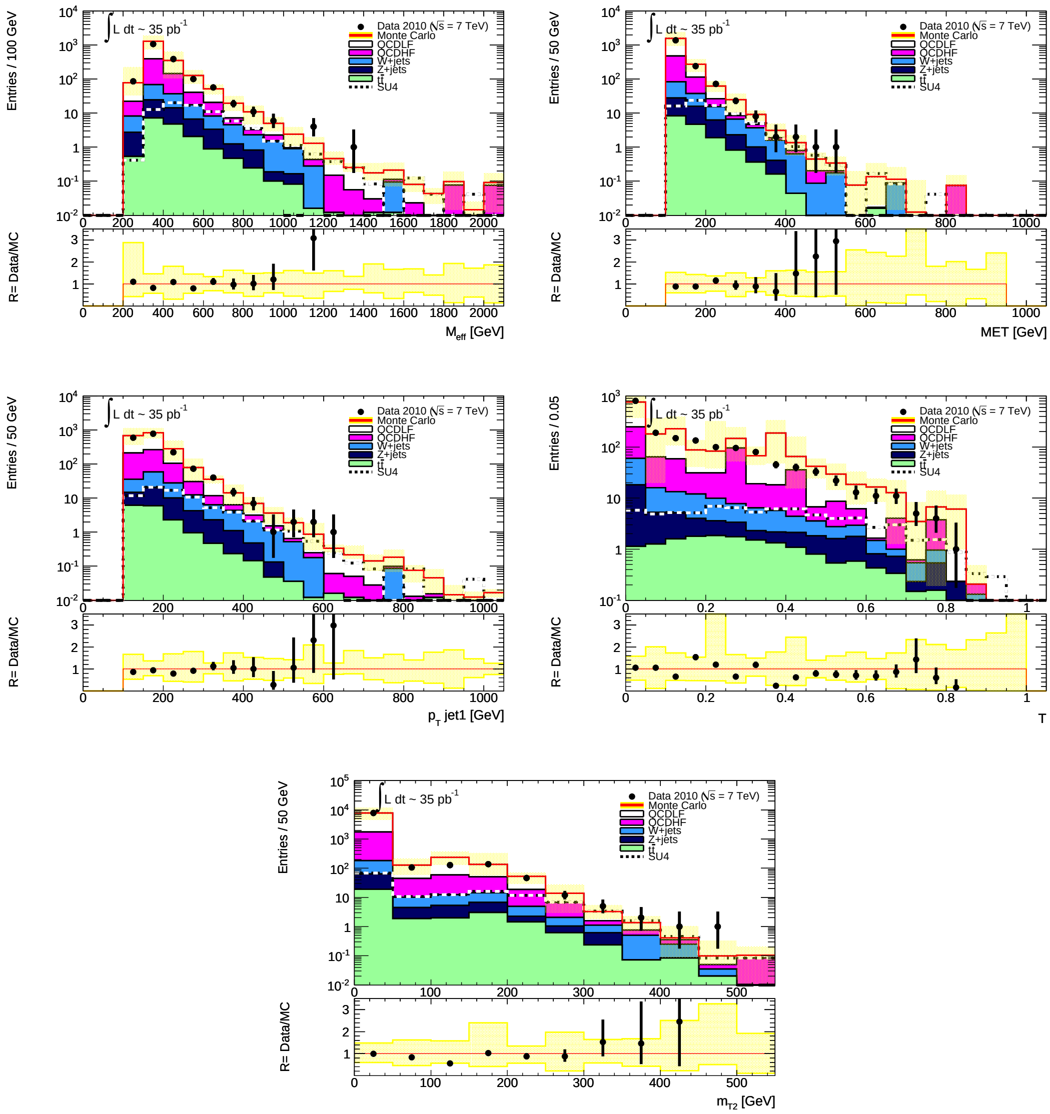

Figure 6.2: Effective mass m_{eff}, missing transverse energy $E_{\text{T}}^{\text{miss}}$, transverse momentum p_{T} of the leading jet, event transverse thrust T and stransverse mass m_{T2} after the inverted $\Delta\phi(\text{jet}, E_{\text{T}}^{\text{miss}})$ cut in the 2 jet channel.

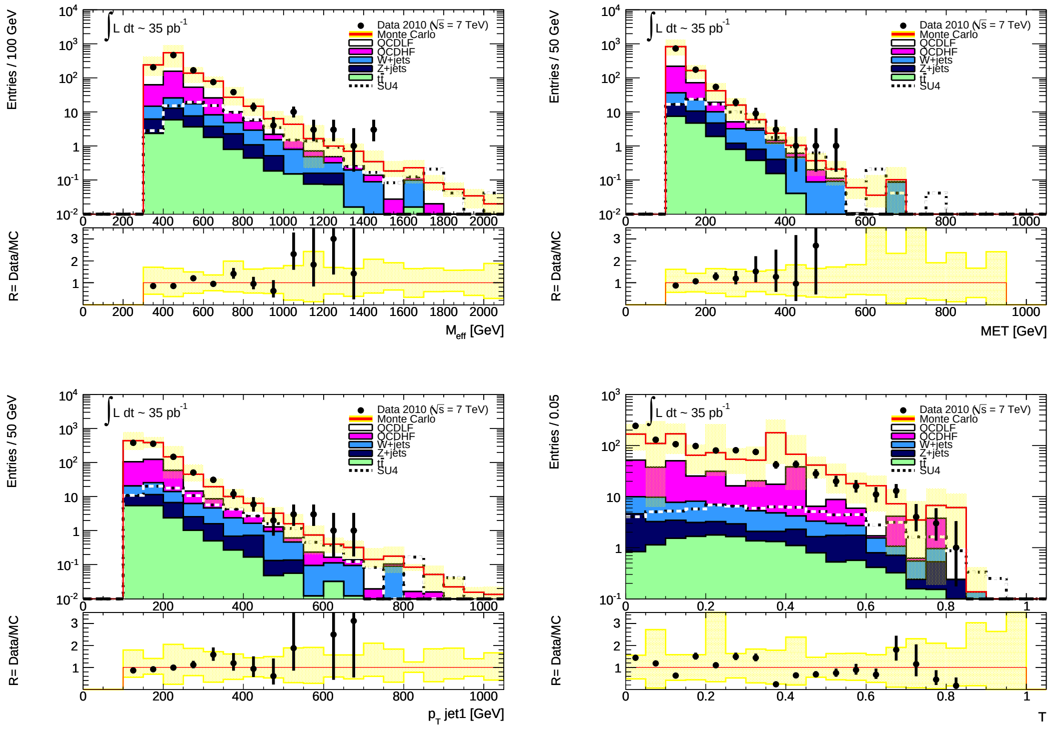

Figure 6.3: Effective mass m_{eff}, missing transverse energy $E_{\mathrm{T}}^{\mathrm{miss}}$, transverse momentum p_{T} of the leading jet and event transverse thrust T after the inverted $\Delta\phi(\mathrm{jet}, E_{\mathrm{T}}^{\mathrm{miss}})$ cut in the 3 jet channel.

	2 jet		3 jet	
	$m_{\text{eff}} > 500$ GeV	$m_{\text{T2}} > 300$ GeV	$m_{\text{eff}} > 500$ GeV	$m_{\text{eff}} > 1000$ GeV
top	4	0.4	7	0.3
Z	9	0.4	9	0.2
W	23	1.1	21	1.5
QCD HF	32	0.7	50	1.0
QCD LF	111	1.9	137	4.3
MC total	179	4.5	224	7.3
data	199	9	318	20
$k_{\Delta\phi}$	1.14 ± 0.14	2.7 ± 1.2	1.51 ± 0.16	3.4 ± 0.9
$N^{\text{SR}}_{\text{expected}}$	7 ± 4	0.6 ± 0.4	9 ± 5	0.2 ± 0.2

Table 6.4: Background composition in the control region with inverted $\Delta\phi(\text{jet}, E_{\text{T}}^{\text{miss}})$ cut and the resulting individual k-factors together with the number of expected QCD events for the signal regions defined by cuts on m_{eff} or m_{T2} for an integrated luminosity of $35\,\text{pb}^{-1}$. The uncertainty quoted for the k-factors and the signal region QCD expectations are statistical uncertainties only.

Table 6.4 summarizes the contributions from different Monte Carlo processes and from data as well as the individual k-factors in the control regions. Also shown are the resulting QCD background estimations in the signal region.

The alternative control region is defined by reversing the $E_{\text{T}}^{\text{miss}}/m_{\text{eff}}$ cut. This observable is expected to have higher values for events with real $E_{\text{T}}^{\text{miss}}$ like gauge boson production or the expected SUSY signal. For QCD background it is expected to have lower values. Therefore, selecting events with $E_{\text{T}}^{\text{miss}}/m_{\text{eff}} < 0.25(0.3)$ populates the QCD background. Figure 6.4 and 6.5 show the m_{eff}, $E_{\text{T}}^{\text{miss}}$, p_{T} of the leading jet and the event transverse thrust for the 2 and 3 jet selection in the $E_{\text{T}}^{\text{miss}}/m_{\text{eff}} < 0.25(0.3)$ control region. Also in this region, using the illustrative scaling factor of 1.28, good agreement is found between data and Monte Carlo prediction. Additional plots can be found in Appendix C.2, too.

The individual k-factors and the QCD background prediction in the signal region are summarized in Table 6.5 for this control region.

The fraction of the heavy flavour QCD component with respect to the light flavour QCD component is in both control regions ($E_{\text{T}}^{\text{miss}}/m_{\text{eff}}$ and $\Delta\phi(\text{jet}, E_{\text{T}}^{\text{miss}})$) similar and found to be $\sim 30\%$. So there is no bias introduced when switching the control region.

The individual k-factors for the two control regions are compared to each other graphically in Figure 6.6 as a function of the cut on m_{eff}. Within the statistical uncertainties there is no dependence on the m_{eff} cut value. Both control regions provide consistent results [8]. The figure also shows in addition to the final signal regions the resulting k-factors without the m_{eff} cut and an additional high m_{eff} selection for the 2 jet channel.

[8] Only the last point in Figure 6.6 corresponding to $m_{\text{eff}} > 1000$ GeV cut for the 3 jet channel has a higher value than the other points. This can be traced to a fluctuation in the 3-jet 1000 GeV $< m_{\text{eff}} <$ 1100 GeV bin in Figure 6.3.

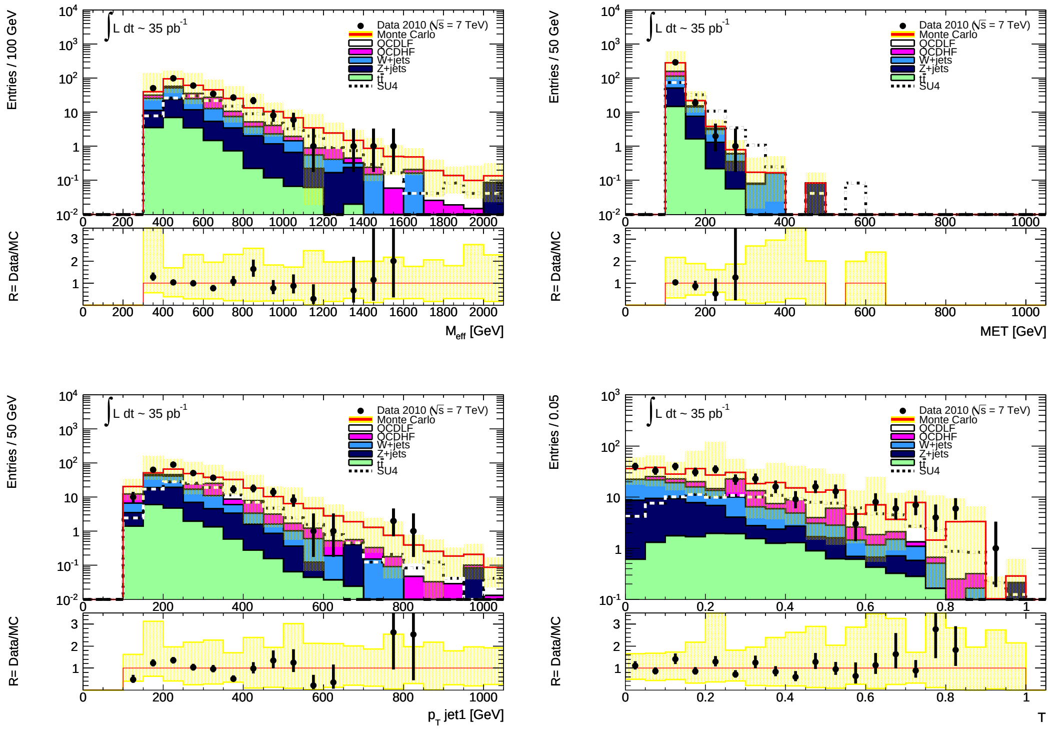

Figure 6.4: Effective mass m_{eff}, missing transverse energy $E_{\mathrm{T}}^{\mathrm{miss}}$, transverse momentum p_{T} of the leading jet and event transverse thrust T after the inverted $E_{\mathrm{T}}^{\mathrm{miss}}/m_{\mathrm{eff}}$ cut in the 2 jet channel.

	2-jet	3-jet	
	$m_{\mathrm{eff}} > 500$ GeV	$m_{\mathrm{eff}} > 500$ GeV	$m_{\mathrm{eff}} > 1000$ GeV
top	6	10	0.3
Z	19	12	0.8
W	29	22	1.7
QCD HF	25	23	2.8
QCD LF	67	70	17
MC total	146	137	23
data	163	162	30
k_R	1.18 ± 0.19	1.3 ± 0.2	1.4 ± 0.3
$N_{\mathrm{expected}}^{\mathrm{SR}}$	7 ± 4	7 ± 4	0.10 ± 0.08

Table 6.5: Background composition in the control region with inverted $E_{\mathrm{T}}^{\mathrm{miss}}/m_{\mathrm{eff}}$ cut for the signal regions in which the final selection is defined by cuts on m_{eff}. Also included are the resulting individual k-factors together with the number of expected QCD events for the signal regions defined by cuts in m_{eff} for an integrated luminosity of $35\,\mathrm{pb}^{-1}$. The uncertainties quoted for the k-factors and the signal region QCD expectations are statistical uncertainties only.

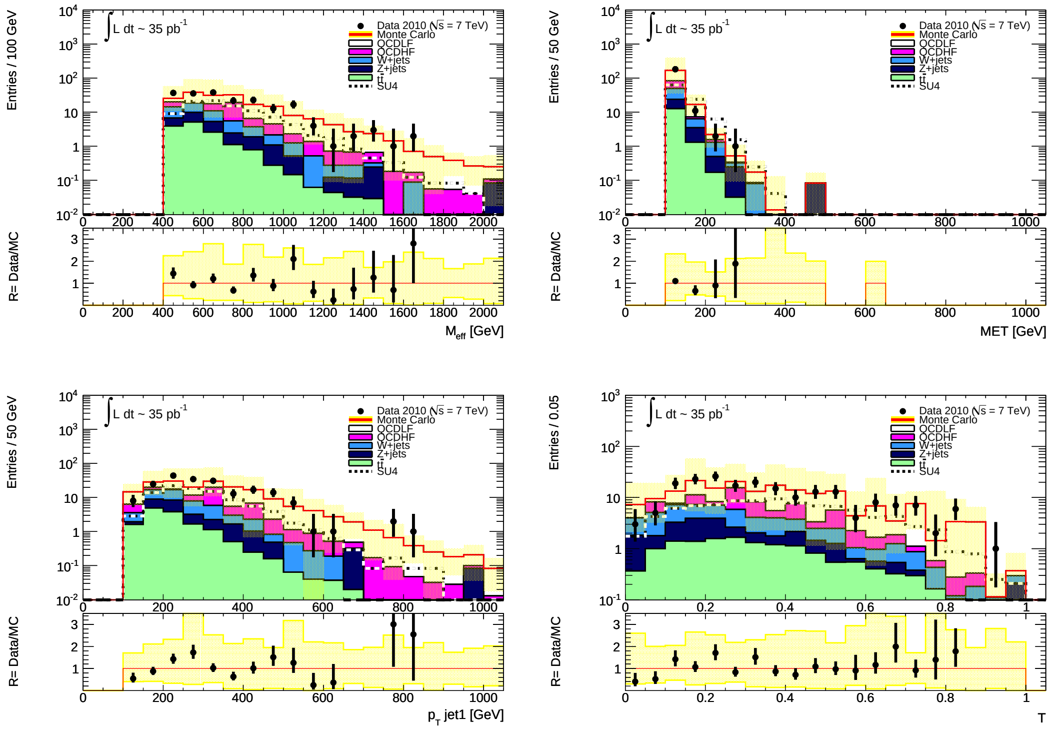

Figure 6.5: Effective mass m_{eff}, missing transverse energy $E_{\mathrm{T}}^{\mathrm{miss}}$, transverse momentum p_{T} of the leading jet and event transverse thrust T after the inverted $E_{\mathrm{T}}^{\mathrm{miss}}/m_{\mathrm{eff}}$ cut in the 3 jet channel.

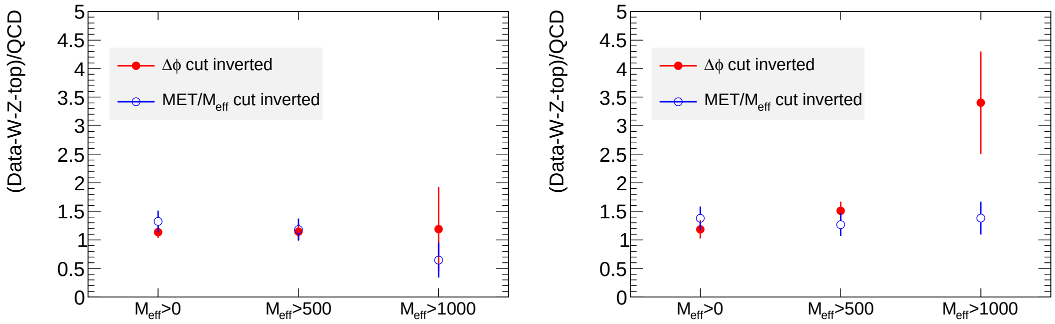

Figure 6.6: Comparison of the k-factors obtained from the control region with inverted $\Delta\phi(\mathrm{jet}, E_{\mathrm{T}}^{\mathrm{miss}})$ cut and from the control region with inverted $E_{\mathrm{T}}^{\mathrm{miss}}/m_{\mathrm{eff}}$ cut for the 2-jet (left) and 3-jet (right) channel.

Alternative method

As a cross check and independent estimation of the QCD background a fully data driven method was applied [68]. The method is based on turning low $E_{\mathrm{T}}^{\mathrm{miss}}$ multijet events in data into high $E_{\mathrm{T}}^{\mathrm{miss}}$ events using a smearing method, which consists of five steps [68]:

(1) Selection of low-$E_{\mathrm{T}}^{\mathrm{miss}}$ seed events which are used in step (5).

(2) Measurement of the Gaussian component of the jet response function.

(3) Measurement of the non-Gaussian component of the jet response function.

(4) Construction of the full smearing function. Perform a 'normalization closure test' to validate the construction of the smearing function.

(5) Jet smearing of the seed events from (1) using the smearing function to obtain estimated distributions of key variables in the SUSY signal region.

The result gives an independent estimate of the amount of QCD events expected in the signal regions and systematics (c.f. Table 6.6). They are in agreement with the results, which were obtained by using the k-factors determined in control regions [68].

Overall estimation

The sources of systematic uncertainties, which were taken into account for the final QCD background estimation [68], are explained in the following. Both theoretical uncertainties, which are due to the incomplete knowledge of the underlying physics, and experimental uncertainties, which arise from the incomplete knowledge of the detector performance, are considered. The systematic effect under study was varied in the MC and with this, the number of expected QCD events was estimated. The difference between that and the nominal MC is then taken as the systematic uncertainty.

Generator systematics were estimated by varying the PDFs used in `Pythia` and by comparing to the results of `Herwig++`.

Heavy flavour systematics were simulated by doubling the weight of events with a b-jet on generator level.

Non QCD background uncertainty was estimated conservatively to be 40%. This is by far more than the numbers achieved by the data-driven methods, which were used for these background, so the considered 40% are indeed conservative.

Jet energy scale (JES) uncertainty and jet resolution (JRES) are taken into account according to the recommendations in [90] and [91], respectively. The JES uncertainty varies as a function of p_{T} and η between 10% at 20 GeV and about 8% at 100 GeV. For the JRES a Gaussian shape is used as an estimate for the distribution with a width of 14% for jets with

	m_{eff}> 500 GeV (2j)	$m_{\text{T2}} > 300$ GeV (2j)
Pythia MC	5.8 ±3.1 (stat) ±6.6 (sys)	0.2 ±0.1 (stat) ±0.1 (sys)
Method QSF ($\Delta\phi$) Method QSF ($E_{\text{T}}^{\text{miss}}/m_{\text{eff}}$)	6.6 ± 3.6 (stat) ± 3.1 (sys) 6.9 ± 3.8 (stat) ± 2.5 (sys)	0.6 ± 0.4 (stat) ± 0.4 (sys) N/A
Method DD	4.6 ±0.1 (stat.) ±0.1 (norm.) ±0.6 (gaus.) ±0.2 (tail-norm.) ±6.5 (tail-sys.)	0.51 ±0.09 (stat.) ±0.01 (norm.) ±0.03 (gaus.) ±0.01 (tail-norm.) ±0.44 (tail-sys.)
Baseline (RC)	6.6 +7.7 (comb.) −6.6 (comb.)	0.6 +0.7 (comb.) −0.6 (comb.)
	m_{eff}> 500 GeV (3j)	m_{eff}> 1000 GeV (3j)
Pythia MC	5.8 ±3.1 (stat) ±3.5 (sys)	0.1 ±0.1 (stat) ±0.1 (sys)
Method QSF ($\Delta\phi$) Method QSF ($E_{\text{T}}^{\text{miss}}/m_{\text{eff}}$)	8.8 ± 4.8 (stat) ± 2.2 (sys) 7.4 ± 4.1 (stat) ± 4.5 (sys)	0.2 ± 0.2 (stat) ± 0.1 (sys) 0.10 ± 0.08 (stat) ± 0.05 (sys)
Method DD	9.4 ±0.2 (stat.) ±0.2 (norm.) ±1.1 (gaus.) ±0.6 (tail-norm.) ±7.1 (tail-sys.)	0.11 ±0.02 (stat.) ±0.00 (norm.) ±0.01 (gaus.) ±0.00 (tail-norm.) ±0.12 (tail-sys.)
Baseline (RC)	9 +10 (comb.) −9 (comb.)	0.2 +0.4 (comb.) −0.2 (comb.)

Table 6.6: The numbers of QCD events predicted for the different signal regions for the `Pythia` Monte Carlo and the different data-driven methods. The numbers for `Pythia` MC are normalized to the luminosity without using a scaling factor. The abbreviation QSF stands for QCD scale factor , DD stands for the fully data driven method. RC stands for the Ratio Combination method (inc. data driven k-factor) . The Ratio Combination method includes more uncertainties than the other methods and is used as baseline prediction. Taken from [68].

$p_{\text{T}} > 20\,\text{GeV}$ and $|\eta| < 2.8$. Both effects are propagated through to the missing transverse energy by recalculating $E_{\text{T}}^{\text{miss}}$ according to: $E_{\text{T}}^{\text{miss}}(\text{new}) = E_{\text{T}}^{\text{miss}}(\text{old}) + \sum p_{\text{T}}(\text{old}) - \sum p_{\text{T}}(\text{new})$.

For the final QCD background prediction all methods are considered, all of which are listed in Table 6.6. The QCD scaling factor method in the $\Delta\phi(\text{jet}, E_{\text{T}}^{\text{miss}})$ control region was used to determine the central value of the final prediction. While for the scaling method only the JES and JRES is taken into account for the systematics, the final prediction (labeled with **(RC)**, c.f. Table 6.6) considers all systematic uncertainties mentioned above [68].

The predictions from each method all give consistent results, which demonstrates the robustness of the estimation.

	$m_{\rm eff}$> 500 GeV (2j)		m_{T2} > 300 GeV (2j)	
Alpgen W+jets	49.6 ± 2.1 (stat)	$^{+9.3}_{-8.1}$ (JES) ±0.8 (JER) ±5.5 (lumi) ±9.4 (CR stat.) ±5.0 (lep eff.)	4.4 ± 0.6 (stat)	$^{+1.0}_{-0.7}$ (JES) ±0.1 (JER) ±0.2 (lumi) ±3.1 (CR stat.+extrapol.) ±0.4 (lep eff.)

	$m_{\rm eff}$ > 500 GeV (3j)		$m_{\rm eff}$ > 1000 GeV (3j)	
Alpgen W+jets	34.7 ± 1.7 (stat)	$^{+6.8}_{-6.5}$ (JES) ±2.2 (JER) ±3.8 (lumi) ±7.3 (CR stat.) ±3.5 (lep eff.)	1.1 ± 0.3 (stat)	$^{+0.2}_{-0.3}$ (JES) ±0.1 (JER) ±0.1 (lumi) ±0.6 (CR stat.+extrapol.) ±0.1 (lep eff.)

Table 6.7: Numbers of W+jets events predicted in the different signal regions from `Alpgen` Monte Carlo simulations for 35 pb^{-1}. Errors shown are from MC statistics (stat.), Jet Energy Scale and luminosity systematics that are correlated in all samples, and various other uncorrelated errors (uncorr.) that are added in quadrature to provide the final error on the SM background estimate. Taken from [68].

6.4.2 Estimation of other backgrounds

Other Standard Model backgrounds were estimated in [68] using various different approaches, summarized below.

Vector boson plus jets

For the W and Z + jets background the following methods were applied:

- **Monte Carlo based:** The background shape and rate is taken from the MC prediction. For this, it has to be assumed that the MC is sufficiently precise. The assumption is encouraged by the amount of input from theory side, that went into the generators, and the constraints from past experiments, that are implemented.

- **Mixed data and MC based:** The background in the signal region is extrapolated from data control samples using Monte Carlo. Doing that, parts of the uncertainties cancel but one pays the price of the central value being influenced by fluctuations in the control sample (where the statistics is low).

- **Event based correction on data:** For this quasi data-driven approach the shape and the rate of the background is taken from data control samples. The correction factors for acceptance and ID efficiency are taken from Monte Carlo.

The `Alpgen` Monte Carlo was used as baseline estimation, cross checked via the other methods and enhanced by systematic uncertainty estimations (for details c.f. [68]). The results are summarized in Table 6.7 and 6.8.

	m_{eff}> 500 GeV (2j)		m_{T2} > 300 GeV (2j)	
Alpgen Z+jets	52.2 ± 3.1 (stat)	$^{+11.4}_{-9.4}$ (JES) ± 2.4 (JER) ± 5.7 (lumi) ± 15.6 (accept.) ± 14.6 (CR stat.)	4.1 ± 0.8 (stat)	$^{+1.7}_{-0.8}$ (JES) ± 0.2 (JER) ± 0.5 (lumi) ± 1.2 (accept.) ± 2.5 (CR stat.+extrapol.)
	m_{eff} > 500 GeV (3j)		m_{eff} > 1000 GeV (3j)	
Alpgen Z+jets	27.4 ± 2.0 (stat)	$^{+7.2}_{-5.0}$ (JES) ± 0.8 (JER) ± 3.0 (lumi) ± 8.2 (accept.) ± 9.0 (CR stat.)	0.84 ± 0.3 (stat)	$^{+0.3}_{-0.}$ (JES) ± 0.003 (JER) ± 0.09 (lumi) ± 0.3 (accept.) ± 0.5 (CR stat.+extrapol.)

Table 6.8: Numbers of Z+jets events predicted in the different signal regions from `Alpgen` Monte Carlo simulations for 35 pb^{-1}. Errors shown are from MC statistics (stat.), Jet Energy Scale and luminosity systematics that are correlated in all samples, and various other uncorrelated errors (uncorr.) that are added in quadrature to provide the final error on the SM background estimate. Taken from [68].

Top

The `MC@NLO` prediction for the top background has been cross checked in [68] with the predictions from the `POWHEG` generator [92] and semi data-driven approaches. The central values of the estimation are taken from `MC@NLO` taking into account systematic uncertainties from variation of the jet energy scale, jet energy resolution and the uncertainty on the integrated luminosity. Table 6.9 summarizes the results.

6.5 Results and interpretation

The observed data was compared to the Standard Model (SM) background expectation in all four signal regions, where all selection cuts are applied besides the final m_{eff} or m_{T2} cut. Figure 6.7 shows the m_{eff} and m_{T2} distributions for the dijet channel and Figure 6.8 shows the m_{eff} distribution for the three-jet selection. The SM background was taken from the normalized (factor 1.28) `Pythia` Monte Carlo and from MC predictions for W, Z and top. The yellow error band corresponds to the combination of the statistical error and the systematic uncertainties from the jet energy scale, the jet energy resolution and the luminosity uncertainty added in quadrature. The error bars associated to the data points are the Poisson coverage interval corresponding to the number of events in each bin.

Good agreement was found between the data and the SM expectation for both of the channels. There is a threshold effect from the p_{t} and $E_{\text{T}}^{\text{miss}}$ cuts showing in the first bin. But even that is well within the error band and furthermore not relevant for the final selection. Table 6.10 shows the comparison of the predicted and observed number of events in the four signal regions. The SM prediction agrees with the observed data within the errors.

	m_{eff}> 500 GeV (2j)		$m_{\text{T2}} > 300$ GeV (2j)	
MC@NLO $t\bar{t}$	8.8 ± 0.2 (stat)	$^{+1.4}_{-2.1}$ (JES) $\pm$0.3 (JER) $\pm$1.0 (lumi)	0.8 ± 0.06 (stat)	$^{+0.2}_{-0.2}$ (JES) $\pm$0.04 (JER) $\pm$0.09 (lumi)
MC@NLO single top	1.0 ± 0.2 (stat)	$^{+0.5}_{-0.2}$ (JES) $\pm$0.02 (JER) $\pm$0.1 (lumi)	0.1 ± 0.06 (stat)	$^{+0.}_{-0.07}$ (JES) $\pm$0. (JER) $\pm$0.01 (lumi)
	$m_{\text{eff}} > 500$ GeV (3j)		$m_{\text{eff}} > 1000$ GeV (3j)	
MC@NLO $t\bar{t}$	15.8 ± 0.3 (stat)	$^{+3.2}_{-3.3}$ (JES) $\pm$0.6 (JER) $\pm$1.7 (lumi)	0.2 ± 0.06 (stat)	$^{+0.05}_{-0.1}$ (JES) $\pm$0.02 (JER) $\pm$0.02 (lumi)
MC@NLO single top	1.0 ± 0.2 (stat)	$^{+0.4}_{-0.3}$ (JES) $\pm$0.05 (JER) $\pm$0.1 (lumi)	0.1 ± 0.05 (stat)	$^{+0.03}_{-0.07}$ (JES) $\pm$0.03 (JER) $\pm$0.01 (lumi)

Table 6.9: Number of $t\bar{t}$ and single top-quark events as predicted by the MC@NLO generator, together with the associated uncertainties, for each of the four signal regions. Taken from [68].

	$m_{\text{eff}} > 500$ GeV (2 jet channel)		$m_{\text{T2}} > 300$ GeV (2 jet channel)	
Total SM background	118 ± 3.7(stat)	$^{+32.1}_{-23.7}$ (JES) $\pm$13.0(lumi) $\pm$25.0(uncorr.)	10.0 ± 1.1(stat)	$^{+4.0}_{-2.0}$ (JES) $\pm$1.1(lumi) $\pm$4.2(uncorr.)
Data	87		11	
	$m_{\text{eff}} > 500$ GeV (3 jet channel)		$m_{\text{eff}} > 1000$ GeV (3 jet channel)	
Total SM background	$87,8 \pm 2.6$(stat)	$^{+25.8}_{-18.7}$ (JES) $\pm$9.7(lumi) $\pm$18.3(uncorr.)	2.5 ± 0.5(stat)	$^{+1.0}_{-0.6}$ (JES) $\pm$0.3(lumi) $\pm$1.0(uncorr.)
Data	66		2	

Table 6.10: Predicted number of SM background events and observed data events in the signal regions. Taken from [68].

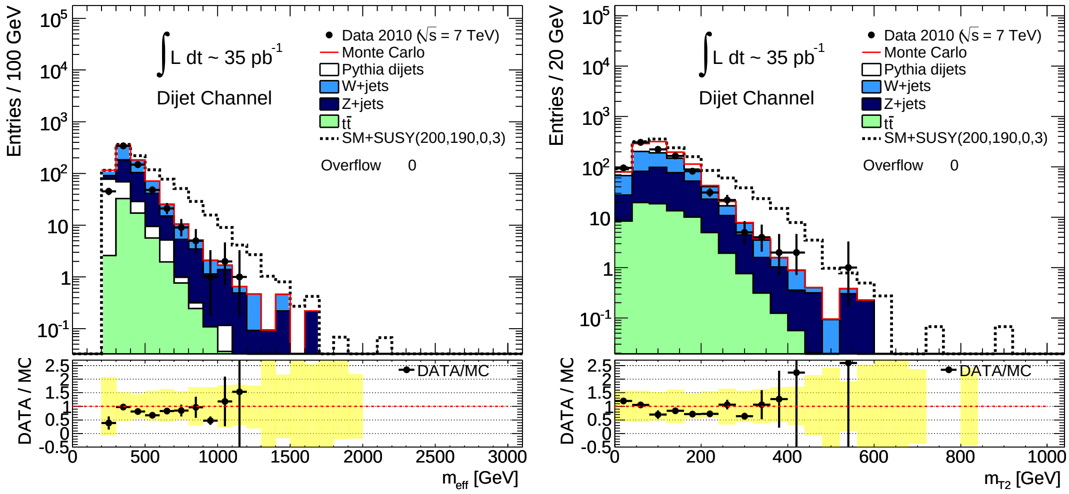

Figure 6.7: Distributions of the effective mass m_{eff} (left)and stransverse mass m_{T2} (right) for events in the dijet channel. The following cuts have been applied: missing transverse momentum $E_{\text{T}}^{\text{miss}} > 100$ GeV, azimuthal difference $\Delta\phi(\text{jet}_{1,2,3}, E_{\text{T}}^{\text{miss}}) > 0.4$. In the left figure it is also required that the ratio of missing transverse momentum to effective mass $E_{\text{T}}^{\text{miss}}/m_{\text{eff}} > 0.3$. The mSUGRA SUSY point shown for reference is $m_0 = 200$, $m_{1/2} = 190$, $A_0 = 0$, $\tan\beta = 3$, $\mu > 0$. Taken from [68].

6.5.1 Limit setting procedure

The method used for the limit calculation is described in detail in [70]. All models of new physics are excluded, that will produce more events in the signal regions than the calculated upper limits, taking into account the uncertainties on the signal and the background.

The method is based on a profile likelihood ratio test statistic following a fully frequentist approach. The likelihood function is a product of a Poisson distribution modeling the statistical uncertainty in the signal region and additional distributions accounting for the systematic uncertainties. Systematic uncertainties are parameterized via nuisance parameters, which are modeled with Gaussian probability density functions. The uncertainties on the luminosity and the jet energy scale are treated as 100% correlated in signal and background, while all other uncertainties - the jet and electron resolution, the uncertainties on the electron energy scale, the electron selection efficiency and the Monte Carlo uncertainties [68] - are treated as uncorrelated.

The final 95% confidence level is calculated using toys sampled from the test statistic described above. By applying only the analysis with the best expected exclusion limit for each signal grid point, the combined limits are avoiding the so-called 'look-elsewhere' effect [9].

[9]Looking for a signal at different locations (other bins of the same histogram or other spectra) has to be taken into account, when computing the significance. More details can be found e.g. in [93]

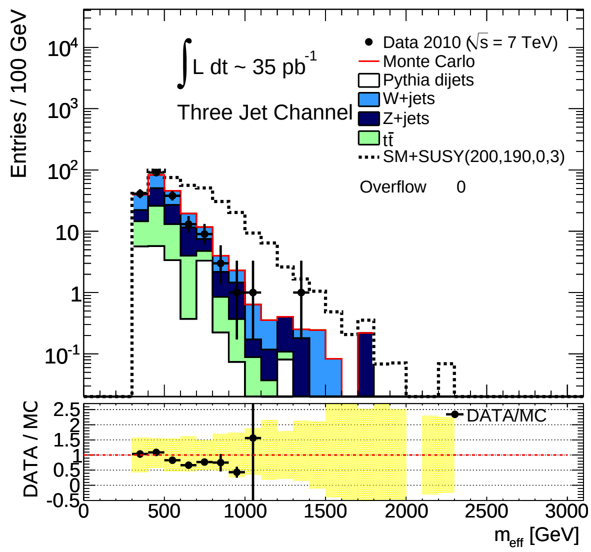

Figure 6.8: Distribution of the effective mass m_{eff} for events in the three-jet channel. The following cuts have been applied: missing transverse momentum $E_{\text{T}}^{\text{miss}} > 100$ GeV, azimuthal difference $\Delta\phi(\text{jet}_{1,2,3}, E_{\text{T}}^{\text{miss}}) > 0.4$ and the ratio of missing transverse momentum to effective mass $E_{\text{T}}^{\text{miss}}/m_{\text{eff}} > 0.25$. The mSUGRA SUSY point shown for reference is $m_0 = 200$, $m_{1/2} = 190$, $A_0 = 0$, $\tan\beta = 3$, $\mu > 0$. Taken from [68].

6.5.2 Exclusion limits

The combined exclusion limits from all four signal regions are displayed in Figure 6.9 for the mSUGRA and squark-gluino grid. For the later one the 95% exclusion reaches 870 GeV in the restricted case with $m_{\tilde{q}} = m_{\tilde{g}}$, while for the mSUGRA model the exclusion for that restricted case exceeds 775 GeV [69]. The exclusion limits for both models are considerably improved with respect to previous experiments.

6.6 Split SUSY prospects in the multijet channels

Since the jets in the Split SUSY model would be due to initial state radiation, the prospects in mutlijet channels should be worse than in a monojet channel. But as the object definitions, the limit setting procedure etc. are different in the multi- and monojet channel (c.f. next chapter), it is difficult to generally quantify this. As a first attempt, the significance [10] is calculated for one gluino mass in the four signal regions of the multijet channels (Table 6.11). These numbers are then compared to the ones obtained in the monojet channel (c.f. next chapter).

[10]The significance is defined as $S/\sqrt{B}$, where S is the number of signal and B the number of background events. This is a very simple figure of merit taking into account only statistical errors.

region	2jet, $m_{\text{eff}} > 500$ GeV	2jet $m_{\text{T2}} > 300$ GeV
$S/\sqrt{B}$	3.2	2.3
region	3jet $m_{\text{eff}} > 500$ GeV	3jet $m_{\text{eff}} > 1000$ GeV
$S/\sqrt{B}$	1.5	1.8

Table 6.11: Significance for a R-hadron signal with $m_{\tilde{g}} = 300$ GeV in the four multijet signal regions.

6.7 Summary

For the searches for squarks and gluinos in the channels with two or three jets, a semi-data-driven QCD background estimation method was developed using normalization factors from control regions. Together with cutflow and distribution comparisons in the signal regions, this contributed to the final exclusion limits presented in [68, 69] and summarized here.

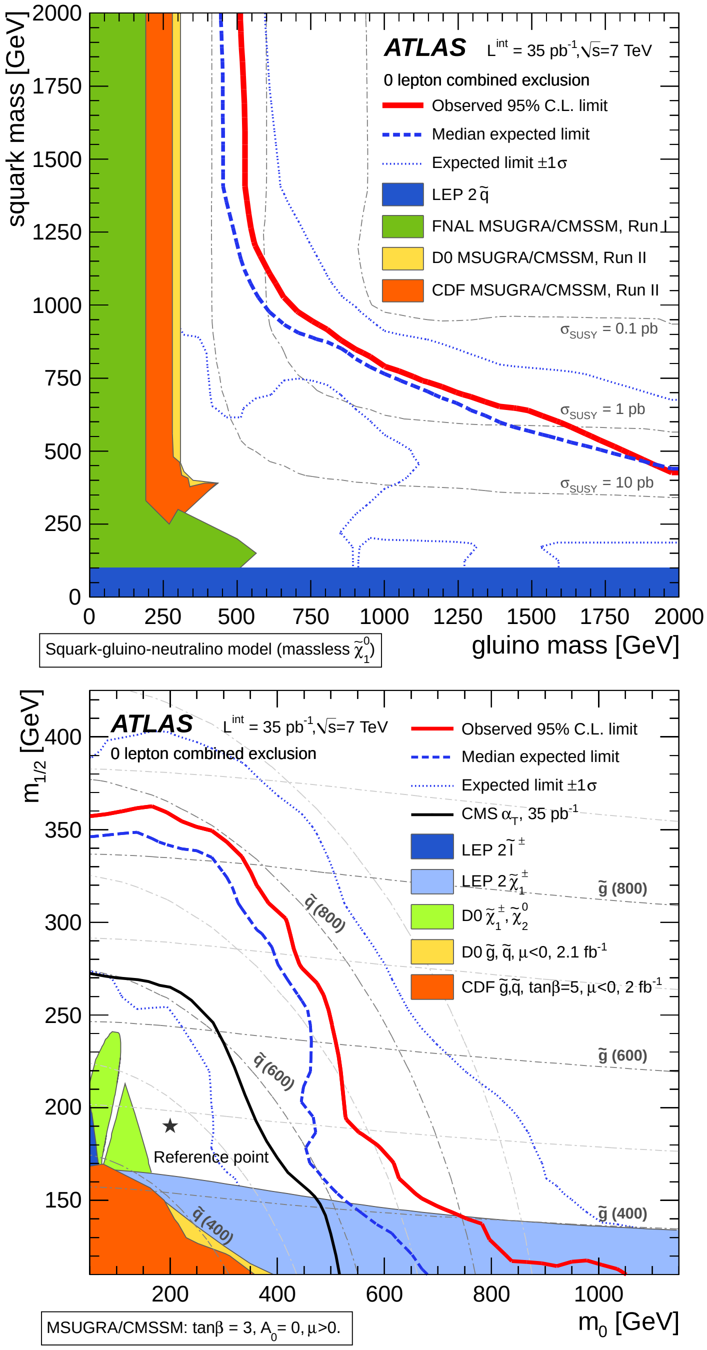

Figure 6.9: Expected and observed limits with the combined exclusion from all four signal regions for the squark-gluino-grid (higher plot) and the mSUGRA-grid (lower plot). The blue dashed line corresponds to the expected 95% CL limit, the dotted blue lines to $\pm 1\sigma$ 95% CL limits respectively. The red line is the observed limit. Tevatron limits on $m_{\tilde{q}}$ and $m_{\tilde{g}}$ are marked for searches in the specific context of mSUGRA, with $\tan\beta = 3$, $A_0 = 0$ and $\mu < 0$, and are also shown for illustration. The reference mSUGRA point ($m_0 = 200$, $m_{1/2} = 190$) plotted in the signal distribution histograms is indicated by a star. Taken from [68].

Chapter 7

Searches in the monojet channel

7.1 Introduction

Originally being part of [68], it was decided to merge the efforts of the SUSY and the EXOTICS groups for the monojet channel searches. This is the reason why the object definition, the cleaning cuts and also some background estimation methods differ from the definitions, that were used for the zero lepton SUSY searches summarized in Chapter 6. The event selection has not been optimized for a specific signal model and the analysis was performed “blind” in the sense that only after a complete study of the background, the data in the signal regions were looked at.

The joint effort is being written up in an ATLAS Internal note [94] aiming for a public paper. For this effort, a data driven QCD background estimation method was developed in collaboration with J. Abdallah, which differs from the one used in the SUSY zero lepton searches, and will be discussed in detail here, while other background estimations are quoted. The exclusion limits for the Split SUSY model were computed and will be also discussed in detail. Section 7.2 briefly introduces the datasets and MC samples which were used in the study, while section 7.3 and 7.4 summarize the object definition and event selection criteria. Section 7.5 summarizes the studies on the various backgrounds, that were done in [94]. The QCD background estimation is discussed in detail in Section 7.5.3. The experimental results and their theoretical interpretation are accompanied by the description of the limit setting procedure.

7.2 Data sets and Monte Carlo samples

The same data format as in Chapter 6 has been used, i.e. D3PDs derived from AODs reconstructed in Athena release 15 via the SUSYD3PDMaker package.

7.2.1 Data sets

Like in Chapter 6, data collected during the 2010 data taking period was used for this analysis partitioned into the run periods A to I (L1Calo or JetTauEtmiss stream, respectively). After the Good Run List (GRL) selection and with an improved luminosity estimate in place, this corresponds to 33.4 ± 3.2 pb^{-1}.

7.2.2 Monte Carlo samples

The same official `mc09` Monte Carlo samples as in Chapter 6, reconstructed with the `GEANT4` [43] based detector simulation, were used for the Standard Model background. A detailed list can be found in Appendix C.1. The signal Monte Carlo is described in Section 7.6.

Different to the multi-jet searches, though, is the modeling and treatment of pileup. For this study dedicated pileup samples were used for the electroweak and the top background. The Monte Carlo samples are overlaid with minimum bias events. In order to model the data correctly, the samples have to be reweighted according to the number of reconstructed vertices in every event. The reweighting factors are listed in Table 7.1.

Number of vertices	1	2	3	4	5	6	7	>7
Factor	1.72	1.096	0.82	0.689	0.595	0.61	0.53	0.838

Table 7.1: Reweighting factors as a function of the number of reconstructed vertices. Taken from [94]

7.3 Object definitions

Jets are defined in the same way as in the multi-jet analysis (c.f. Chapter 6) using topological clusters [85] as input for the anti-k_t algorithm [84]. The distance parameter was again chosen to be $R = 0.4$ and the jets are calibrated to the jet energy scale via the *Jet Numerical Inversion Correction* mentioned before.

For the event cleaning, jets with $p_T > 20$ GeV and no $|\eta|$ constraint are considered, while for the event selection the requirement on the transverse momentum is tightened to $p_T > 30$ GeV and a cut on $|\eta| < 4.5$ is imposed.

Electrons have to pass the *Robust Medium quality requirements* [50, 86] and are constrained by $p_T > 20$ GeV and $|\eta^{clust}| < 2.47$.

Muons are required to be combined, i.e. having a matched Inner Detector and Muon Spectrometer track via the *STACO* algorithm [51], and should satisfy $p_T > 10$ GeV and $|\eta| < 2.4$. By requiring the energy in a cone of radius 0.2 to be less than 1.8 GeV, the muons are guaranteed to be isolated.

Missing transverse energy is calculated based on calorimeter information using the *MET_TopoLocHad* definition. The inputs are topological clusters [85] calibrated at the local energy scale in the range $|\eta| < 4.5$.

In contrast to the multi-jet analysis, there is no special treatment for overlapping objects.

7.4 Event selection

7.4.1 Preselection

Before any kinematic cuts defining the signal regions, the following preselections are imposed:

(P1) SUSY Good Run List (GRL)

(P2) `EF_xe40_noMu` trigger

(P3) At least one good vertex with five or more associated tracks

(P4) Cleaning Cuts

(P5) Veto events with one or more electron(s) or muon(s)

Trigger

The `EF_xe40_noMu` trigger is the first available unprescaled $E_{\mathrm{T}}^{\mathrm{miss}}$ trigger. The efficiency was studied in detail in [94] and was found to be fully efficient above $E_{\mathrm{T}}^{\mathrm{miss}} > 120$ GeV.

Event cleaning

Since the monojet channel is especially susceptible to non-collision background, the tightest cleaning cuts are used, that are proposed by the Jet$E_{\mathrm{T}}^{\mathrm{miss}}$group labeled "Tight+" (c.f. Table 7.2). In addition, the event is dropped, if the leading jet has a charge fraction of $f_{\mathrm{ch}} \leq 0.02$ with $p_{\mathrm{T}} > 120$ GeV. This is done in order to be even more protected against cosmic ray and beam halo events.

Lepton veto

The lepton veto rejects isolated muons and electrons according to the object definitions described above. Detailed studies were done in [94] concerning the rejection power and uncertainties. Good agreement between data and Monte Carlo predictions were found, i.e. the differences are below 3%. Table 7.3 shows the rejection power of the lepton veto for different electroweak backgrounds. As expected, the veto works best for a clear muon signature, whereas for $Z \to \nu\nu$ it is almost completely inefficient.

7.4.2 Signal regions

Two signal regions were defined covering a great variety of possible new physics models.

LowPt region

The low kinematic region is defined by a central jet and $E_{\mathrm{T}}^{\mathrm{miss}}$ plus a veto of any further jet above a certain p_{T} threshold.

(L1) $E_{\mathrm{T}}^{\mathrm{miss}} > 120$ GeV

(L2) leading jet: $p_{\mathrm{T}} > 120$ GeV and $|\eta| < 2$

Source of fake jets	*Loose*	*Tight*=*Loose* or	*Tight*+=*Tight* or
EM coherent noise	f_{em} >0.95 and f_{Q} >0.8 or	f_{em} >0.90 and f_{Q} >0.6 or	
HEC spikes	f_{hec} >0.8 and n_{90} <=5 or f_{hec} >0.5 and f_{Q} >0.5 or	f_{hec} >0.3 and f_{Q} >0.3 or f_{hec} >1-f_{Q} or	
Cosmics and beam-background	t_{jet} >25ns or f_{em} <0.05 or f_{max} >0.99 and $\|\eta\| < 2$	f_{em} <0.1 or f_{max} >0.95 and $\|\eta\| < 2$	f_{em} >0.95 and $f_{\mathrm{ch}} < 0.05$ and $\|\eta\| < 2$

Table 7.2: Bad jet definition according to [87].

	$W \to e\nu$	$W \to \mu\nu$	$W \to \tau\nu$	overall W background	$Z \to \nu\nu$
Total rejection	20±4%	80±2%	21±3%	35±2%	$0.6^{+0.5}_{-0.2}$%

Table 7.3: Rejection power of the lepton veto for different electroweak backgrounds. $Z \to \nu\nu$ gives the same signature as possible signals. Taken from [94].

(L3) second jet (if any): $p_T < 30$ GeV and $|\eta| < 4.5$

HighPt region

In addition to higher p_T and E_T^{miss} requirements, the high kinematic region allows for a second jet up to $p_T < 60$ GeV, that is not pointing in the direction of the missing transverse energy, and sets a veto on the (possible) third jet. The p_T cut on the leading jet is set to a higher value than the one used for the missing transverse energy in order to allow for the second jet.

(H1) $E_T^{miss} > 220$ GeV

(H2) leading jet: $p_T > 250$ GeV and $|\eta| < 2$

(H3) second jet (if any): $p_T < 60$ GeV, $\Delta\phi(\text{jet2}, E_T^{miss}) > 0.5$ and $|\eta| < 4.5$

(H4) third jet (if any): $p_T < 30$ GeV and $|\eta| < 4.5$

7.5 Background estimation

This section summarizes the background estimation methods used in [94]. Data driven methods were employed (whenever possible) in order to check the Monte Carlo estimations. For the QCD background a data-driven estimation method was developed, which is described in more detail below.

7.5.1 Vector boson plus jet background

W and Z plus jet events are the dominant background to this analysis. $Z \to \nu\nu$ plus jet is even irreducible, since it gives the same signature as the possible new physics signal. Following the approach in [68], the `Alpgen` MC is first normalized to the inclusive NNLO cross section and then rescaled via k-factors obtained from comparison of MC prediction to data in control regions.

The systematic uncertainties on the MC prediction were studied in detail in [94], resulting in the following values (quoted numbers correspond to the high kinematic region) for different sources:

- MC renormalization and factorization scale 35%
- jet energy scale uncertainty 10%
- initial and final state radiation 10%
- NNLO calculation and PDF uncertainty 5%
- luminosity 3.4%
- jet energy resolution 1.7%
- variation of the Cell Out energy scale 1.5%

- lepton reconstruction efficiency <1%

By using data driven renormalization the systematic uncertainty of around 40% is reduced substantially to 8.7% (for the overall EW background). A detailed description on the choice of control regions and the uncertainty estimations can be found in [94]. Table 7.4 shows the final numbers of the electroweak background estimation for both signal regions.

	`LowPt` selection	`HighPt` selection
$W \to e\nu$	$64 \pm 4 \pm 8$	$3.0 \pm 0.5 \pm 0.4$
$W \to \mu\nu$	$64 \pm 3 \pm 7$	$3.8 \pm 0.4 \pm 0.4$
$W \to \tau\nu$	$150 \pm 5 \pm 20$	$7.9 \pm 1.1 \pm 1.0$
$Z \to \nu\nu$	$318 \pm 11 \pm 35$	$24.6 \pm 2.6 \pm 2.7$
$Z \to ee$	-	-
$Z \to \mu\mu$	$1.7 \pm 0.14 \pm 0.19$	-
$Z \to \tau\tau$	$2.9 \pm 0.3 \pm 0.4$	-

Table 7.4: Expected number of W/Z+jets background events for an integrated luminosity of 33.4 pb^{-1} for the `LowPt` and the `HighPt` monojet selections. The first and second uncertainties correspond to statistical and systematic uncertainties, respectively. Taken from [94].

7.5.2 Non-collision background

Although very harsh cleaning cuts are applied, the potential remaining non-collision background has to be estimated. The method can be shortly summarized as follows [94]:
One collects fake jets from unpaired (corresponding to beam induced background) and empty (corresponding to cosmic ray induced background) bunches, which pass all cleaning cuts except for the cuts on the charge fraction. After that, the possibility is calculated, that the fake jets are overlaid with genuine proton proton collisions resulting in at least one good vertex. Finally the probability for these overlaid events to pass the charge fraction cuts is calculated.

Altogether this results in an estimation of the non-collision background of (2.4 ± 1.1) events for the `LowPt` and (0.04 ± 0.04) events for the `HighPt` region (normalized to 33.4 pb^{-1}) [94].

7.5.3 QCD background

Despite the harsh cuts imposed on the jets and the missing transverse energy, it is still crucial to estimate the QCD background in the signal regions due to its potentially large cross section. QCD events, which enter the signal selection, are events, where one or more jets are mismeasured or lost (e.g. in calorimeter crack regions).

Two estimation methods were employed and compared to each other. Adapting the proposal in [68], a QCD control region was used in order to normalize the `Pythia` prediction to data. In addition, a data driven method can be applied to the `LowPt` region.

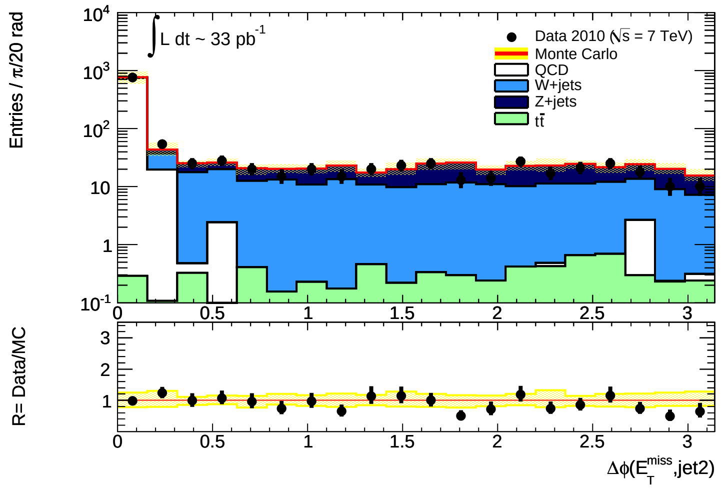

Figure 7.1: Azimuthal angle between the second leading jet and the missing transverse energy in the QCD control region.

Control region

The control region selects dijet events by inverting the veto on the second jet. More precisely, the same trigger, cleaning requirements, lepton veto and kinematic selection are applied as in the `LowPt` signal region. In order to select exclusive dijet events, a second jet with $p_{\mathrm{T}} > 30$ GeV is required and a veto on any third jet with $p_{\mathrm{T}} > 30$ GeV is applied. Figure 7.1 [1] shows the azimuthal angle $\Delta\phi(\mathrm{jet2}, E_{\mathrm{T}}^{\mathrm{miss}})$ between the second leading jet and the missing transverse energy. The region $\Delta\phi(\mathrm{jet2}, E_{\mathrm{T}}^{\mathrm{miss}}) \leq 0.5$ is mostly populated by QCD dijet events, where one jet is badly measured and hence points in the direction of $E_{\mathrm{T}}^{\mathrm{miss}}$. The electroweak background shows a flat behavior in $\Delta\phi(\mathrm{jet2}, E_{\mathrm{T}}^{\mathrm{miss}})$. This region is therefore selected to be the QCD control region and the electroweak background is subtracted (normalized to NLO cross section). Doing that, one gets a normalization factor of (1.13 ± 0.04) for the `Pythia` QCD Monte Carlo. The quoted uncertainty is the quadratic combination of the statistical error and the systematic uncertainty on the electroweak background (c.f. Section 7.5.1). That results in an estimation of the QCD background of (19.1 ± 6.7) events in the `LowPt` and (0.06 ± 0.06) events in the `HighPt` signal region.

Data driven method

Since a veto on the transverse momentum of the second leading jet is applied in the signal regions, this variable can be used to estimate the QCD background directly from data without relying on the QCD Monte Carlo prediction. After the background from Z, W and top is subtracted from the spectrum of the second leading jet (using MC prediction), a fit is applied to the raising slope of the data distribution in order to extrapolate from $p_{\mathrm{T}}(\mathrm{jet2}) > p_T^{veto}$ to

[1] As in Chapter 6, the yellow error band corresponds to the combination of the statistical error and the systematic uncertainty (JES, JER, luminosity).

the signal region with $p_{\mathrm{T}}(\mathrm{jet2}) < p_T^{veto}$. The fit was applied using three different functions: A linear functions, which is used for the central value and a Gaussian and a Landau, which are used as estimate of the systematic uncertainty together with the uncertainty of electroweak background subtraction. Figure 7.2 shows the spectra of the second leading jet with the three fit functions applied to the data. The Monte Carlo prediction was scaled by the normalization factor of 1.13 mentioned above. The linear fit to the data yields [94]

$$f(x) = (0.63 \pm 0.2)x - (1.5 \pm 12)$$

By extrapolating into the signal region, this results in an estimate of the QCD background in the `LowPt` region of $24 \pm 5(\mathrm{stat}) \pm 14(\mathrm{sys})$ events [94], which is in agreement with the estimation using the normalization factor.

For the `HighPt` signal region, the statistics are too low to fit the data points in a meaningful way. But given the estimation of the normalized `Pythia` Monte Carlo prediction, this is an indication, that the QCD background for this signal region is negligible.

7.5.4 Other minor backgrounds

The $t\bar{t}$ process was estimated using Monte Carlo predictions normalized to NNLL cross section calculations, while for the γ+jet process, which is even less relevant, the LO `Pythia` prediction was used. The sum of both backgrounds contributes less than 1% to the overall Standard Model background in the signal regions [94].

7.6 Results

After "opening the signal box" and actually looking at the data in the signal regions, very good agreement was found between the data and the Standard Model expectation. Table 7.6 shows this agreement in the two signal regions (c.f. also Figure 7.4 and Figure 7.5). Given this observation, it was then attempted to set exclusion limits within the Split SUSY model.

7.6.1 Split SUSY interpretation

The signal samples corresponding to the Split SUSY model (c.f. Chapter 2) were generated with `Pythia` and the NLO cross section calculations were done with `PROSPINO`. All Split SUSY signal samples and the NLO cross section calculations used for this study were provided by R. Mackeprang, C. Ohm and D. Milstead [95].

Signal generation

For the simulation of the gluino pair production the `Pythia` generator was used. To accurately simulate the final R-hadron states the string hadronization model [96] was extended by a customized routine that handles the hadronization [97]. The R-hadron interaction in matter was simulated by special `GEANT4` routines based on different scattering models [98, 99, 100], which are taken into account in the systematic uncertainty determination. There are three different scattering models available in `GEANT4`: the 'generic'[100, 101], 'regge' [98, 102] and 'intermediate' [99] model, which are all based on a central picture of a non-interacting heavy

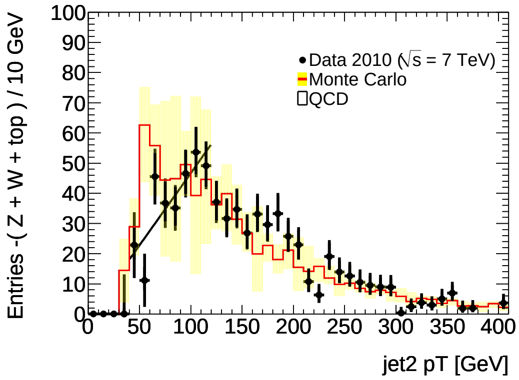

(a)

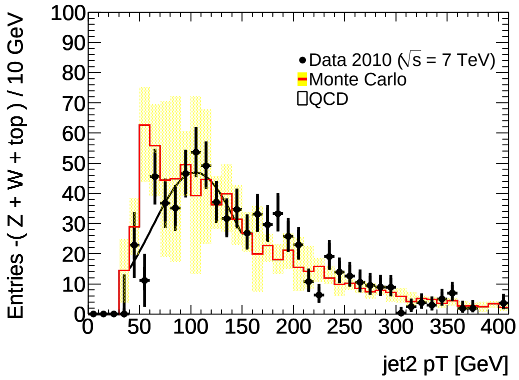

(b)

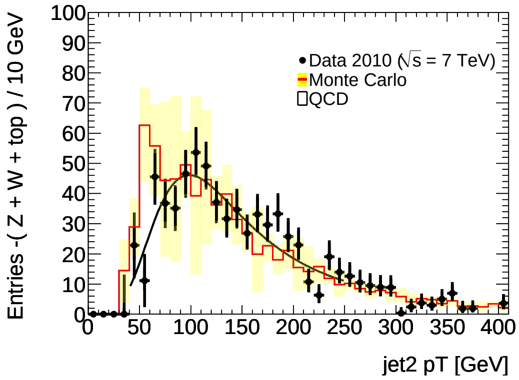

(c)

Figure 7.2: Transverse momentum of the second jet with the extrapolation to the `LowPt` signal region using a linear (a), Gaussian (b) and Landau (c) fit.

	`LowPt` selection	`HighPt` selection
$W \to e\nu$	$64.2 \pm 3.5 \pm 8.3$	$3.0 \pm 0.5 \pm 0.4$
$W \to \mu\nu$	$63.6 \pm 3.3 \pm 7$	$3.8 \pm 0.4 \pm 0.4$
$W \to \tau\nu$	$150.2 \pm 5.3 \pm 19.5$	$7.9 \pm 1.1 \pm 1.0$
$Z \to \nu\nu$	$318 \pm 10.9 \pm 35$	$24.6 \pm 2.6 \pm 2.7$
$Z \to ee$	-	-
$Z \to \mu\mu$	$1.7 \pm 0.14 \pm 0.19$	-
$Z \to \tau\tau$	$2.9 \pm 0.3 \pm 0.4$	-
QCD	$24 \pm 5 \pm 14$	-
$t\bar{t}$	$0.96 \pm 0.04 \pm 0.19$	-
γ+jet	$0.35 \pm 0.04 \pm 0.19$	-
non-collision	$2.4 \pm 0.5 \pm 1.1$	-
Total background	$628.3 \pm 14.6 \pm 52.7$	$39.3 \pm 2.9 \pm 3.4$
Data	611 ± 25	39 ± 6.2

Table 7.5: Summary of background estimations and total number of observed events in 33.4 pb^{-1} of data for the `LowPt` and the `HighPt` monojet selections. The first and second uncertainties correspond to statistical and systematic uncertainties, respectively. Taken from [94].

parton. Since there are large uncertainties on the treatment of gluino based R-hadrons, the 'generic' model was chosen, which relies on a minimal set of underlying assumptions, while the two other models are considered as systematic variations.

Next-to-leading order cross section calculation

The `PROSPINO` program [29] was used to calculate next-to-leading order cross sections for the gluino pair production. Figure 7.3 shows the cross section of the gluino pair production in LO (`Pythia`) and NLO (`PROSPINO`) as a function of the gluino mass. The `PROSPINO` renormalization scale was chosen to be the gluino mass and the CTEQ6.6 [103] parton distribution functions were used. The masses of all the other sparticles were set to 10 TeV, which is appropriate for the Split SUSY model, where their influence on the gluino production cross section is small (c.f. Chapter 2).

Monte Carlo samples

Table 7.6 summarizes the signal samples used in this analysis showing the mass, the scattering model and the sample ID. In addition, the probability $p_{\tilde{g}g}$ that a gluino hadronizes into a gluinoball formed from a gluino-gluon bound state, was varied from the conventional 10% to

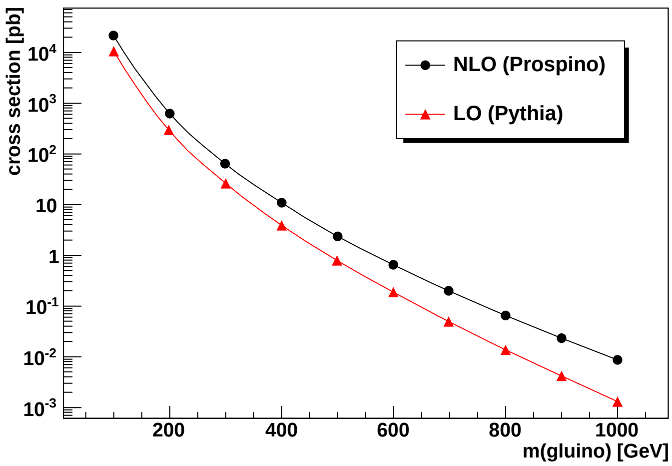

Figure 7.3: Cross section of the gluino pair production in LO (`Pythia`, red triangles) and NLO (`PROSPINO`, black circles) as a function of the gluino mass.

50% and 100% respectively. For all of the three scenarios, the exclusion limits are calculated separately.

Signal efficiency

Table 7.7 shows the number of events (normalized to 33.4 pb^{-1}) for the R-hadron signal samples with gluino masses from 100 to 1000 GeV after each cut of the event selection. The signal selection efficiencies are in the range of 1 to 8% for the `LowPt` kinematic region and in the range of 0.2 to 3 % for the `HighPt` kinematic region. The efficiencies are smaller for small masses and increase to higher masses of the gluino. Figure 7.4 and Figure 7.5 show the missing transverse energy, the transverse momentum of the leading jet and the azimuthal angle between the two, for the SM background and selected signal samples in the `LowPt` and `HighPt` kinematic region, respectively. Also here the good agreement between data and Standard Model expectation can be observed.

In the following paragraphs the different sources of systematic errors of the signal are discussed. These systematics are then taken into account for the exclusion limit calculation.

For each of the three available hadronization models ('generic', 'intermediate', 'regge') the exclusion limits are calculated separately, although the 'generic' model is treated as the default one for the event generation.

Systematic Uncertainties

Next-to-leading order cross section and PDF uncertainty: The variation of the renormalization scale (set to the gluino mass) by a factor of two up and down lead to a 15% variation in cross section [95]. Changing the pdfs from CTEQ6.6 [103] to MSTW [104] resulted in a variation of less than 5% [95].

Gluino mass (GeV)	Scattering Model	ID
100	generic	114760
200	generic	114761
300	generic	114762
400	generic	114763
500	generic	114764
600	generic	114765
700	generic	114766
800	generic	114767
900	generic	114768
1000	generic	114769
100	regge	114790
300	regge	114792
500	regge	114794
700	regge	114796
100	intermediate	114820
300	intermediate	114822
500	intermediate	114824
700	intermediate	114826

Table 7.6: Simulated gluino R-hadron signal samples. The production cross sections are shown in Figure 7.3.

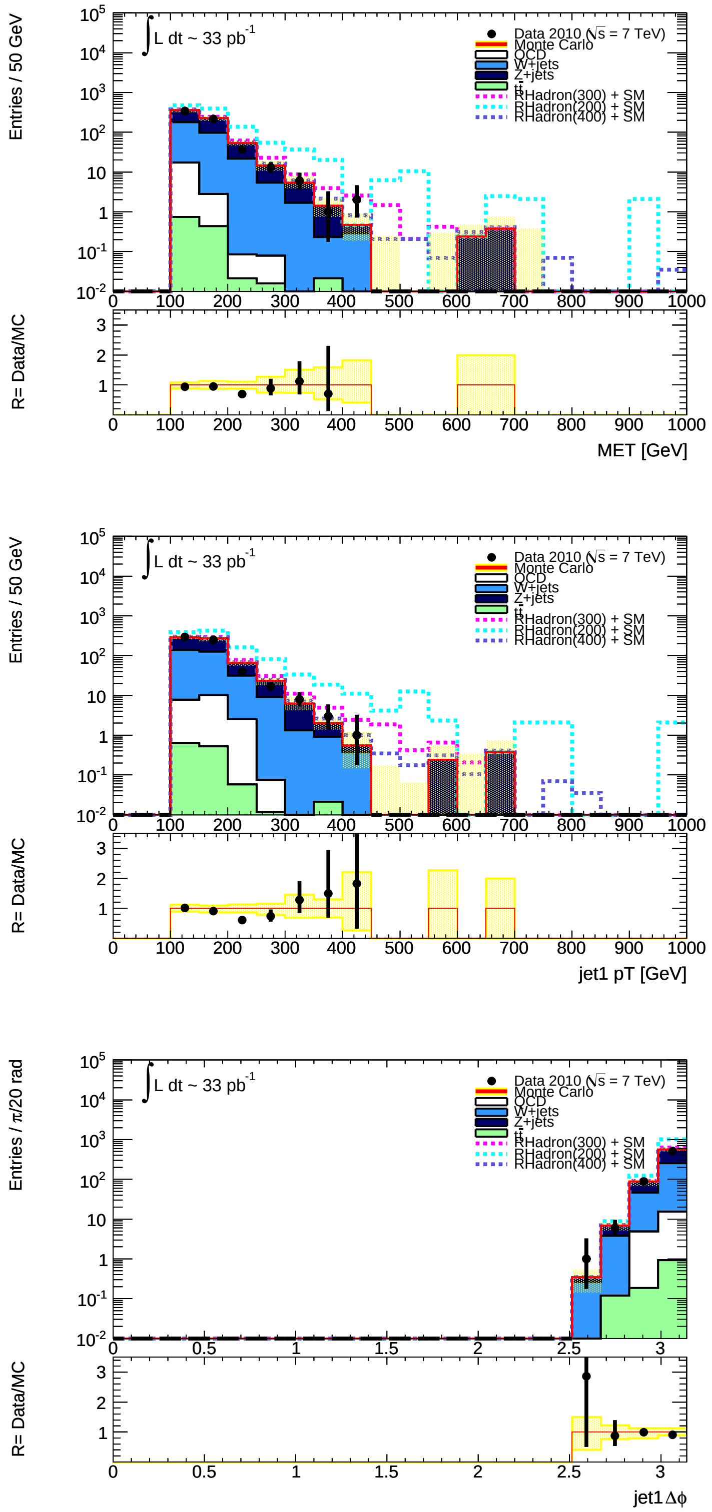

Figure 7.4: Missing transverse energy, p_{T} of the leading jet and $\Delta\Phi$ between the leading jet and the missing transverse energy in the `LowPt` kinematic region for data, the SM background and the R-hadron signal (showing gluino masses from 200 to 400 GeV).

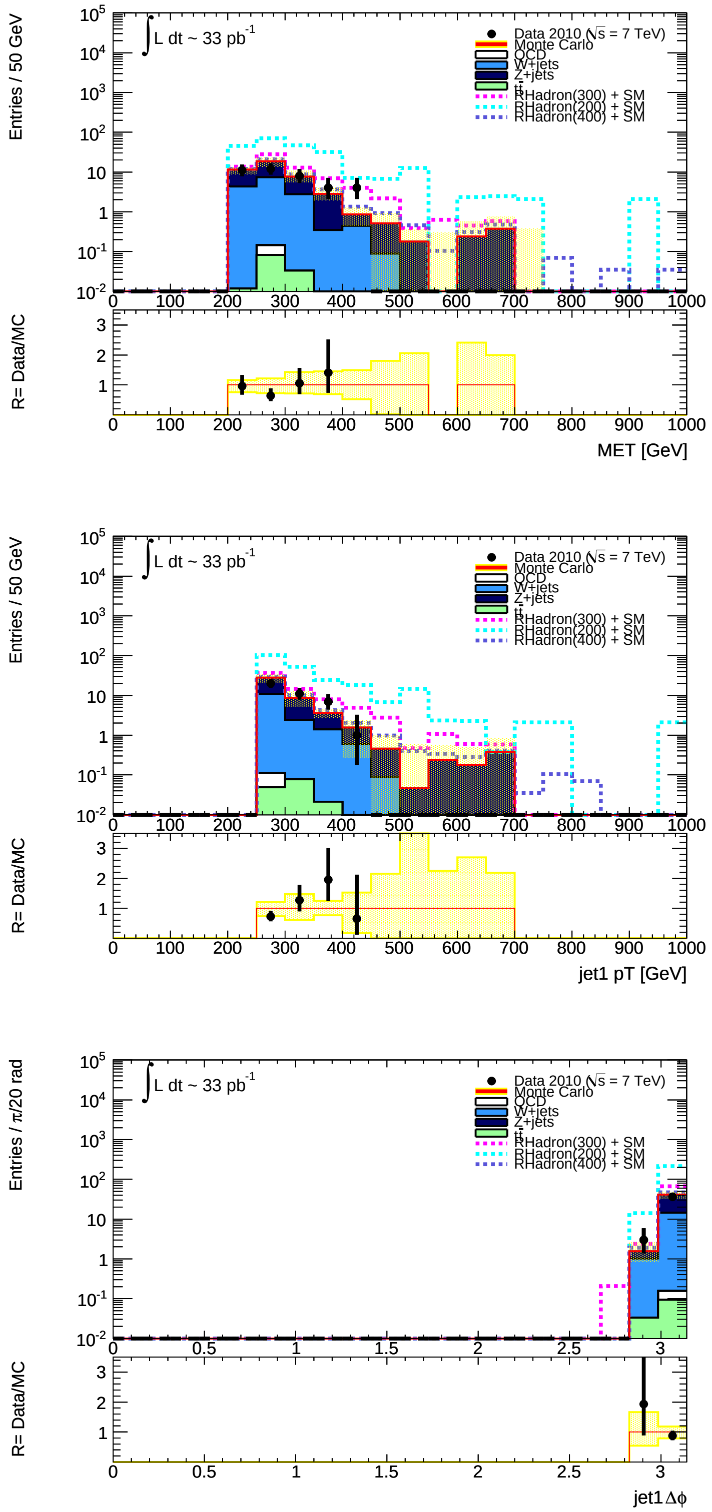

Figure 7.5: Missing transverse energy, p_{T} of the leading jet and $\Delta\Phi$ between the leading jet and the missing transverse energy in the HighPt kinematic region for data, the SM background and the R-hadron signal (showing gluino masses from 200 to 400 GeV).

	Gluino mass [GeV]									
Cut	100	200	300	400	500	600	700	800	900	1000
P1 (GRL)	708114	20875	2074	347	78	21	6.5	2.2	0.78	0.29
P2 (trigger)	92971	5000	639	122	30	8.8	2.8	0.98	0.36	0.14
P3 (vertex)	92971	4997	639	122	30	8.8	2.8	0.98	0.36	0.14
P4 (cleaning)	81996	4574	547	107	25	7.5	2.4	0.82	0.29	0.11
P5 (lepton veto)	69109	3634	429	82	19	5.7	1.8	0.35	0.23	0.09
L1 ($E_{\mathrm{T}}^{\mathrm{miss}}$ cut, low)	24712	1557	216	44	11	3.3	1.09	0.38	0.15	0.05
L2 (leading jet p_{T}, low)	17844	1100	158	32	7.9	2.4	0.81	0.29	0.11	0.04
L3 (second jet veto, low)	6585	486	61	13	2.9	0.89	0.30	0.11	0.04	0.01
H1 ($E_{\mathrm{T}}^{\mathrm{miss}}$ cut, high)	6514	472	73	16	4.1	1.4	0.50	0.17	0.07	0.03
H2 (leading jet p_{T}, high)	4319	301	47	11	2.7	0.91	0.31	0.12	0.04	0.02
H3 (second jet p_{T}, high)	1912	200	29	6.6	1.5	0.53	0.18	0.07	0.02	0.01
H4 (third jet veto, high)	1346	188	27	6.0	1.4	0.47	0.16	0.06	0.02	0.01

Table 7.7: Cutflow table for the Split SUSY Signal and different gluino masses. The samples are normalized to 33.4 pb^{-1} and were generated with the 'generic' model and $p_{\tilde{g}g}$ of 10%. For the cut definitions c.f. Section 7.4.

Initial state radiation: Higher order QCD radiation is handled in `Pythia` via the parton shower algorithm. The uncertainty associated with the ISR was estimated by varying the corresponding `Pythia` parameters `parp64` and `parp67`. `parp64` is the parameter by which the squared transverse momentum evolution scale is multiplied while `parp67` is the parameter by which the scale of the hard scattering Q^2 is multiplied to define the maximum parton virtuality allowed in Q^2 ordered showers. Both are modifying the phase space in which emission can occur. According to a recommendation of the `Pythia` authors [95] the following set of parameters were used: `parp64`=0.25 `parp67`=6.0 and `parp64`=0.5 `parp67`=4.0. This variation of the parameters results in an estimated 15% variation of the number of events that pass the selection (c.f. Table 7.8).

The correct modelling of the ISR is crucial for the investigated process. There are ongoing studies by N. Kanaya, comparing the `Pythia` to the `MadGraph` [105] prediction. Since `MadGraph` includes the radiation in the matrix element calculation rather than in the parton shower, it is expected to model the process more accurately.

Possibility of hadronizing into gluinoballs: Varying the probability $p_{\tilde{g}g}$ for a gluino to hadronize into a electrically neutral gluinoball from 10% to 50% or 100% respectively lead to a up to 30% variation of the number of events that pass the selection (c.f. Table 7.9). Therefore, the three different probabilities $p_{\tilde{g}g}$ are also treated separately for the exclusion limit calculation. For this comparison the 'generic' hadronization model was assumed.

	nominal	ISR up	ISR down
signal region	100% (9950 events generated)	100% (5264 events generated)	100% (5264 events generated)
`LowPt`	2.95%	2.72%	3.12%
`HighPt`	1.29%	1.27%	1.12%

Table 7.8: Cut efficiency for variations of the ISR at a gluino mass of 300 GeV using the 'generic' model and 10% gluinoball hadronization probability.

		$p_{\tilde{g}g}$		
$m_{\tilde{g}}$[GeV]	signal region	10%	50%	100%
100	`LowPt`	6585	6939	8568
	`HighPt`	1345	1912	1629
300	`LowPt`	61	67	76
	`HighPt`	27	28	37
500	`LowPt`	2.9	3.1	3.9
	`HighPt`	1.4	1.6	2.0
700	`LowPt`	0.30	0.30	0.33
	`HighPt`	0.16	0.18	0.20

Table 7.9: Number of events (normalized to 33.4 pb^{-1}) that pass the selection for different probabilities $p_{\tilde{g}g}$ of hadronizing into gluinoballs.

Jet energy scale: The jet energy was scaled up and down using the `JESUncertainty Provider` tool [90], which provides an η and p_{T} dependent parametrization of the jet energy scale uncertainty leading to an average scale uncertainty per jet of about 7%. The missing transverse energy is recalculated taken the changes of the jets into account. Table 7.10 and 7.11 show the impact of this uncertainty for a number of gluino masses in the 'generic' model for $p_{\tilde{g}g}$=10%. The difference on the number of events passing the selection is accounted for with a conservative 10% systematic error.

$m_{\tilde{g}}$[GeV]	nominal	JES up	JES down
200	486	482	495
300	61	59	64
400	13	13	13

Table 7.10: Impact of the jet energy scale uncertainty on the number of events (normalized to 33.4 pb^{-1}) that pass the `LowPt` signal selection for different gluino masses, the 'generic' model and $p_{\tilde{g}g}$=10%.

$m_{\tilde{g}}$[GeV]	nominal	JES up	JES down
200	188	188	171
300	27	28	27
400	6.0	6.1	5.9

Table 7.11: Impact of the jet energy scale uncertainty on the number of events (normalized to 33.4 pb^{-1}) that pass the `HighPt` kinematic signal selection for different gluino masses, the 'generic' model and $p_{\tilde{g}g}$=10%.

Jet energy resolution: To account for the uncertainty of the jet energy resolution a random variation of the jet p_T is applied following the recipe in [91]. Each jet p_{T} is smeared independently with a p_T-dependent Gaussian resolution of

$$0.55\sqrt{\frac{(4.6\ \mathrm{GeV})^2}{p_T^2} + \frac{0.846^2\ \mathrm{GeV}}{p_T} + 0.064^2}.$$

Table 7.12 shows the impact on the number of events passing the `LowPt` and `HighPt` kinematic signal region selection. The resulting variation is below 3%.

Luminosity: Due to the uncertainty on the integrated luminosity a 3.2% error was assigned to the signal acceptance.

Effect of pile-up: The effect of pile-up is estimated using dedicated pile-up samples and comparing the number of events passing the selection cuts with non-pile-up samples. The nominal signal MC samples do not include the effect of pile-up (in contrast to the background

	`LowPt` kinematic selection		`HighPt` kinematic selection	
$m_{\tilde{g}}$[GeV]	nominal	smeared	nominal	smeared
200	486	486	188	186
300	61	61	27	27
400	13	13	6.0	6.3

Table 7.12: Impact of the jet energy resolution on the number of events (normalized to 33.4 pb^{-1}) that pass the signal selection for different gluino masses, the 'generic' model and $p_{\tilde{g}g}$=10%.

samples). Table 7.13 shows the comparison. The variation due to pile-up is accounted for with a 3% uncertainty.

	`LowPt` kinematic selection		`HighPt` kinematic selection	
$m_{\tilde{g}}$[GeV]	nominal	pile-up	nominal	pile-up
500	3.0	2.8	1.4	1.4
600	0.92	0.94	0.48	0.51
700	0.31	0.31	0.16	0.16

Table 7.13: Impact of pile-up on the number of events (normalized to 33.4 pb^{-1}) that pass the signal selection for different gluino masses, the 'generic' model and $p_{\tilde{g}g}$=10%.

Comparison to the multijet analysis

As a simple comparison to the potential reach in the multijet channels, the significances in the two signal regions are computed and compared to the ones obtained in chapter 6. Table 7.14 shows, that the significance in the `HighPt` signal region is considerably higher than in all the multijet signal regions, where the maximum value is 3.2 (c.f. Table 6.11). The lower significance in the `LowPt` region is due to more background entering this selection, but the `HighPt` signal region is clearly favorable to any multijet analysis.

region	`LowPt`	`HighPt`
$S/\sqrt{B}$	2.4	4.3

Table 7.14: Significance for a R-hadron signal with $m_{\tilde{g}}$ = 300 GeV in the two monojet signal regions.

Setting limits on the gluino mass

Procedure: In order to set a limit on the mass of the gluino, a simple approach was chosen based on a counting experiment. For both the `LowPt` and `HighPt` kinematic signal region the number of events - for the signal, the Standard Model background and the data - surviving these cuts are passed to the ROOT class TLimit [106], which makes use of the so-called modified frequentists approach. Given this information and the above mentioned systematic errors, confidence levels for the signal plus background and the background only hypothesis tests are calculated based on a likelihood ratio test statistic. The systematic uncertainties are taken into account by convoluting the probability density function describing the event yield in the signal region with a Gaussian function corresponding to the size of the systematic uncertainties. A detailed discussion on the limit setting procedure is given in [106].

Results: For the results the different hadronization models as well as the different $p_{\tilde{g}g}$ are treated separately. Quoted are confidence levels derived with two different methods: CL_{s+b} , which is the probability of observing the signal plus background hypothesis given the signal hypothesis is true and $CL_s = CL_{s+b}/CL_b$, which is more conservative. They are quoted both, so the reader might choose the one, he would like to compare with. Nevertheless, the more conservative CL_s was chosen for the summary of the results. CL_s is less sensitive to fluctuations of the background than CL_{s+b} and therefore is the more conservative approach.

Table 7.15 and 7.16 show the observed CL_s and CL_{s+b} and the expected $< CL_s >$ and $< CL_{s+b} >$ confidence levels in the `LowPt` and `HighPt` kinematic signal region for different gluino masses and different $p_{\tilde{g}g}$ in the 'generic' model.

The same was done using the two alternative hadronization models for $p_{\tilde{g}g}$=10%. Table 7.17 and 7.18 show the confidence level for different gluino masses and the three different hadronization models in the `LowPt` and `HighPt` kinematic region.

For convenient comparison the results are displayed graphically in the following plots, where the `HighPt` kinematic region was chosen as it provides more stringent limits. The individual points are connected via a simple line, giving a conservative guideline for the eye. Figure 7.6 shows the different expected confidence levels for a range of gluino masses produced with the 'generic' model and a probability of hadronizing into gluinoballs of 10%. The expected 95% exclusion limit is around $m_{\tilde{g}} \approx 320$ GeV for CL_s. CL_{s+b} leads to an improved expected 95% exclusion limit of and $m_{\tilde{g}} \approx 340$ GeV. The observed limits are also at $m_{\tilde{g}} \approx 320$ GeV for CL_s and at $m_{\tilde{g}} \approx 340$ GeV for CL_{s+b}.

In Figure 7.7 the influence of the probability $p_{\tilde{g}g}$ of hadronizing into gluinoballs is illustrated. The observed 95% exclusion limit (CL_s) varies between 310 and 315 GeV for the gluino mass. Figure 7.8 on the other hand shows the influence of the different handronization models for a fixed $p_{\tilde{g}g}$ of 10%. The expected exclusion limit (CL_s) for the mass of the gluino varies from 310 to 315 GeV.

Figure 7.9 shows the 95% CL_s limit as function of the gluino mass as combined cross section times acceptance for the high kinematic region. The acceptance was calculated using the values in Table 7.7 and goes from 0.2% for a gluino mass of 100 GeV up to 2.5% for 700 GeV.

$p_{\tilde{g}g}$=10%				
$m_{\tilde{g}}$ [GeV]	CL_s	CL_{s+b}	$< CL_s >$	$< CL_{s+b} >$
100	0	0	0	0
200	0.15%	0.07%	0.18%	0.09%
300	30.5%	14.1%	31.9%	16.0%
400	32.5%	15.0%	35.6%	17.9%
500	34.2%	15.8%	36.9%	18.5%
$p_{\tilde{g}g}$=50%				
$m_{\tilde{g}}$ [GeV]	CL_s	CL_{s+b}	$< CL_s >$	$< CL_{s+b} >$
100	0	0	0	0
300	22.8%	10.5%	24.7%	12.4%
500	32.4%	15.0%	35.2%	17.7%
$p_{\tilde{g}g}$=100%				
$m_{\tilde{g}}$ [GeV]	CL_s	CL_{s+b}	$< CL_s >$	$< CL_{s+b} >$
100	0	0	0	0
300	29.1%	13.4%	30.3%	15.2%
500	33.4%	15.4%	36.0%	18.0%

Table 7.15: Observed and expected confidence level for different gluino masses, different $p_{\tilde{g}g}$ and the 'generic' model in the `LowPt` kinematic region.

$p_{\tilde{g}g}$=10%				
$m_{\tilde{g}}$ [GeV]	CL_s	CL_{s+b}	$< CL_s >$	$< CL_{s+b} >$
100	0	0	0	0
200	$1e^{-7}$	$6e^{-8}$	$1e^{-7}$	$6e^{-8}$
300	3.7%	1.79%	3.4%	1.79%
400	62.9%	30.6%	58.4%	30.6%
500	91.8%	44.7%	85.4%	44.7%
$p_{\tilde{g}g}$=50%				
$m_{\tilde{g}}$ [GeV]	CL_s	CL_{s+b}	$< CL_s >$	$< CL_{s+b} >$
100	$5e^{-10}$	$2e^{-10}$	$4e^{-10}$	$2e^{-10}$
300	3.0%	1.47%	2.8%	1.47%
500	96.0%	48.7%	89.2%	46.7%
$p_{\tilde{g}g}$=100%				
$m_{\tilde{g}}$ [GeV]	CL_s	CL_{s+b}	$< CL_s >$	$< CL_{s+b} >$
100	$3e^{-9}$	$2e^{-9}$	$3e^{-9}$	$2e^{-9}$
300	1.02%	0.49%	0.95%	0.49%
500	84.6%	41.2%	78.6%	41.2%

Table 7.16: Observed and expected confidence level for different gluino masses, different $p_{\tilde{g}g}$ and the 'generic' model in the `HighPt` kinematic region.

'generic'				
$m_{\tilde{g}}$ [GeV]	CL_s	CL_{s+b}	$< CL_s >$	$< CL_{s+b} >$
100	0	0	0	0
200	0.15%	0.07%	0.18%	0.09%
300	30.5%	14.1%	31.9%	16.0%
400	32.5%	15.0%	35.6%	17.9%
500	34.2%	15.8%	36.9%	18.5%

'intermediate'				
$m_{\tilde{g}}$ [GeV]	CL_s	CL_{s+b}	$< CL_s >$	$< CL_{s+b} >$
100	0	0	0	0
300	24.8%	11.4%	25.8%	12.9%
500	33.4%	15.4%	36.6%	18.3%

'regge'				
$m_{\tilde{g}}$ [GeV]	CL_s	CL_{s+b}	$< CL_s >$	$< CL_{s+b} >$
100	0	0	0	0
300	20.5%	9.4%	22.2%	11.2%
500	33.2%	15.4%	36.3%	18.3%

Table 7.17: Observed and expected confidence level for different gluino masses, different hadronization models and $p_{\tilde{g}g}$=10% in the `LowPt` kinematic region.

'generic'				
$m_{\tilde{g}}$ [GeV]	CL_s	CL_{s+b}	$< CL_s >$	$< CL_{s+b} >$
100	0	0	0	0
200	$1e^{-7}$	$6e^{-8}$	$1e^{-7}$	$6e^{-8}$
300	3.7%	1.79%	3.4%	1.79%
400	62.9%	30.6%	58.4%	30.6%
500	91.8%	44.7%	85.4%	44.7%
'intermediate'				
$m_{\tilde{g}}$ [GeV]	CL_s	CL_{s+b}	$< CL_s >$	$< CL_{s+b} >$
100	0	0	0	0
300	0.79%	0.39%	0.74%	0.39%
500	82.5%	40.3%	76.8%	40.3%
'regge'				
$m_{\tilde{g}}$ [GeV]	CL_s	CL_{s+b}	$< CL_s >$	$< CL_{s+b} >$
100	0	0	0	0
300	0.69%	0.34%	0.65%	0.34%
500	84.6%	41.2%	78.6%	41.2%

Table 7.18: Observed and expected confidence level for different gluino masses, different hadronization models and $p_{\tilde{g}g}$=10% in the `HighPt` kinematic region.

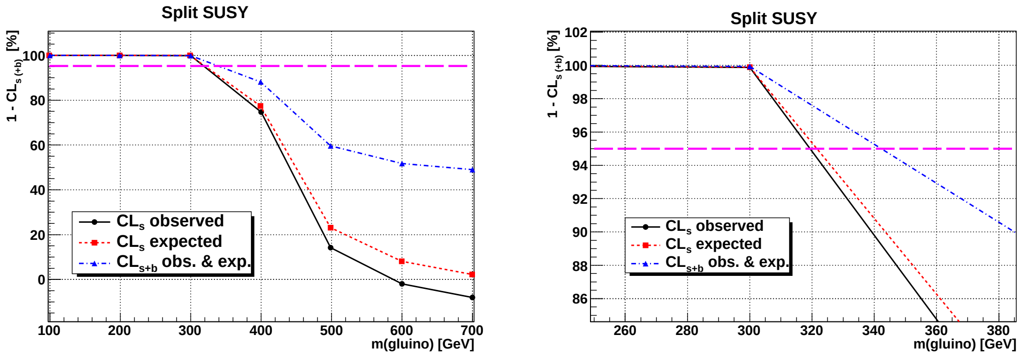

Figure 7.6: Comparison of the different confidence levels for the high kinematic region, the 'generic' hadronization model and $p_{\tilde{g}g}$=10%. The left plot shows the gluino mass range between 100 and 500 GeV; the right plot shows the area relevant for a 95% exclusion. The dashed pink line marks the 95% exclusion border.

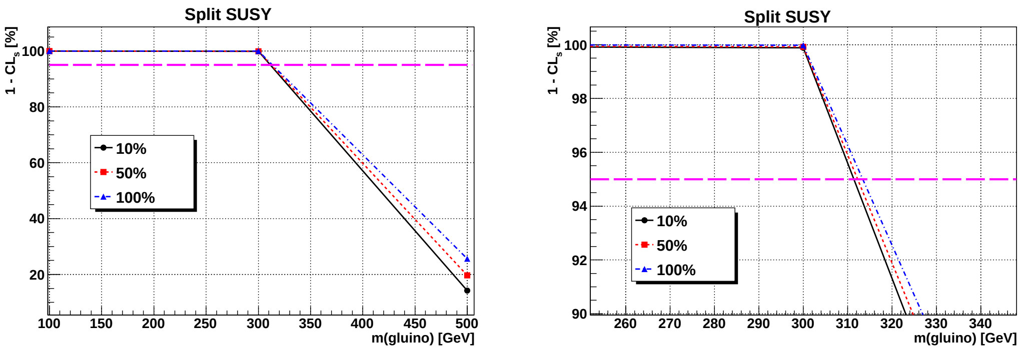

Figure 7.7: Comparison of the impact of the different probabilities $p_{\tilde{g}g}$ for the 'generic' model. The left plot shows the gluino mass range between 100 and 500 GeV; the right plot shows the area relevant for a 95% exclusion. The dashed pink line marks the 95% exclusion border.

Discussion Considering the different models, systematics and limit calculation algorithms a conservative 95% exclusion limit of 315 GeV is placed on the gluino mass with this analysis. This is worse than the limit achieved with the dedicated R-hadron analysis [95, 107], where the R-hadrons are required to be charged. Electrical neutral R-hadrons are not covered in [95, 107], whereas this analysis specifically focusses on this particular case.

7.7 Summary

The monojet analysis, which is a joint effort of the ATLAS SUSY and EXOTICS groups [94], has been presented. For this effort, the QCD background estimation method was developed together with J. Abdallah using data driven normalization factors and a data driven fit. Both methods deliver compatible results. Other background estimates done in [94] have been summarized. As a final result of this study, exclusion limits on a Split SUSY scenario were calculated. Gluino masses below 315 GeV are excluded with 95% confidence level, including

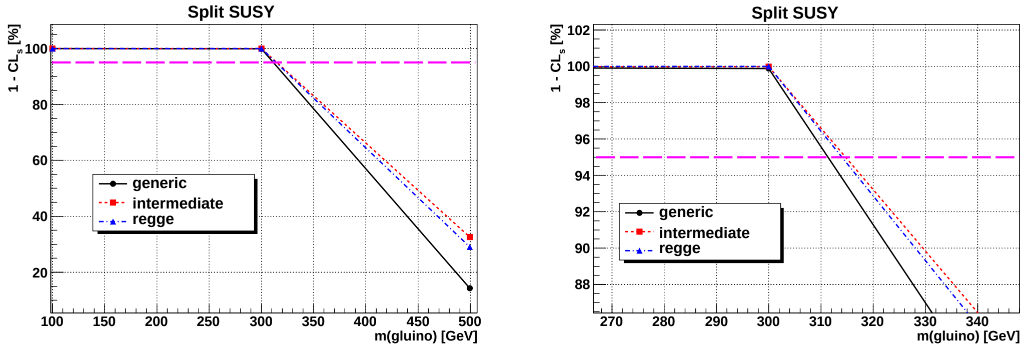

Figure 7.8: Comparison of the impact of the different hadronization models for a fixed value of $p_{\tilde{g}g}$=10%. The left plot shows the gluino mass range between 100 and 500 GeV; the right plot shows the area relevant for a 95% exclusion. The dashed pink line marks the 95% exclusion border.

both charged and neutral R-hadrons.

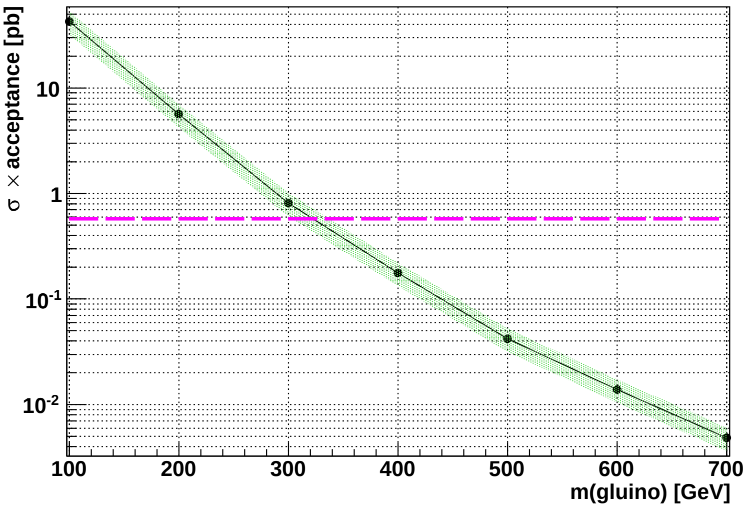

Figure 7.9: Cross section times acceptance for the high kinematic region. The NLO prediction intersects with the 95% CL_s limit line at ~ 320 GeV. The green band corresponds to a 20% error accounting for cross section and acceptance uncertainty.

Chapter 8

Conclusion

This thesis represents the work, which was done within the ATLAS SUSY and EXOTICS groups concerning the searches for new particles in channels with jets and missing transverse momentum. In the course of the thesis the ATLAS experiment went from the late preparation to the early running stage.

Before any actual ATLAS data (using all subsystems together) was available, an early study investigated the capabilities of a simple monojet analysis to spot detector effects like hot or dead cells in the calorimeter (c.f. Chapter 4). The study showed, that the detector effects not only could be found but could even be distinguished. The excellent quality of the collision data, that has first been taken two years later, was not expected at the time the study was done. Nevertheless it shows, that certain distributions are critical to look at for a monojet analysis in order to exclude detector problem effects.

The next step towards the analyses, whose objective is the search for new physics, was the study of non-collision background (c.f. Chapter 5). It used MC of various background sources as well as data from cosmic rays and single beam events. A combination of cleaning cuts using track and calorimeter based jet variables was optimized with multivariate techniques via TMVA. The study, which improved the background rejection compared to earlier studies, contributed to the development of the cleaning cuts used for the 2010 SUSY analyses.

The ATLAS runs in 2010 delivered ~ 35 pb^{-1} of data suitable for the searches for new physics in the SUSY and EXOTICS group. For both analyses, which are covered in this thesis, no significant excess with respect to SM expectation was observed.

The estimation of the SM background is the most crucial part in searches for new physics. Especially at the early running stage of the LHC, when a new kinematic region in phase space is explored for the first time, one cannot completely rely on MC predictions. Therefore, it is crucial to use data-driven methods in order to determine the SM background.

A partially data-driven QCD background determination method was developed for the SUSY analysis, which focused on channels with two or three jets (inclusive), missing transverse momentum and no isolated lepton [68]. The QCD background in the signal regions was estimated by rescaling the MC prediction by normalization factors, which were determined in control regions. The result, which was confirmed by alternative methods [68], contributed to the final limit calculation, which significantly improved the existing exclusion limits for the mSUGRA and another constraint MSSM model [68, 69]. In the restricted case with $m_{\tilde{q}} = m_{\tilde{g}}$, masses below 775 GeV (mSUGRA) and 870 GeV (constraint MSSM) are excluded at 95% confidence level [68, 69].

For the monojet analysis, which is an ongoing joint study between the ATLAS SUSY and EXOTICS groups [94], the QCD background was estimated. In addition to the method, which was already mentioned, another data-driven method was developed. The fit to the p_T spectrum of the second leading jet in a control region is extrapolated into the signal region in order to estimate the QCD background there. The result was consistent with the one using normalization factors. Together with the other background estimations [94], this result was used in the calculation of exclusion limits in the Split SUSY model. Gluino masses below 315 GeV could be excluded at 95% confidence level. In contrary to the limits in [95, 107], this value also includes the possibility of electrically neutral R-hadrons.

Chapter 9

Acknowledgments

These last paragraphs are dedicated to all the people, whom I very much like to thank for their various supports.

First of all, I'm very grateful to Gregor Herten for the opportunity to do my PhD in his group. I would like to thank him in particular for his open door policy, the confidence he put in his students and the freedom of work I enjoyed during my time in his group as well as for his spot on comments and questions.

I'd like to acknowledge the fellowship granted by the Graduiertenkolleg "Physik an Hadron-Beschleunigern" of the "Deutsche Forschungsgemeinschaft" (DFG).

My thanks go to all the current and former members of our working group in Freiburg. It's been a pleasure working with you guys! In the following I'd like to thank some of those people in particular.

I thank Sascha Caron for the supervision of the thesis and for always pointing me into the right direction. His ideas kept me on track and his enthusiasm towards particle physics is a true inspiration. I'd like to thank Zuzana Rurikova for our pleasant team work, the fruitful discussions, her suggestions and patients and of course for the tea; Jan Erik Sundermann for the collaboration, helping with various kinds of computing issues, for always making time for my questions and problems, for many nice barbecues and gaming nights; Michael Rammensee for his help with statistics; my Brazilian buddy Bernhard Meirose for the supervision of the beam background study and the good times we had, not only during our great collaboration on the analysis. It's been a "grandiose Zeit"! My fellow partner in crime Stephan Horner for the great team work, discussions (on both work and non-physics issues) and the fantastic time we had in Vancouver. It's been a long road - and man, we made it! Many thanks to Ulrich Landgraf, Bernhard Pfeifer and Jürgen Tobias for their various professional and personal supports. I'd like to thank Anton Gamel and Adil Aktas for the direct connection to the computing center.

For proof reading the manuscript I'm once more in debt of Sascha Caron, Zuzana Rurikova, Jan Erik Sundermann, Michael Rammensee and Bernhard Meirose.

I'd like to thank all the members of the various ATLAS working groups, whom I had the pleasure to work with. In particular I'd like to thank Alden Stradling and Richard Teuscher for their support concerning the non-collision background study; Rasmus Mackeprang, Christian Ohm and David Milstead for providing the R-hadron Monte Carlo samples and answering many of my thick questions on that matter; Naoko Kanaya and Jalal Abdallah for the collaboration in the monojet analysis.

To all of my friends, who were there during this exciting, sometimes back-breaking but overall wonderful adventure: Thank you so much! This thing couldn't have happened without your support.

I'd like to thank my former teacher Bernd Kretschmer for his dedication and enthusiasm. It was his influence that encouraged me to take up physics as a field of study.

Three people I cannot thank enough: My parents, who brought me up the way I am and who have supported me with never-dwindling confidence and love my whole life, and my brother, who simply is my brother. They have been my hold and support when things seem to go to shreds as well as the people with whom I've shared joy and success.

To all of you, once again, thank you!

Appendix A

Jet definitions used in the analyses

This chapter gives a brief introduction on the definition of jets and their requirements in general as well as the specifics of the jet algorithms, which are used in this work. A detailed description can be found e.g. in [108].

A.1 Jet definition

Since individual quarks and gluons, which are produced in collision events, are not observed individually, a construct called "jet" is used to describe the features of the final state. Therefore, a jet has, by definition, integer charge and zero colour. It is important to understand, that a jet is defined by an algorithm, which is run on the final state, and neither by the raw detector data, nor by the individual partons.

The jet algorithm should ideally satisfy all of the following requirements:
The result of the algorithm should be stable and reproducable and the algorithm has to perform well in terms of speed if the multiplicity increases, since many LHC events will contain a large number of high p_{T} jets. The effects of hadronisation and the underlying event on the jet should be small and it should be possible to compare the result of the algorithm to theoretical calculations in a meaningful way. In particular, the jet algorithm has to be comparable to at least NLO QCD predictions in order to achieve the desired precision. This implies, that the algorithm should be colinear and infrared safe, meaning there must not be large fluctuations due to colinear splitting of the input objects to the algorithm (colinear), or to addition of soft particles (infrared).

The following two jet algorithms were used in this work.

A.2 The ATLAS cone algorithm

This algorithm is based on the maximisation of the energy in a geometric cone, that is defined in the $\eta - \phi$ plane by the radius R. It is run iteratively, defining a candidate cone, calculating the new momentum vector and redrawing the cone around the new center until the process converges. Cones sharing energy are either split into two or merged into one single jet depending on the energy fraction they share.

Since the ATLAS cone algorithm relies on a seed for the first candidate cone, it is neither infrared nor collinear safe and therefore was replaced in more recent studies.

A.3 The ATLAS anti-$k_\perp$ algorithm

The anti-$k_\perp$ algorithm is based on the clustering of the initial constituents. The clustering is defined by a distance measure ΔR between the objects and a condition, which determines when the clustering should be terminated. For this particular clustering algorithm, all softer objects near a hard object are merged together into the hard object, so that the jet boundary is not affected by soft radiation.

Appendix B

Excluding one event from the Pythia J1 sample

As stated in Chapter 4 an event from the `Pythia` J1 dijet sample with a $\hat{p}_T$ between 17 and 35 GeV should not be able to pass the event selection cuts. But in this particular event (event number: 71263) there is one reconstructed high p_T jet and a large amount of missing transverse energy (Table B.1). The jet and the missing transverse energy are back to back

object	p_T [GeV]	η	Φ
jet	162.6	0.484	2.01
$E_{\mathrm{T}}^{\mathrm{miss}}$	161.7		-1.018

Table B.1: Reconstructed objects in the `Pythia` QCD J1 event number 71263.

in the Φ plane balancing each other (note that jets with $p_T < 20$ GeV are discarded by the jet selection criteria applied). The truth jets of this event are shown in Table B.2. No true jet corresponding to the hard reconstructed jet is found. Hence there seems to be something wrong with the reconstruction of this particular event. Looking at the event with the Atlantis event display [58] confirms this.

In Figure B.1 one can see that there are no tracks pointing to the calorimeter cluster which is responsible for the hard jet. Regarding all these features there is a strong hint that this event suffers from a bug in `GEANT4`. The following citation is taken from the savannah bug tracker [109]: "In the high energy collision of sigma+ and a nucleon, some low energy particles are added to the backward reaction hemisphere in order to simulate the intra-nuclear cascade and nuclear de-excitation. Occasionally, the leading particle algorithm incorrectly selects one of these backward particles as the leading particle and dumps a large amount of energy into it as a crude way to balance energy. When the boost to the lab frame is made, this particle has enough energy to remain backward, thus causing the problem."

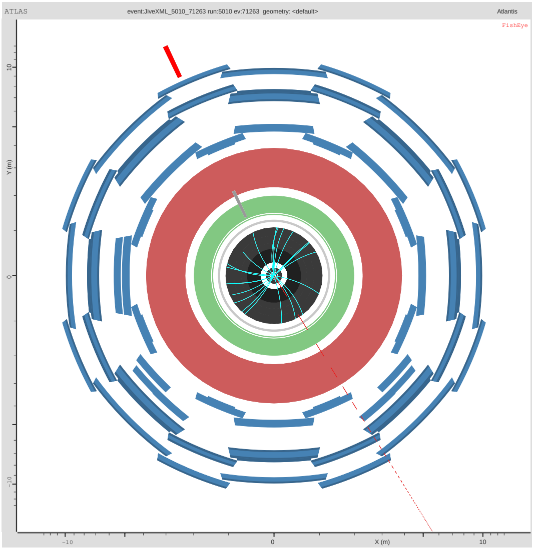

XY plane

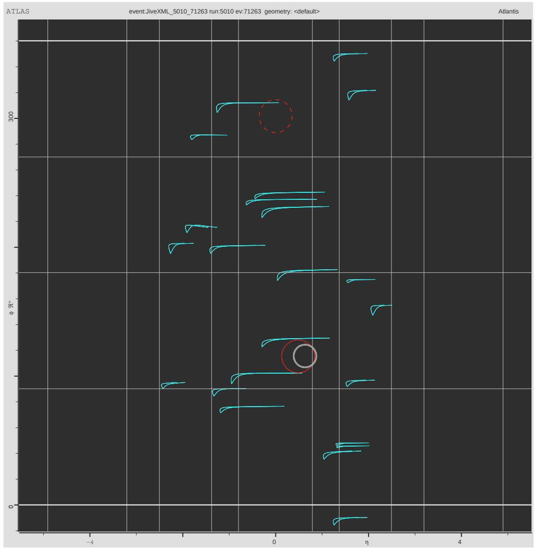

Φ η projection

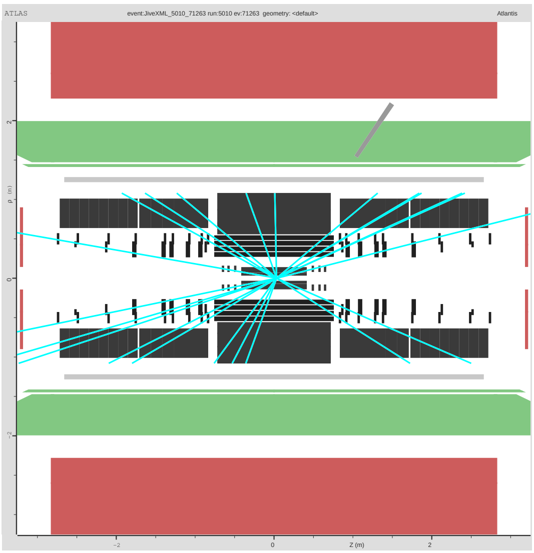

ρ Z projection (zoomed)

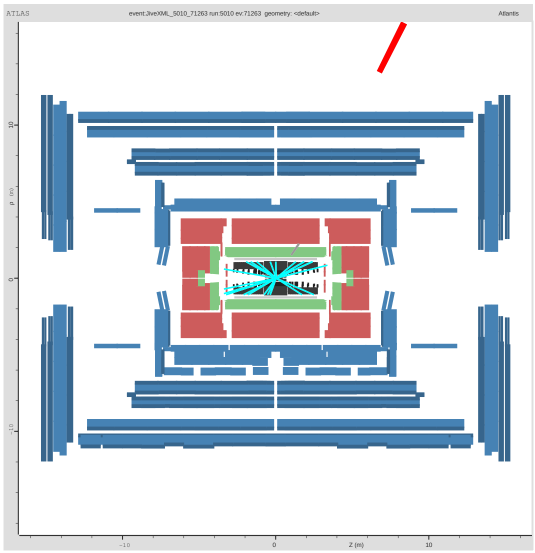

ρ Z projection

Figure B.1: Atlantis event display of suspicious J1 event 71263.
Event display made from AOD (no calorimeter cells shown).
E_T^{miss}: red dashed line, tracks: light blue lines, calorimeter cluster: grey bar (upper right: circle), Cone4H1TowerJet: red bar (upper right: circle).

object	p_T [GeV]	η	Φ
$E_{\mathrm{T}}^{\mathrm{miss}}$	0.		0.
jet	25.8	4.72	-1.11
jet	15.7	3.26	-2.87
jet	15.0	-2.72	-2.82
jet	12.5	1.37	0.83
jet	12.0	-0.54	-1.93
jet	11.3	-1.31	1.30
jet	9.9	3.45	2.32
jet	9.4	1.33	0.40
jet	9.1	1.76	2.97
jet	8.4	4.58	1.74
jet	7.2	-2.42	0.64

Table B.2: Truth objects in the `Pythia` QCD J1 event number 71263.

Appendix C

Additional information for the searches in events with two or three jets

C.1 Monte Carlo samples

All Monte Carlo samples used in the analysis - besides the two signal grids - are listed in the following tables.

Sample ID	Name	Generator	Cross Section [pb]	k–factor	N_{gen}
107680	WenuNp0_pt20	Alpgen Jimmy	6913.3	1.199	1381931
107681	WenuNp1_pt20	Alpgen Jimmy	1293.0	1.199	258408
107682	WenuNp2_pt20	Alpgen Jimmy	377.1	1.199	188896
107683	WenuNp3_pt20	Alpgen Jimmy	100.9	1.199	50477
107684	WenuNp4_pt20	Alpgen Jimmy	25.3	1.199	12991
107685	WenuNp5_pt20	Alpgen Jimmy	6.9	1.199	3449
107690	WmunuNp0_pt20	Alpgen Jimmy	6913.3	1.199	1386038
107691	WmunuNp1_pt20	Alpgen Jimmy	1293.0	1.199	255909
107692	WmunuNp2_pt20	Alpgen Jimmy	377.1	1.199	187860
107693	WmunuNp3_pt20	Alpgen Jimmy	100.9	1.199	50877
107694	WmunuNp4_pt20	Alpgen Jimmy	25.3	1.199	12991
107695	WmunuNp5_pt20	Alpgen Jimmy	6.9	1.199	3498
107700	WtaunuNp0_pt20	Alpgen Jimmy	6913.3	1.199	1365491
107701	WtaunuNp1_pt20	Alpgen Jimmy	1293.0	1.199	254753
107702	WtaunuNp2_pt20	Alpgen Jimmy	377.1	1.199	188446
107703	WtaunuNp3_pt20	Alpgen Jimmy	100.9	1.199	50472
107704	WtaunuNp4_pt20	Alpgen Jimmy	25.3	1.199	12996
107705	WtaunuNp5_pt20	Alpgen Jimmy	6.9	1.199	3998
106280	WbbNp0_pt20	Alpgen Jimmy	3.2	1.22	6499
106281	WbbNp1_pt20	Alpgen Jimmy	2.6	1.22	5500
106282	WbbNp2_pt20	Alpgen Jimmy	1.4	1.22	2997
106283	WbbNp3_pt20	Alpgen Jimmy	0.6	1.22	1500

Table C.1: W + jet Monte Carlo samples including cross section times branching ratio, the k–factors and the number of generated events of the sample. The k–factors are the NNLO/LO scaling factors used to scale the overall cross section for $W \to l\nu$ to the total NNLO inclusive cross section [68].

.

Sample ID	Name	Generator	Cross Section [pb]	k–factor	N_{gen}
107650	ZeeNp0_pt20	Alpgen Jimmy	664.1	1.25	304216
107651	ZeeNp1_pt20	Alpgen Jimmy	133.0	1.25	63440
107652	ZeeNp2_pt20	Alpgen Jimmy	40.23	1.25	19497
107653	ZeeNp3_pt20	Alpgen Jimmy	11.14	1.25	5499
107654	ZeeNp4_pt20	Alpgen Jimmy	2.899	1.25	1499
107655	ZeeNp5_pt20	Alpgen Jimmy	0.753	1.25	500
107660	ZmumuNp0_pt20	Alpgen Jimmy	664.1	1.25	303947
107661	ZmumuNp1_pt20	Alpgen Jimmy	133.0	1.25	62996
107662	ZmumuNp2_pt20	Alpgen Jimmy	40.23	1.25	18993
107663	ZmumuNp3_pt20	Alpgen Jimmy	11.14	1.25	5497
107664	ZmumuNp4_pt20	Alpgen Jimmy	2.899	1.25	1499
107665	ZmumuNp5_pt20	Alpgen Jimmy	0.753	1.25	499
107670	ZtautauNp0_pt20	Alpgen Jimmy	664.1	1.25	303359
107671	ZtautauNp1_pt20	Alpgen Jimmy	133.0	1.25	63481
107672	ZtautauNp2_pt20	Alpgen Jimmy	40.23	1.25	19492
107673	ZtautauNp3_pt20	Alpgen Jimmy	11.14	1.25	5497
107674	ZtautauNp4_pt20	Alpgen Jimmy	2.899	1.25	1499
107675	ZtautauNp5_pt20	Alpgen Jimmy	0.753	1.25	499
107710	ZnunuNp0_pt20	Alpgen Jimmy	28.05	1.28	2999
107711	ZnunuNp1_pt20	Alpgen Jimmy	428.9	1.28	44487
107712	ZnunuNp2_pt20	Alpgen Jimmy	193.1	1.28	39491
107713	ZnunuNp3_pt20	Alpgen Jimmy	58.3	1.28	11995
107714	ZnunuNp4_pt20	Alpgen Jimmy	14.5	1.28	7993
107715	ZnunuNp5_pt20	Alpgen Jimmy	4.7	1.28	8662

Table C.2: Z + jet Monte Carlo samples including cross section times branching ratio, the k–factors and the number of generated events of the sample. The k–factors are the NNLO/LO scaling factors used to scale the overall cross section for $Z \to \nu\bar{\nu}$ and $Z \to l^+l^-$ to the total NNLO inclusive cross section [68]. The values for $Z \to \nu\bar{\nu}$ already include the efficiency of the event filter, which was imposed on those samples and requires at least one jet above $p_{\text{T}} > 25$ GeV.

Sample ID	Name	Generator	Cross Section [pb]	N_{gen}
105200	T1	MC@NLO Jimmy	89.4	999387
105204	TTbar_FullHad	MC@NLO Jimmy	71.4	149899
108340	st_tchan_enu	MC@NLO Jimmy	7.0	9993
108341	st_tchan_munu	MC@NLO Jimmy	7.0	9997
108342	st_tchan_taunu	MC@NLO Jimmy	7.0	10000
108343	st_schan_enu	MC@NLO Jimmy	0.468	9950
108344	st_schan_munu	MC@NLO Jimmy	0.468	9996
108345	st_schan_taunu	MC@NLO Jimmy	0.468	9996
108346	st_Wt	MC@NLO Jimmy	13.0	14995

Table C.3: Top Monte Carlo samples at NLO with NLL used in the 0-lepton analyses including cross section times branching ratio and the number of generated events of the sample [68].

Sample ID	Name	Generator	Cross Section [pb]	N_{gen}
105009	J0 jetjet	Pythia	$9750{\cdot}10^6$	1,399,184
105010	J1 jetjet	Pythia	$673{\cdot}10^6$	1,395,383
105011	J2 jetjet	Pythia	$41{\cdot}10^6$	1,398,078
105012	J3 jetjet	Pythia	$2.2{\cdot}10^6$	1,397,430
105013	J4 jetjet	Pythia	$88{\cdot}10^3$	1,397,401
105014	J5 jetjet	Pythia	2330	1,391,612
105015	J6 jetjet	Pythia	33.8	1,347,654

Table C.4: QCD Monte Carlo samples including cross sections and the number of generated events of the sample [68].

Sample ID	Name	Generator	Cross Section [pb]	N_{gen}
106484	SUSY SU4 point	Herwig++	59.6	49,954
114068	SUSY $m_0 = 200\,\mathrm{GeV}$, $m_{1/2} = 190\,\mathrm{GeV}$	Herwig++	19.4	9,989

Table C.5: SUSY benchmark point Monte Carlo samples including cross sections and the number of generated events of the sample [68].

C.2 Additional control plots

In the following, additional plots of various observables from the two control regions used for the QCD background estimation are shown.

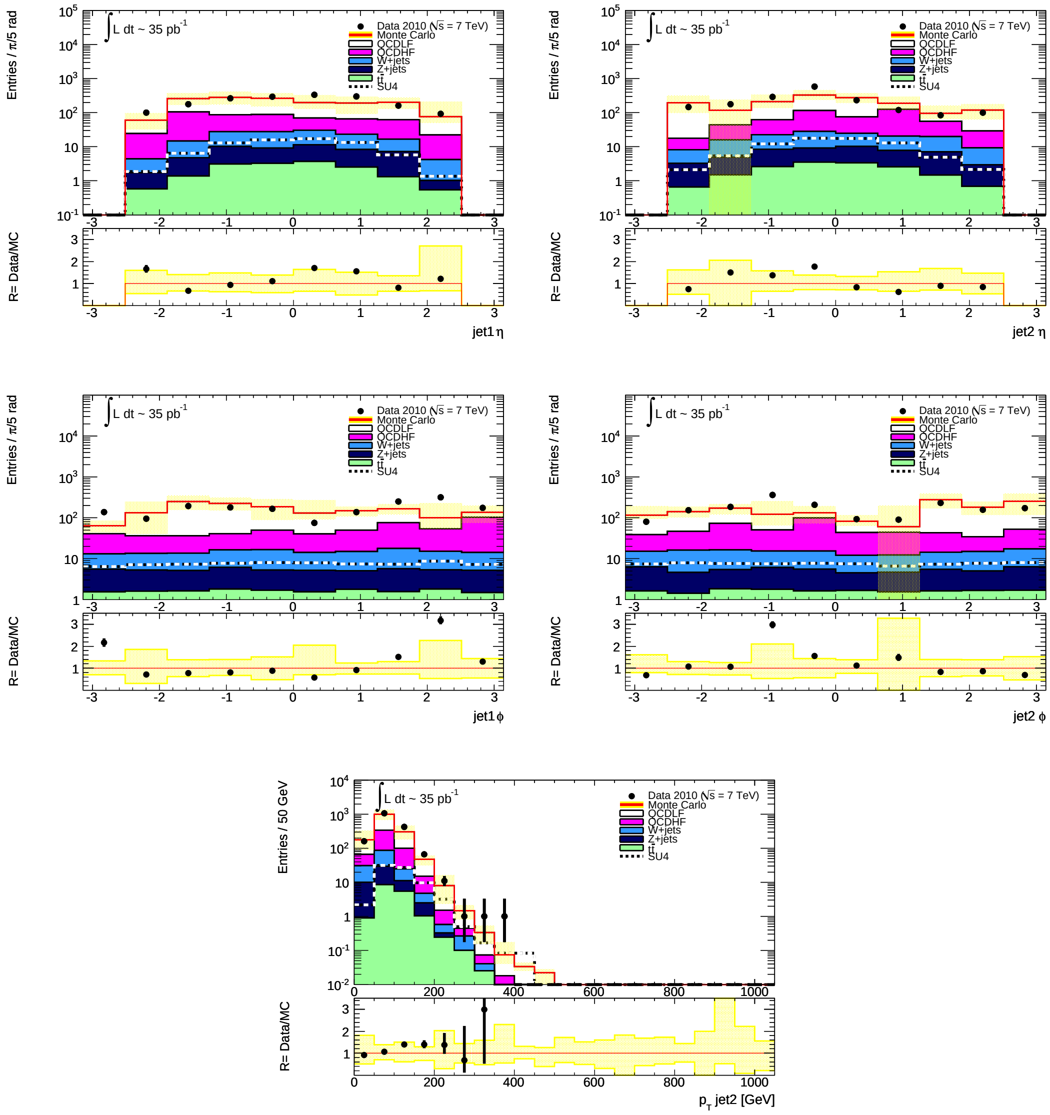

Figure C.1: Pseudorapidity η and azimuthal angle ϕ of the first and second leading jet as well as the transverse momentum of the second leading jet for the 2 jet channel in the control region with inverted $\Delta\Phi$ cut

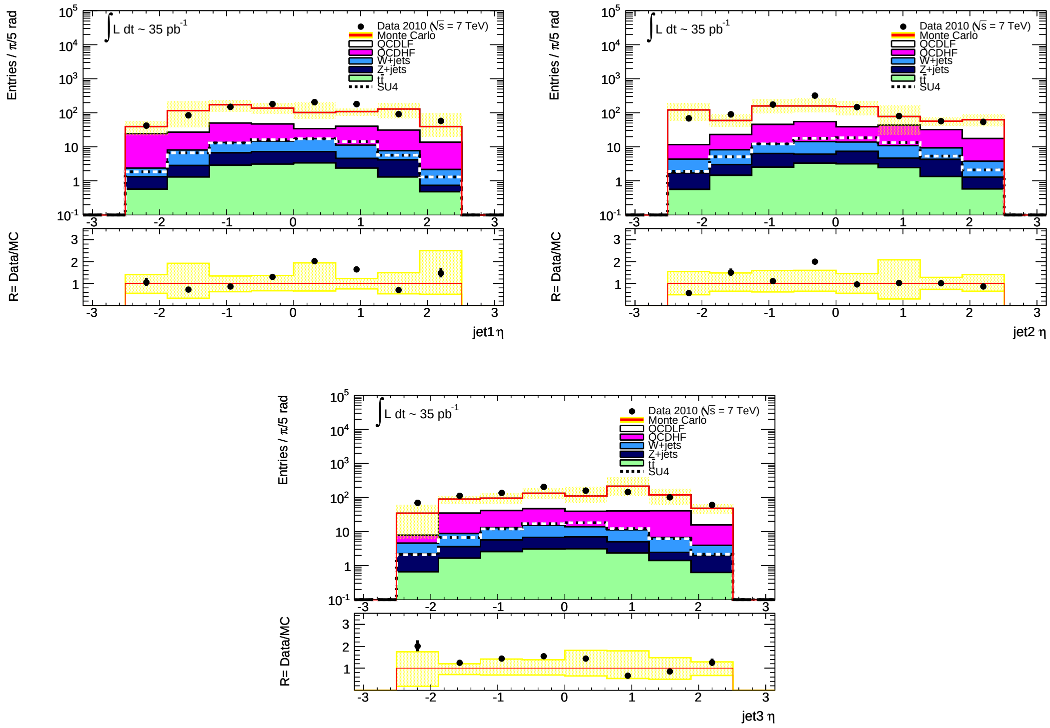

Figure C.2: Pseudorapidity η the first three leading jets for the 3 jet channel in the control region with inverted $\Delta\Phi$ cut

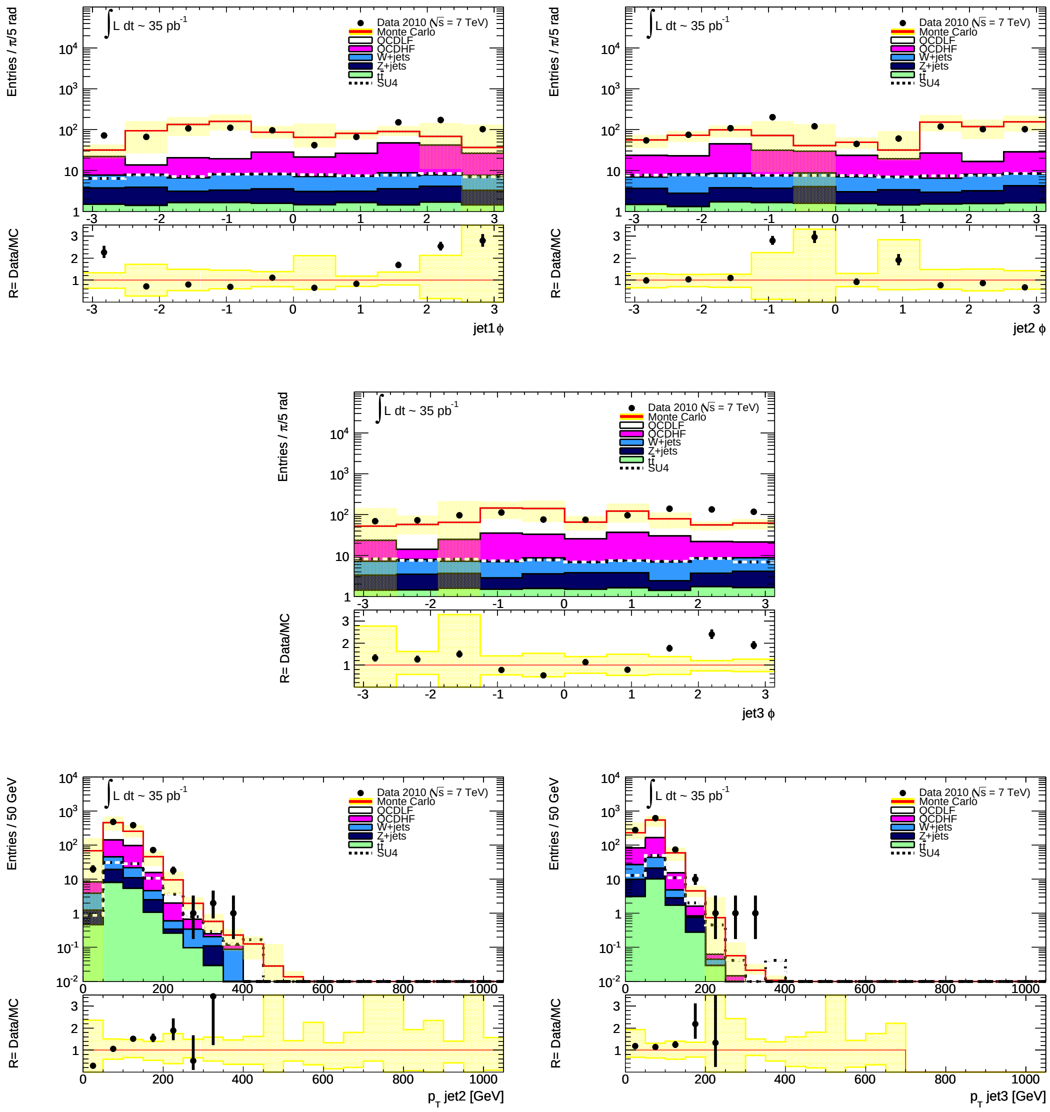

Figure C.3: Azimuthal angle ϕ of the first three leading jets as well as the transverse momentum of the second and third leading jet for the 3 jet channel in the control region with inverted $\Delta\Phi$ cut

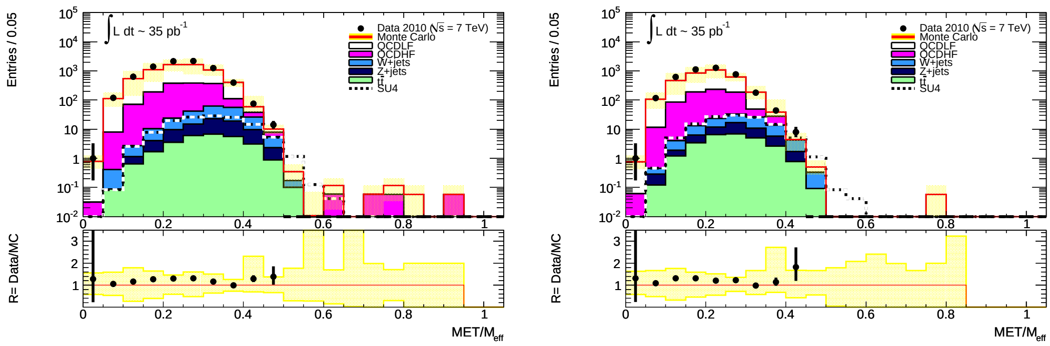

Figure C.4: $E_{\mathrm{T}}^{\mathrm{miss}}/m_{\mathrm{eff}}$ for the 2-(left) and 3-(right) jet channel in the control region with inverted $\Delta\Phi$ cut. No cut on this variable is yet applied

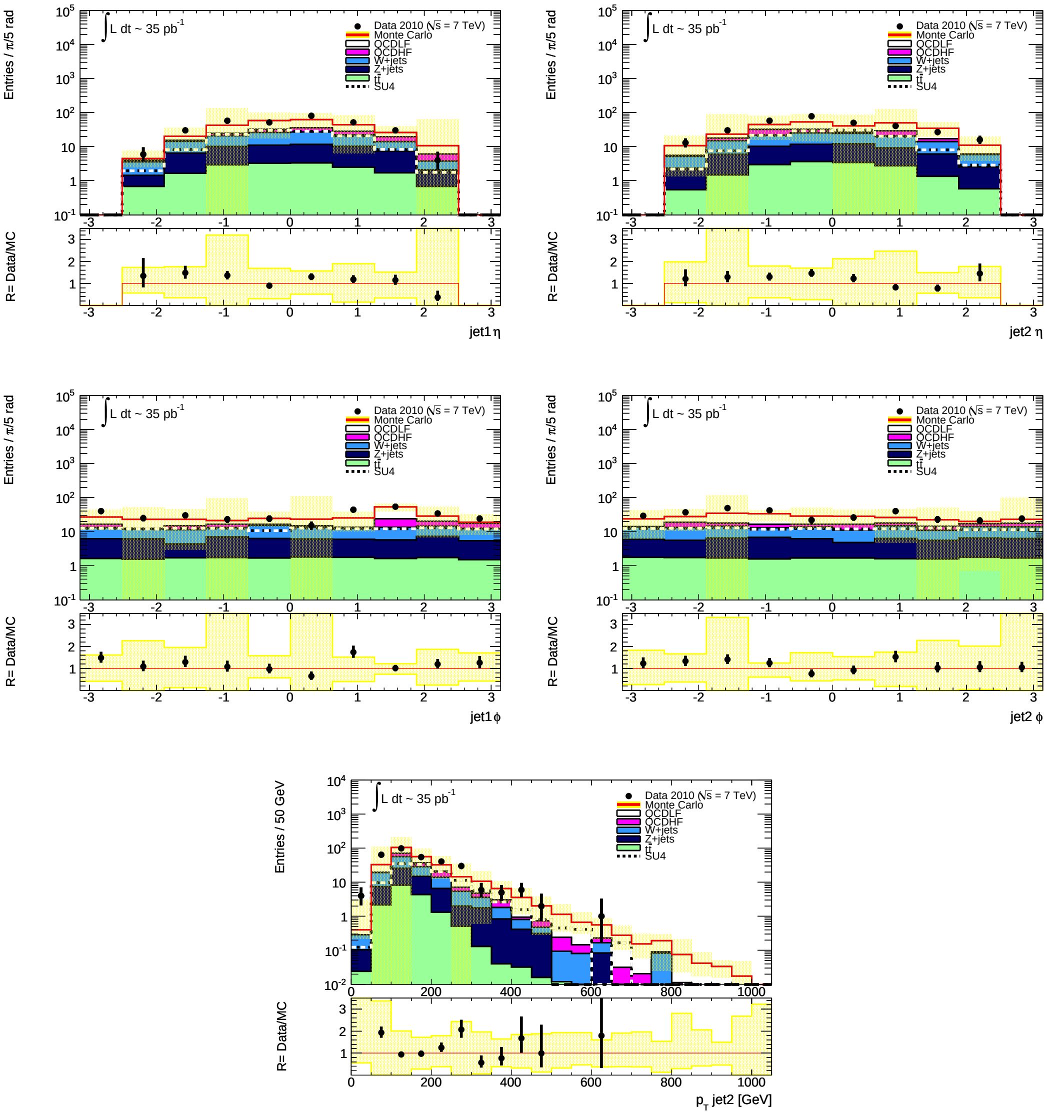

Figure C.5: Pseudorapidity η and azimuthal angle ϕ of the first and second leading jet as well as the transverse momentum of the second leading jet for the 2 jet channel in the control region with inverted $E_{\mathrm{T}}^{\mathrm{miss}}/m_{\mathrm{eff}}$ cut

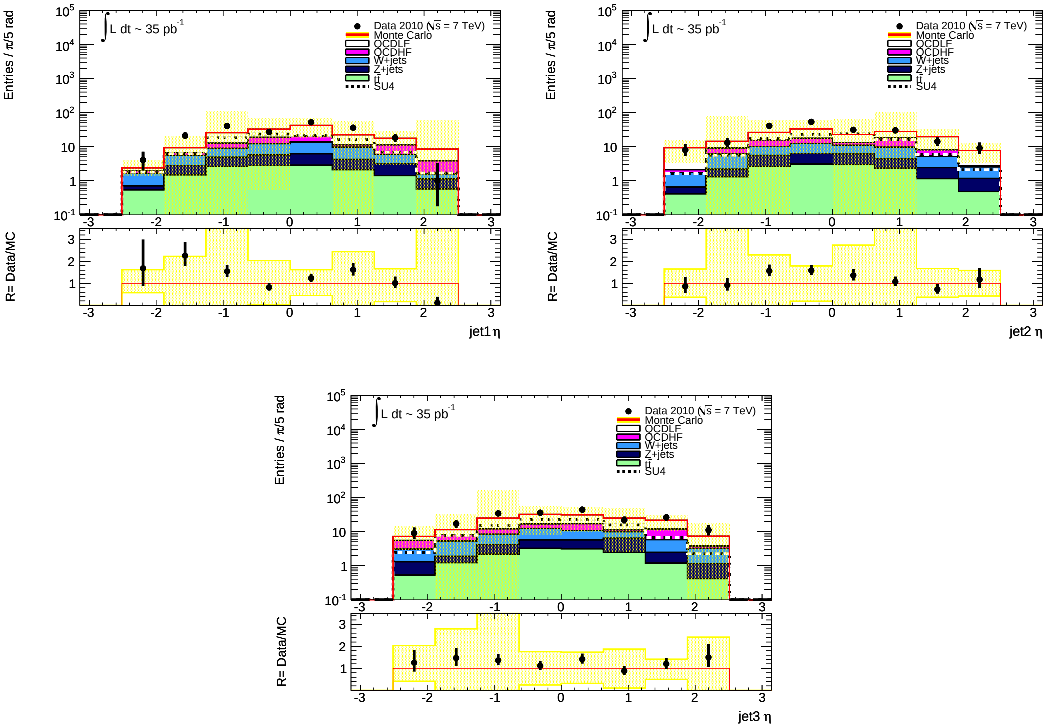

Figure C.6: Pseudorapidity η of the first three leading jets for the 3 jet channel in the control region with inverted $E_{\mathrm{T}}^{\mathrm{miss}}/m_{\mathrm{eff}}$ cut

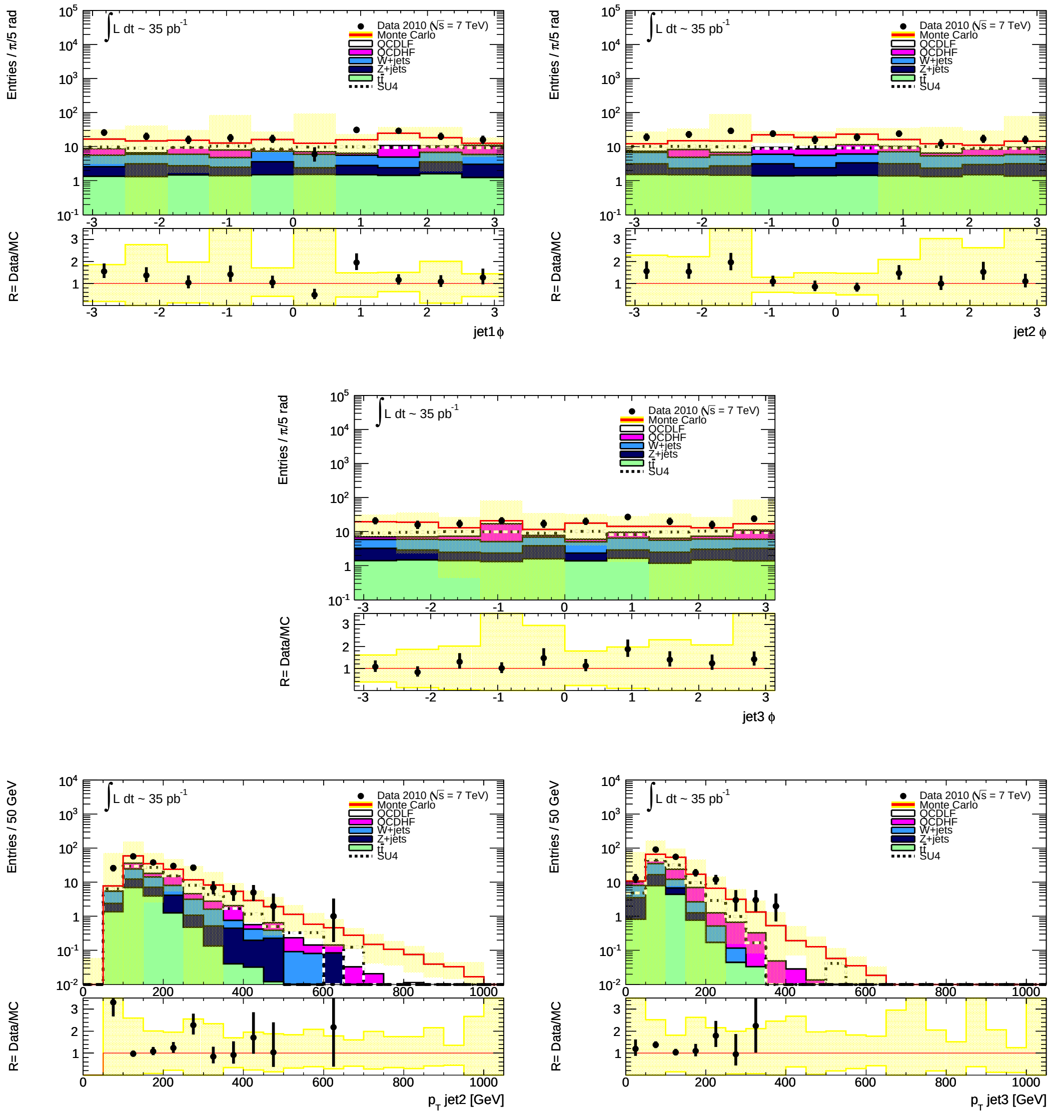

Figure C.7: Azimuthal angle ϕ of the first three leading jets as well as the transverse momentum of the second and third leading jet for the 3 jet channel in the control region with inverted $E_{\mathrm{T}}^{\mathrm{miss}}/m_{\mathrm{eff}}$ cut

Appendix D

Additional information on the monojet channel

D.1 Additional control plots

The following figures show the control distributions, which are considered important to guarantee absence of non-physics backgrounds according to Chapter 4. Figure D.1 shows the η and ϕ of the leading jet, the azimuthal angle of the $E_{\mathrm{T}}^{\mathrm{miss}}$ and the $\Delta\phi$ between the leading jet and the missing transverse energy after all selection cuts for the `LowPt` region (L3), as well as the $\Delta\phi$ after only the $E_{\mathrm{T}}^{\mathrm{miss}}$ selection cut (L1). Figure D.2 shows the same quantities for the `HighPt` selection (H4 or H1, respectively).

There is good agreement between the observed data and the SM expectation for both cases. Non of the possible effects described Chapter 4 can be found. This stresses the extremely good quality of the data, that is taken by the ATLAS detector.

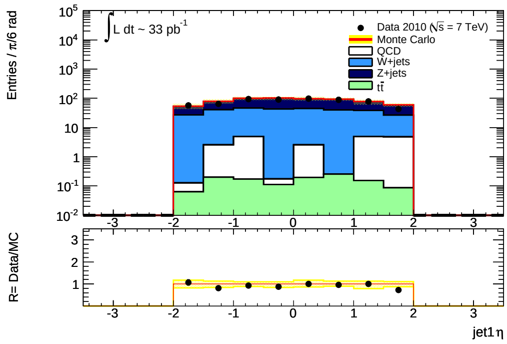

(a)

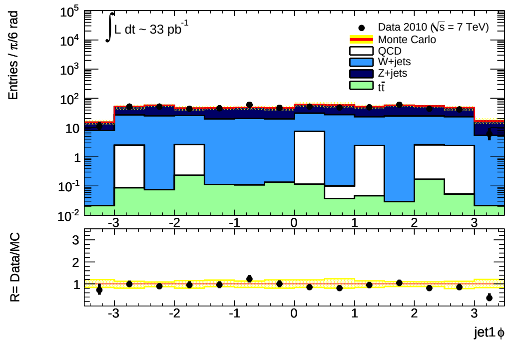

(b)

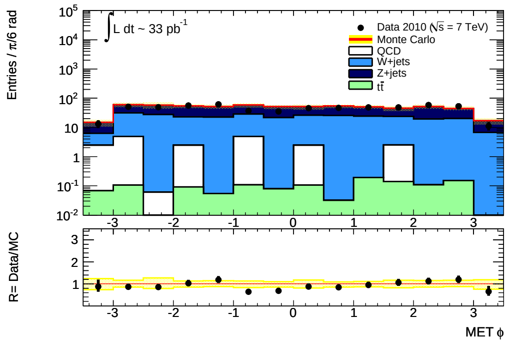

(c)

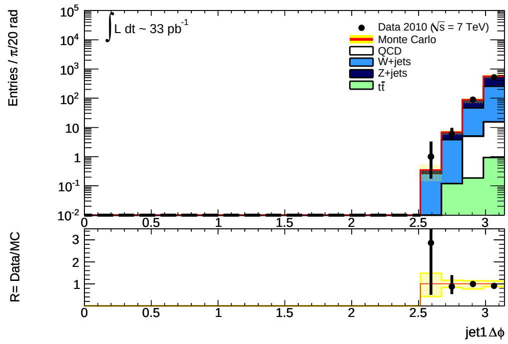

(d)

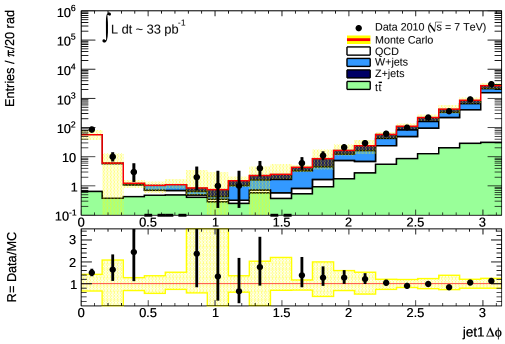

(e)

Figure D.1: η and ϕ of the leading jet (D.1(a) and D.1(b)), azimuthal angle of $E_{\mathrm{T}}^{\mathrm{miss}}$ (D.1(c)) and $\Delta\phi$ between the leading jet and $E_{\mathrm{T}}^{\mathrm{miss}}$ (D.1(d)) after all `LowPt` selection cuts are applied (L3). Furthermore $\Delta\phi$ between the leading jet and $E_{\mathrm{T}}^{\mathrm{miss}}$ (D.1(e)) after only the cut on $E_{\mathrm{T}}^{\mathrm{miss}}$ (L1).

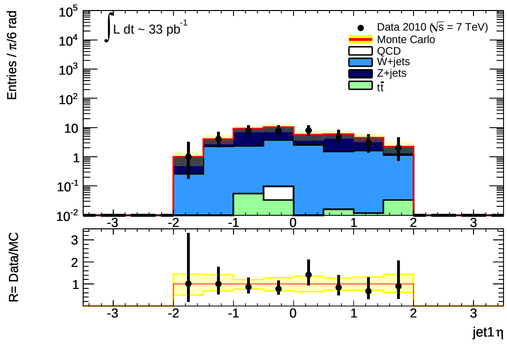

(a)

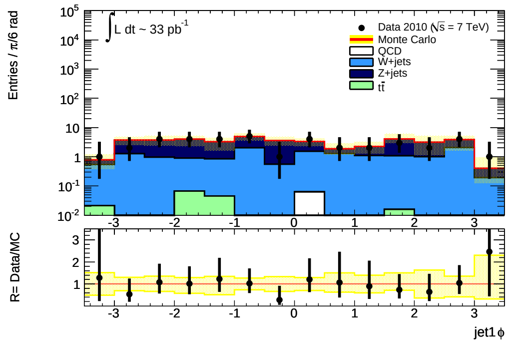

(b)

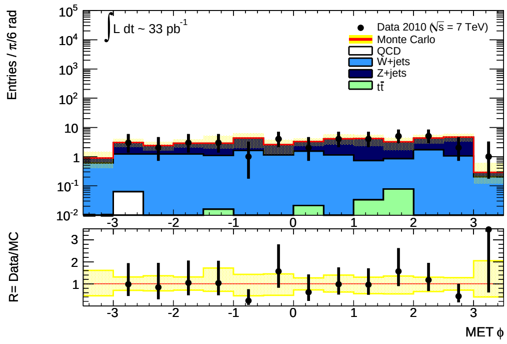

(c)

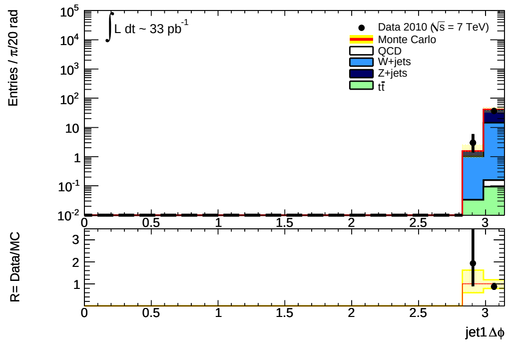

(d)

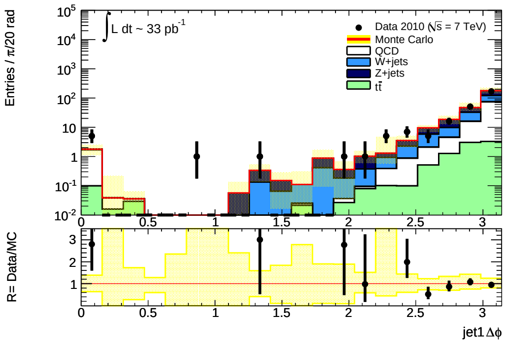

(e)

Figure D.2: η and ϕ of the leading jet (D.2(a) and D.2(b)), azimuthal angle of $E_{\mathrm{T}}^{\mathrm{miss}}$ (D.2(c)) and $\Delta\phi$ between the leading jet and $E_{\mathrm{T}}^{\mathrm{miss}}$ (D.2(d)) after all `HighPt` selection cuts are applied (H4). Furthermore $\Delta\phi$ between the leading jet and $E_{\mathrm{T}}^{\mathrm{miss}}$ (D.2(e)) after only the cut on $E_{\mathrm{T}}^{\mathrm{miss}}$ (H1).

Bibliography

[1] D. Griffiths, *Introduction to elementary particles*, . Weinheim, Germany: Wiley-VCH (2008) 454 p.

[2] K. Nakamura and others (Particle Data Group), *The Review of Particle Physics*, J. Phys. G 37, 075021 (2010) .

[3] S. Nussinov and R. Shrock, *Upper Limits on a Possible Gluon Mass*, Phys. Rev. **D82** (2010) 034031, `arXiv:1005.0850 [hep-ph]`.

[4] S. L. Glashow, *Partial Symmetries of Weak Interactions*, Nucl. Phys. **22** (1961) 579–588.

[5] S. Weinberg, *A Model of Leptons*, Phys. Rev. Lett. **19** (1967) 1264–1266.

[6] V. N. Gribov and B. Pontecorvo, *Neutrino astronomy and lepton charge*, Phys. Lett. **B28** (1969) 493.

[7] A. D. Sakharov, *Violation of CP Invariance, c Asymmetry, and Baryon Asymmetry of the Universe*, Pisma Zh. Eksp. Teor. Fiz. **5** (1967) 32–35.

[8] G. Bertone, D. Hooper, and J. Silk, *Particle dark matter: Evidence, candidates and constraints*, Phys. Rept. **405** (2005) 279–390, `arXiv:hep-ph/0404175`.

[9] G. Bertone, *The moment of truth for WIMP Dark Matter*, Nature **468** (2010) 389–393, `arXiv:1011.3532 [astro-ph.CO]`.

[10] P. J. E. Peebles and B. Ratra, *The cosmological constant and dark energy*, Rev. Mod. Phys. **75** (2003) 559–606, `arXiv:astro-ph/0207347`.

[11] S. P. Martin, *A Supersymmetry Primer*, Tech. Rep. hep-ph/9709356, Sep, 1997.

[12] H. Baer and X. Tata, *Weak scale supersymmetry: From superfields to scattering events*, . Cambridge, UK: Univ. Pr. (2006) 537 p.

[13] S. Weinberg, *The quantum theory of fields. Vol. 3: Supersymmetry*, . Cambridge, UK: Univ. Pr. (2000) 419 p.

[14] J. D. Wells, *Implications of supersymmetry breaking with a little hierarchy between gauginos and scalars*, `arXiv:hep-ph/0306127`.

[15] N. Arkani-Hamed and S. Dimopoulos, *Supersymmetric unification without low energy supersymmetry and signatures for fine-tuning at the LHC*, JHEP **06** (2005) 073, arXiv:hep-th/0405159.

[16] G. F. Giudice and A. Romanino, *Split supersymmetry*, Nucl. Phys. **B699** (2004) 65–89, arXiv:hep-ph/0406088.

[17] W. Kilian, T. Plehn, P. Richardson, and E. Schmidt, *Split supersymmetry at colliders*, Eur. Phys. J. **C39** (2005) 229–243, arXiv:hep-ph/0408088.

[18] A. C. Kraan, *Interactions of R-hadrons in ATLAS*, arXiv:hep-ex/0506009.

[19] J. L. Hewett, B. Lillie, M. Masip, and T. G. Rizzo, *Signatures of long-lived gluinos in split supersymmetry*, JHEP **09** (2004) 070, arXiv:hep-ph/0408248.

[20] CMS Collaboration, *Search for Heavy Stable Charged Particles in pp collisions at sqrt(s)=7 TeV*, JHEP **03** (2011) 024, arXiv:1101.1645 [hep-ex].

[21] M. A. Dobbs et al., *Les Houches guidebook to Monte Carlo generators for hadron collider physics*, arXiv:hep-ph/0403045.

[22] T. Sjostrand, S. Mrenna, and P. Skands, *"PYTHIA 6.4 Physics and Manual"*, 2006. JHEP **05** (2006) 026, arXiv:hep-ph/0603175.

[23] G. Corcella et al., *Herwig 6: An event generator for hadron emission reactions with interfering gluons (including supersymmetric processes)*, JHEP **01** (2001) 010, arXiv:hep-ph/0011363.

[24] G. Corcella et al., *Herwig 6.5 release note*, arXiv:hep-ph/0210213.

[25] J. Butterworth, J. Forshaw, and M. Seymour, *Multiparton interactions in photoproduction at HERA*, Z. Phys. **C72** (1996) 637–646, hep-ph/9601371.

[26] F. Paige, S. Protopopescu, H. Baer, and X. Tata, *ISAJET 7.69: A Monte Carlo event generator for p p, anti-p p, and e+ e- reactions*, arXiv:hep-ph/0312045.

[27] M. Mangano et al., *Alpgen, a generator for hard multiparton processes in hadronic collisions*, JHEP **07** (2003) 001, arXiv:hep-ph/0206293.

[28] S. Frixione and B. Webber, *The MC@NLO 3.2 event generator*, arXiv:hep-ph/0601192.

[29] W. Beenakker, R. Hopker, and M. Spira, *PROSPINO: A program for the PROduction of Supersymmetric Particles In Next-to-leading Order QCD*, arXiv:hep-ph/9611232.

[30] R. Gavin, Y. Li, F. Petriello, and S. Quackenbush, *FEWZ 2.0: A code for hadronic Z production at next-to- next-to-leading order*, arXiv:1011.3540 [hep-ph].

[31] ATLAS Collaboration, *ATLAS: technical proposal for a general-purpose pp experiment at the Large Hadron Collider at CERN*. LHC Tech. Proposal. CERN, Geneva, 1994.

[32] ATLAS Collaboration, *The ATLAS Experiment at the CERN Large Hadron Collider*, J. Instrum. **3** (2008) S08003. 437 p.

[33] G. Kane and A. Pierce, *Perspectives on LHC Physics*. World Scientific, Singapore, 2008.

[34] J.-L. Caron, *Overall view of LHC experiments.. Vue d'ensemble des experiences du LHC.*, AC Collection. Legacy of AC. Pictures from 1992 to 2002., May, 1998.

[35] CMS Collaboration.

[36] C. Kuhn, *The ALICE experiment at LHC*, Nucl. Phys. A **787** (2007) 19c–28c.

[37] LHC-B Collaboration, *LHC-B: A dedicated LHC collider beauty experiment for precision measurements of CP-violation. Letter of intent*, . CERN-LHCC-95-05.

[38] W. K. H. Panofsky, *Evolution of particle accelerators and colliders*, SLAC Beam Line **27N1** (1999) 36–44.

[39] J. Pequenao, *Computer generated image of the whole ATLAS detector*, Mar, 2008.

[40] J. Pequenao, *Computer generated image of the ATLAS inner detector*, Mar, 2008.

[41] J. Pequenao, *Computer Generated image of the ATLAS calorimeter*, Mar, 2008.

[42] ATLAS, *Readiness of the ATLAS Tile Calorimeter for LHC collisions. oai:cds.cern.ch:1282535*, Eur. Phys. J. C **70** (Jul, 2010) 1193–1236. 64 p. Comments: Submitted for publication in EPJC.

[43] GEANT4 Collaboration, S. Agostinelli et al., *GEANT4: A simulation toolkit*, Nucl. Instrum. Meth. **A506** (2003) 250–303.

[44] R. Brun and F. Rademakers, *ROOT: An object oriented data analysis framework*, Nucl. Instrum. Meth. **A389** (1997) 81–86.

[45] F. Ahles, S. Caron, and J. E. Sundermann, *Investigating* E_T^{miss} *in early data with a monojet analysis*, Tech. Rep. ATL-PHYS-INT-2009-111, CERN, Geneva, Dec, 2009.

[46] K. Cranmer, *The ATLAS Analysis Architecture. oai:cds.cern.ch:1047631*, .

[47] K. Koeneke, *Distributing and storing required data efficiently by means of specifically tailored data formats in the ATLAS collaboration*, Tech. Rep. ATL-SOFT-PROC-2011-036, CERN, Geneva, Jan, 2011.

[48] K. Cranmer, A. Farbin, and A. Shibata, *EventView - The Design Behind an Analysis Framework*, Tech. Rep. ATL-SOFT-PUB-2007-008. ATL-COM-SOFT-2007-012, CERN, Geneva, Sep, 2007.

[49] ATLAS Collaboration, G. Aad et al., *Expected Performance of the ATLAS Experiment - Detector, Trigger and Physics*, `arXiv:0901.0512 [hep-ex]`.

[50] ATLAS Collaboration, *Electron and photon reconstruction and identification in ATLAS: expected performance at high energy and results at 900 GeV*, Tech. Rep. ATLAS-CONF-2010-005, CERN, Geneva, Jun, 2010.

[51] B. Resende, *Muon identification algorithms in ATLAS*, Tech. Rep. ATL-PHYS-PROC-2009-113, CERN, Geneva, Sep, 2009.

[52] F. Ahles and B. Meirose, *Studying suppression of beam-induced and cosmic background to physics analyses*, Tech. Rep. ATL-PHYS-INT-2010-031, CERN, Geneva, Apr, 2010.

[53] *AthenaRootAccess: https://twiki.cern.ch/twiki/bin/view/AtlasProtected/AthenaROOTAccess*, .

[54] J. D. Chapman, *The ATLAS Detector Digitization Project for 2009 data taking*, .

[55] M. Gyulassy and X.-N. Wang, *"HIJING 1.0: A Monte Carlo program for parton and particle production in high-energy hadronic and nuclear collisions"*, Comput. Phys. Commun. **83** (1994) 307, `arXiv:nucl-th/9502021`.

[56] A. R. Stradling, W. S. Lan, and B. Mellado, *"An Examination of Backgrounds to Early-Run Minimum-Bias Events in ATLAS at the LHC. oai:cds.cern.ch:1192843"*. PhD thesis, Madison, WI, University of Wisconsin - Madison, Madison, WI, 2008. Presented on 27 Mar 2008.

[57] A. Rossi, *Residual Gas Density Estimations in the LHC Insertion Regions IR1 and IR5 and the Experimental Regions of ATLAS and CMS for Different Beam Operations*, Tech. Rep. LHC-Project-Report-783. CERN-LHC-Project-Report-783, CERN, Geneva, Sep, 2004.

[58] N. P. Konstantinidis et al., *"The Atlantis event visualisation program for the ATLAS experiment"*, 2005.

[59] R. Teuscher, *Private communication*, 2009.

[60] A. Ferrari, P. R. Sala, A. Fasso, and J. Ranft, *"FLUKA: A multi-particle transport code (Program version 2005)"*, . CERN-2005-010.

[61] L. de Andrade Filho and J. de Seixas, *"A ROOT Tools for 3D Event Visualization in ATLAS Calorimeter", Proceedings of Science, XI International Workshop on Advanced Computing Analysis Techniques in Physics Research*, 2007.

[62] L. de Andrade Filho and J. de Seixas, *"Combining Hough Transform and Optimal Filtering for Efficient Cosmic Ray Detection with a Hadronic Calorimeter", Proceedings of Science, XII Advanced Computing and Analysis Techniques in Physics Research*, 2008.

[63] H. Okawa, R. Teuscher, A. Gibson, B. Guo, G. Rosenbaum, A. Yurkewicz, B. Meirose, A. Nepomuceno, T. Bain, L. Filho, N. Ilic, and C. Flores, *Calorimeter Commissioning With Cosmic Rays: Cells, Clusters, Jets and Missing ET*, Tech. Rep. ATL-COM-CAL-2008-007, CERN, Geneva, Dec, 2008.

[64] A. Hocker et al., *TMVA: Toolkit for multivariate data analysis*, PoS **ACAT** (2007) 040, arXiv:physics/0703039.

[65] R. Teuscher et al., *"Fake Missing Transverse Energy from ATLAS Calorimeter Cosmic Ray Data"*, Tech. Rep. ATL-CAL-INT-2008-001. ATL-COM-CAL-2008-002, CERN, Geneva, Feb, 2008.

[66] M. Boonekamp et al., *"Cosmic Ray, Beam-Halo and Beam-Gas Rate Studies for ATLAS Commissioning"*, Tech. Rep. ATL-GEN-2004-001, CERN, Geneva, Feb, 2004.

[67] W. Bell, *Minimum Bias Walk-through:Trigger: http://indico.cern.ch/getFile.py/access?contribId=5&resId=1&materialId=slides&confId=67249*, .

[68] ATLAS Collaboration, *Search for squarks and gluinos using final states with jets and missing transverse momentum with the ATLAS detector in sqrt(s) = 7 TeV proton-proton collisions*, Tech. Rep. ATL-PHYS-INT-2011-009, CERN, Geneva, Feb, 2011.

[69] ATLAS Collaboration, *Search for squarks and gluinos using final states with jets and missing transverse momentum with the ATLAS detector in sqrt(s) = 7 TeV proton-proton collisions*, arXiv:1102.5290 [hep-ex]. * Temporary entry *.

[70] R. Bruneliere, M. Baak, J. Lundberg, M. C. Rammensee, and T. J. Khoo, *Setting exclusion limits in ATLAS supersymmetry searches with a likelihood ratio based method*, Tech. Rep. ATL-COM-PHYS-2011-004, CERN, Geneva, Jan, 2011. This is our support note with limit setting procedures for (for example) the 0,1,2 lepton SUSY notes/papers.

[71] ATLAS Collaboration, *ATLAS Monte Carlo tunes for MC09*, ATL-PHYS-PUB-2010-002, 2010.

[72] D. Stump et al., *Inclusive jet production, parton distributions, and the search for new physics*, JHEP **10** (2003) 046, arXiv:hep-ph/0303013.

[73] K. Melnikov and F. Petriello, *Electroweak gauge boson production at hadron colliders through O(alpha(s)**2)*, Phys. Rev. **D74** (2006) 114017, arXiv:hep-ph/0609070.

[74] S. Frixione and B. Webber, *Matching NLO QCD computations and parton shower simulations*, JHEP **06** (2002) 029, arXiv:hep-ph/0204244.

[75] S. Moch and P. Uwer, *Heavy-quark pair production at two loops in QCD*, Nucl. Phys. Proc. Suppl. **183** (2008) 75–80, arXiv:0807.2794 [hep-ph].

[76] A. Sherstnev and R. Thorne, *Parton Distributions for LO Generators*, Eur. Phys. J. **C55** (2008) 553–575, arXiv:0711.2473 [hep-ph].

[77] R. Barbieri, S. Ferrara, and C. Savoy, *Gauge models with spontaneously broken local supersymmetry*, Physics Letters B **119** (1982) no. 4-6, 343 – 347.

[78] L. Hall, J. Lykken, and S. Weinberg, *Supergravity as the messenger of supersymmetry breaking*, Phys. Rev. D **27** (1983) no. 10, 2359–2378.

[79] CDF Collaboration, T. Aaltonen et al., *Inclusive Search for Squark and Gluino Production in $p\bar{p}$ Collisions at $\sqrt{s}$ = 1.96-TeV*, Phys. Rev. Lett. **102** (2009) 121801, arXiv:0811.2512 [hep-ex].

[80] D0 Collaboration, V. M. Abazov et al., *Search for squarks and gluinos in events with jets and missing transverse energy using 2.1 fb^{-1} of $p\bar{p}$ collision data at $\sqrt{s}$ = 1.96-TeV*, Phys. Lett. **B660** (2008) 449–457, arXiv:0712.3805 [hep-ex].

[81] M. Bahr et al., *Herwig++ Physics and Manual*, Eur. Phys. J. **C58** (2008) 639–707, arXiv:0803.0883 [hep-ph].

[82] M. Bahr et al., *Herwig++ 2.3 release note, arXiv:0812.0529*, 0812.0529, 2008.

[83] W. Beenakker, R. Hopker, M. Spira, P.M. Zerwas, Squark and gluino production at hadron colliders, Nucl. Phys. B492 (1997), 51.

[84] M. Cacciari, G. P. Salam, and G. Soyez, *The anti-k_t jet clustering algorithm*, JHEP **04** (2008) 063, arXiv:0802.1189 [hep-ph].

[85] W. Lampl et al., *Calorimeter Clustering Algorithms: Description and Performance*, Tech. Rep. ATL-LARG-PUB-2008-002, CERN, 2008.

[86] ATLAS Collaboration, *Measurement of the W→lnu and Z/gamma*→ll production cross sections in proton-proton collisions at $\sqrt{s}$ = 7 TeV with the ATLAS detector*, arXiv:1010.2130 [hep-ex].

[87] *https://twiki.cern.ch/twiki/bin/view/AtlasProtected/HowToCleanJets*, .

[88] A. J. Barr and C. Gwenlan, *The race for supersymmetry: using m_{T2} for discovery*, Phys. Rev. **D80** (2009) 074007, arXiv:0907.2713 [hep-ph].

[89] H.-C. Cheng and Z. Han, *Minimal Kinematic Constraints and m_{T2}*, JHEP **12** (2008) 063, arXiv:0810.5178 [hep-ph].

[90] ATLAS Collaboration, *Jet energy scale and its systematic uncertainty for jets produced in proton-proton collisions at sqrt(s) = 7 TeV and measured with the ATLAS detector*, Tech. Rep. ATLAS-CONF-2010-056, CERN, Geneva, Jul, 2010.

[91] ATLAS Collaboration, *Jet energy resolution and selection efficiency relative to track jets from in-situ techniques with the ATLAS Detector Using Proton-Proton Collisions at a Center of Mass Energy sqrts = 7 TeV*, Tech. Rep. ATLAS-CONF-2010-054, CERN, Geneva, Jul, 2010.

[92] S. Frixione, P. Nason, and G. Ridolfi, *A Positive-Weight Next-to-Leading-Order Monte Carlo for Heavy Flavour Hadroproduction*, JHEP **09** (2007) 126, arXiv:0707.3088 [hep-ph].

[93] E. Gross and O. Vitells, *Trial factors for the look elsewhere effect in high energy physics*, .

[94] J. Abdallah, F. Ahles, H. Beauchemin, P. Calfayan, S. Caron, S. Horner, N. Kanaya, S. Kazama, I. Korolkov, M. Martinez, S. Poddar, T. Rave, R. Rezvani, V. Rossetti, R. Rurikova, N. Ryder, P. Savard, J. Sundermann, and K. Terashi, *Search for mono-jet plus missing transverse energy in pp collisions at* $\sqrt(s) = 7\,TeV$ *with the ATLAS detector*, Tech. Rep. ATL-COM-PHYS-2011-040, CERN, Geneva, Jan, 2011.

[95] T. Cornelisen, C. Gay, C. Gemme, S. Hellman, E. Klinkby, C. Marino, R. Mackeprang, P. Mermod, W. Mills, D. Milstead, C. Ohm, H. Ogren, T. Petersen, M. Joergensen, L. Rossi, and D. Zieminska, *Search for Stable Hadronising Squarks and Gluinos at the ATLAS Experiment at the LHC*, Tech. Rep. ATL-COM-PHYS-2010-1065, CERN, Geneva, Dec, 2010.

[96] B. Andersson, G. Gustafson, G. Ingelman, and T. Sjostrand, *Parton Fragmentation and String Dynamics*, Phys. Rept. **97** (1983) 31–145.

[97] M. Fairbairn et al., *Stable massive particles at colliders*, Phys. Rept. **438** (2007) 1–63, `arXiv:hep-ph/0611040`.

[98] R. Mackeprang and D. Milstead, *An Updated Description of Heavy-Hadron Interactions*, Eur. Phys. J. **C66** (2010) 493–501, `arXiv:0908.1868 [hep-ph]`.

[99] G. F. Farrar, R. Mackeprang, D. Milstead, and J. P. Roberts, *Limit on the mass of a long-lived or stable gluino*, `arXiv:1011.2964 [hep-ph]`.

[100] R. Mackeprang and A. Rizzi, *Interactions of coloured heavy stable particles in matter*, Eur. Phys. J. **C50** (2007) 353–362, `arXiv:hep-ph/0612161`.

[101] A. C. Kraan, *Interactions of heavy stable hadronizing particles*, Eur. Phys. J. **C37** (2004) 91–104, `arXiv:hep-ex/0404001`.

[102] Y. R. de Boer, A. B. Kaidalov, D. A. Milstead, and O. I. Piskounova, *Interactions of Heavy Hadrons using Regge Phenomenology and the Quark Gluon String Model*, J. Phys. **G35** (2008) 075009, `arXiv:0710.3930 [hep-ph]`.

[103] P. M. Nadolsky et al., *Implications of CTEQ global analysis for collider observables*, Phys. Rev. **D78** (2008) 013004, `arXiv:0802.0007 [hep-ph]`.

[104] A. D. Martin, W. J. Stirling, R. S. Thorne, and G. Watt, *Parton distributions for the LHC*, Eur. Phys. J. **C63** (2009) 189–285, `arXiv:0901.0002 [hep-ph]`.

[105] J. Alwall et al., *MadGraph/MadEvent v4: The New Web Generation*, JHEP **09** (2007) 028, `arXiv:0706.2334 [hep-ph]`.

[106] T. Junk, *Confidence Level Computation for Combining Searches with Small Statistics*, Nucl. Instrum. Meth. **A434** (1999) 435–443, `arXiv:hep-ex/9902006`.

[107] ATLAS Collaboration Collaboration, G. Aad et al., *Search for stable hadronising squarks and gluinos with the ATLAS experiment at the LHC*, arXiv:1103.1984 [hep-ex]. * Temporary entry *.

[108] L. Asquith, B. Brelier, J. M. Butterworth, M. Campanelli, T. Carli, G. Choudalakis, P. A. Delsart, S. De Cecco, P. O. Deviveiros, M. D'Onofrio, S. Eckweiler, E. Feng, P. Francavilla, S. Grinstein, I. La Plante, J. Huston, N. Ghodbane, D. Lopez Mateos, B. Martin, N. Makovec, S. Majewsky, M. Martinez, D. W. Miller, J. Monk, K. Perez, C. Roda, J. Robinson, A. Schwartzmann, F. Spano, K. Terashi, F. Vives, P. Weber, and S. Zenz, *Performance of Jet Algorithms in the ATLAS Detector*, Tech. Rep. ATL-PHYS-INT-2010-129, CERN, Geneva, Dec, 2010.

[109] *https://savannah.cern.ch/bugs/?30662)*, .

List of Figures

List of Tables